nature portfolio

Peer Review File

Electronic-resonance Enhanced Molecule for Perovskite Solar Cells

Corresponding Author: Professor Yaowen Li

Any redactions in this file are there to maintain patient confidentiality, the confidentiality of unpublished data, or to remove third-party material.

Parts of this Peer Review File have been redacted as indicated to remove third-party material.

Attachments originally included by the reviewers as part of their assessment can be found at the end of this file.

Version 0:

Reviewer comments:

Referee #1

(Remarks to the Author)
In this work, Wu et al. develop a novel SAM molecule for inverted perovskite solar cells, achieving impressive device performance and significantly enhanced stability under various conditions. However, many of the characterizations of the SAM molecules, as well as some of the conclusions drawn, are incorrect, which undermines the overall reliability of the manuscript. Therefore, I do not recommend this article for publication in Nature at the current stage.

1. The chemical structures of FTPA–CPA and FMTPA–CAPA presented in this manuscript are incorrect. The configuration of the C=C double bond should be E rather than Z. In other words, the CN group should be located on the same side as the other C=C double bond to minimize steric effects. Consequently, the following characterizations and simulations of these two molecules are not convincing. In addition, there are several errors in the structural drawings in both the manuscript and the Supporting Information.

2. Based on my understanding, the intensity of ESR signals cannot be used to indicate the capacity of intramolecular electron transfer within materials. Therefore, the authors should employ additional or alternative measurements to support this assumption. In addition, the conjugated structures of FTPA–CPA and FMTPA–CAPA shown in Fig. 1a do not represent stable resonance structures.

3. The molecular dipole moment reflects the distribution of positive and negative electrical charges within a molecule, which is not directly related to the molecule's intramolecular electron-transfer capacity.

4. Phosphonic acid is a strong acid; therefore, the pKa of this type of material is expected to be below 2. The reviewer suggests that the authors remeasure to confirm pKa values.

5. The surface energy alignment and charge extraction of the SAM-deposited substrate are determined by the molecular dipole moments of the SAM molecules, rather than by their electron resonance properties.

6. Regarding device performance, the authors only provide the PCE of the champion devices; other performance parameters and device PCEs under different conditions should also be included in the manuscript for comparison. In addition, for the stability measurements, the authors should report the initial performance of the devices.

Referee #2

(Remarks to the Author)
Reviewer comments

Authors report a significant advancement on both power conversion efficiency and operation stability through designing a novel self-assembly molecule with resonant structure. Thus, the originality of this study is a novel SAM molecule, FMTPA-CPA, in which the resonant charge delocalization facilitates efficient carrier transport and the electronic resonance strengthens the phosphonic acid-ITO anchoring bond to prevent the SAM molecule desorption during operation. As a result, the inverted perovskite solar cells with this SAM molecule shows a certified efficiency of 27.45% with excellent stability even under various conditions. Research on SAMs is highly active, focusing on reinforcing SAMs or solving interfacial issues with perovskites. Unlike previous studies, this manuscript focuses on the desorption from ITO, which is undoubtedly a novel and significant issue. Very recently, a study addressing an issue similar to this manuscript was published in Science (10.1126/science.adz7969). This paper not only reports long-term stability in a harsher environment (light including UV + thermal stress) than this manuscript, but also presents long-term stability in large-area modules. Although this manuscript reports a record-high efficiency exceeding 27%, the long-term stability results remain largely similar to those of previously reported studies (e.g., 10.1038/s41586-025-09509-7). Consequently, the actual effect of the proposed resonance-enhanced structure in improving long-term durability remains unclear. While the recent Science report identifying UV light as a critical degradation factor, this manuscript lacks experimental validation under UV-inclusive environments. Thus, the current version does not sufficiently demonstrate the extraordinary conceptual advancement required for Nature. Thus, for publication in Nature, authors should substantially revise the manuscript to provide stronger evidence and new scientific insights that clearly distinguish this study from the recent science paper.

1. Recent studies have already reported perovskite solar cells with exceptional stability under combined LED and thermal stress (10.1038/s41586-025-09509-7). However, a very recently published Science paper (10.1126/science.adz7969) reports UV light as the primary cause of bond dissociation between ITO and SAMs. This is a critical consideration as actual operating environments inevitably include UV exposure. Nevertheless, this manuscript lacks experimental results addressing this issue. Therefore, experimental verification is required to demonstrate whether the developed SAM maintains a stable bond with ITO under UV light or a combined environment of light including UV and heat.

2. While this manuscript addresses SAM desorption through a resonance-enhanced structure, it lacks a critical qualitative distinction between covalent and hydrogen bonding. As established in recent Science paper, ensuring robust covalent anchoring is essential to prevent UV-induced bond decomposition and subsequent chemical degradation of the perovskite. The current evidence, based on ethanol washing, is insufficient to demonstrate the formation of these critical covalent bonds as opposed to mere hydrogen bonding. Therefore, additional verification, such as acid-washing tests, is required to demonstrate that the resonance effect fundamentally promotes stable covalent anchoring.

3. In the top-view SEM images, a significant amount of PbI2 is observed on the perovskite surface. While the presence of PbI2 can positively contribute to efficiency enhancement, it can be detrimental to long-term photostability. Specifically, PbI2 is highly susceptible to decomposition under light below 500 nm, raising concerns about its impact on the device's long-term reliability. The authors should provide SEM images before and after long-term stability to demonstrate the effect of PbI2 on long-term stability.

4. It is essential to provide long-term stability data under a combined environment of UV-inclusive light and thermal stress. Providing this result should be presented as a key result to demonstrate practical durability.

5. The current manuscript lacks logical justification for this strategy. Therefore, the introduction should be substantially revised to emphasize the significance of the proposed strategy and clearly differentiate it from a recent paper.

6. The C-AFM images (Fig. 3c) are currently missing scale bars. Authors should add the scale bars.

7. To ensure the reproducibility of the reported 27.45% efficiency and long-term stability data, the exact number of independent cells used for each statistical analysis must be clearly stated.

Referee #3

(Remarks to the Author)
This manuscript presents an impressive advance in the field of perovskite solar cells by introducing an electronic-resonance enhanced self-assembled monolayer (SAM) of FMTPA-CPA. The core concept of using a symmetric D-A-D-like resonant molecular structure to intrinsically enhance the negative charge density at the phosphonic acid anchoring site is innovative and significant. The reported results are outstanding, with a certified PCE of 27.45% for rigid small-area devices, 26.64% for flexible devices, and 23.63% for a mini-module. The operational stability results under various conditions (99% PCE retention after 1080 h MPPT at 85°C, 97% after 1000 h day/night cycling, 98% after 720 thermal cycles) are state-of-the-art and address a critical bottleneck for commercialization. The work is undoubtedly suitable for a high-impact journal. However, to establish the proposed mechanisms and validate the extraordinary claims, substantial revisions and clarifications are required. Several key aspects of the experimental evidence, data interpretation, and mechanistic depth are currently insufficient or give rise to questions. The manuscript should be reconsidered after revisions addressing the following points.
1. The authors attribute the stability to robust monolayer anchoring. However, the evidence for a complete, uniform monolayer of different molecules on ITO, both initially and after aging, is indirect. It is possible that the initial coverage

includes multilayers or aggregates, and the observed stability during aging might simply reflect the desorption of only weakly bound excess molecules, not the anchored monolayer itself. The authors should provide more direct and conclusive evidence.
2. The manuscript compellingly argues that resonance enhances charge density at the anchor. However, a critical question remains: how much stronger is the anchoring due to resonance compared to other established strategies for improving SAM anchoring stability? Recent works (Science 2024, 383, 1236; Adv. Mater. 2025, adma.202514735; Nature 2025, 646, 95) have also achieved improved stability. The authors should calculate and compare the intrinsic P-O-In binding energies and, if possible, experimentally measure the desorption activation energies for their resonant SAM versus representative molecules from these other strategic classes. This is essential to contextualize the novelty and superiority of the resonance approach within the rapidly evolving field of stable SAMs.
3. The manuscript discusses preventing desorption but does not explicitly address what causes the covalent P-O-In bond to break in the first place during device operation. Is it primarily thermally activated hydrolysis? Electrochemical reactions driven by bias and moisture? Photochemical degradation? Or mechanical stress from perovskite lattice expansion? A deeper investigation into the failure mechanism of the reference SAMs (2PACz, FTPA-CPA) is needed. Clarifying this root cause is vital to explain why the increased negative charge density from resonance offers superior protection.
4. The description of FMTPA-CPA as a "D-A-D" structure is chemically misleading. The two TPA donors are not conjugated to each other through the acceptor. They are independently linked to the central cyanovinyl bridge. Therefore, the electronic structure is better described as two independent D-(π-A) pathways or a symmetric double-D-A system, not a delocalized D-A-D triad.
In addition, comparing FMTPA-CPA (with a CPA anchor) to 2PACz (with a simpler PA anchor) is problematic because the anchoring chemistry itself is different. The observed improvements could be partly attributable to the inherent properties of CPA group (stronger acidity, different coordination geometry) rather than solely the resonance effect. A much fairer and more critical control would be a non-resonant SAM molecule featuring the exact same CPA anchoring group, but without the symmetric donor structure. This control is essential to isolate the effect of the resonant electronic structure.
5. The 1H NMR and 13C NMR of FTPA-CPA seems not so pure. The authors should input details 13C NMR data of FTPA-CPA and FMTPA-CPA in the experimental part, and provide their element analysis data to confirm the purity of final SAM materials.
6. The claim in Fig. 1c and the text that the HOMO orbital distribution "confirms the formation of delocalized diradicals" is unsubstantiated and likely incorrect. The plotted HOMO is a ground-state molecular orbital, not a singly occupied molecular orbital (SOMO) characteristic of a radical. The presence of diradicals or radical character should be investigated through proper theoretical methods. Relying on the HOMO plot for such a claim weakens the theoretical analysis.
7. The in-situ FTIR signals (Fig. 2g-i; Fig. S13) are surprisingly strong for a SAM layer. Were these spectra collected on well-defined monolayers or on as-deposited films that may contain multilayers/physiosorbed material? If they are from monolayers, what experimental setup (grazing incidence, multiple internal reflections) was used to achieve sufficient sensitivity? This detail is crucial, as conventional transmission FTIR is notoriously insensitive to sub-nanometer layers. If they are form multilayers, the observed peak shifts and decrease in intensity for 2PACz and FTPA-CPA could be due to the desorption of weakly bound multilayers rather than changes in the bonded monolayer. Control experiments verifying the monolayer nature of the initial film are necessary to interpret these FTIR trends correctly.
8. For the probing $PO_3H_2^-$ signal in Tof-SIMS data (Fig. S14), once the phosphonic acid anchors to ITO, it loses protons to form P-O-In bonds. The $PO_3H_2^-$ signal, therefore, predominantly originates from non-bound or protonated species such as free molecules, molecules bonded in a monodentate fashion retaining an -OH, or molecules that have hydrolyzed from the surface. Tracking its diffusion into the perovskite may not report on the stability of the covalently anchored monolayer but rather on the mobility of loosely associated acidic species. The authors should justify this choice and complement it with a signal more specific to the anchored state. In addition, the significant noise near the baseline in the $PO_3H_2^-$ profiles for samples in Fig. S14c,d are concerning. The authors should explain the potential source of this noise
9. The use of XPS peak area ratios (P/In) to quantitatively compare SAM coverage across different molecules is highly problematic and a major weakness. XPS is semi-quantitative, and signals from ultrathin layers are prone to large errors, and the P signal intensity is not directly proportional to the number of molecules if their structures differ significantly. To substantiate the coverage and stability claims, the authors must employ more reliable quantitative measurements.
10. Supplementary Fig. 23 appears to show same images for different samples. This must be corrected immediately. In addition, the statement that perovskite on FMTPA-CPA shows higher XRD peak intensity requires quantification. By how much is it higher (please provide integrated intensity ratios)? The proposed reason (improved wettability leading to better crystallization) is plausible but should be supported by additional analysis.
11. The similar PLQY of perovskite on FMTPA-CPA and on bare glass (Fig. 3e) is unusual. Glass/perovskite interfaces are typically highly defective, leading to low PLQY. Therefore, the result requires explanation. Full PLQY spectra and detailed experimental conditions (excitation wavelength, power density, integration sphere calibration procedure) should be provided. The TRPL decays (Fig. 3f) also look unusual, particularly the very long tail for FMTPA-CPA. The test conditions (excitation wavelength, fluence, repetition rate) are mandatory for interpretation. The decays should be measured under identical conditions for all samples. The TRPL of glass/perovskite sample should be provided. The reported SRH lifetimes should be extracted from a proper recombination model with a detailed discussion.
12. The energy level diagram appears inconsistent with the UPS data (Fig. S35), please check again. In addition, UPS shows 2PACz has the largest work function, which should be more favorable for hole extraction in a p-i-n structure, contradicting the narrative that FMTPA-CPA is superior. The HOMO level of FMTPA-CPA does not appear deeper than FTPA-CPA of 2PACz from the UPS secondary electron cut-off and valence band region. The depicted energy level diagram (likely Fig. S35e) needs to be precisely derived from the UPS measurements (work function = 21.22 eV - Ecutoff; HOMO onset relative to Fermi level). A corrected, quantitatively accurate diagram is essential. The authors must reconcile these observations: if FMTPA-CPA has a less favorable work function, what other factor compensates to yield better device performance?
13. The origin of the different temperature dependencies of hole conductivity (Fig. 3g, S36) is not explained. Why does

2PACz show the strongest temperature dependence? Is it due to higher energetic disorder as mentioned? If so, how does the resonant structure of FMTPA-CPA reduce this disorder? The authors should discuss this in the context of molecular packing and electronic coupling. Furthermore, if FTPA-CPA and FMTPA-CPA possess radical character, their charge transport might involve hopping between localized states, which also has a temperature dependence. The authors should elaborate on the proposed transport mechanism in their systems.
14. UV light is known to degrade the interfaces. The UV illumination stability of devices, operational stability under a xenon lamp with UV region are necessary, which will provide critical information on photochemical stability. Additionally, the initial PCE values for all devices subjected to stability tests must be provided to allow readers to assess the starting point.

Version 1:

Reviewer comments:

Referee #1

(Remarks to the Author)
The authors have addressed most of my previous comments. However, I remain confused about the configuration analysis in this work. Specifically, two structurally similar molecules exhibit two different configurations: FTPA-CPA is assigned an E configuration, while FMTPA-CPA is assigned a Z configuration. I strongly recommend that the authors provide additional experimental evidence to support these DFT conclusions, such as single-crystal X-ray diffraction analysis or NMR measurements. Furthermore, the interconversion between E and Z configurations is generally challenging, as it requires a significant input of energy to overcome the π-bond barrier. The authors should consider these experimental approaches and the mechanism rather than relying solely on simulations based on the DFT results.

Referee #2

(Remarks to the Author)
The authors have addressed most of my previous concerns satisfactorily. The revised manuscript represents a substantial improvement over the original submission. However, a few issues still remain that require further attention before I can recommend acceptance of this manuscript.

1.The authors added UV stability data but did not provide a clear mechanistic discussion for why FMTPA-CPA resists UV-induced degradation. The Science paper by Fei et al. proposed that UV selectively cleaves weak hydrogen-bonded PA–TCO interactions through a photochemical pathway distinct from thermal hydrolysis. A more in-depth mechanistic discussion addressing this UV-specific degradation pathway would be needed to substantiate the claim of superior UV stability.

2.The promising small-cell results of FMTPA-CPA raise the question of whether the enhanced stability translates to large-area modules. Given that the Science paper by Fei et al. (10.1126/science.adz7969) has already demonstrated module-level operational stability under combined UV and thermal stress, providing equivalent module-scale data would further strengthen the impact of this work for Nature.

Referee #3

(Remarks to the Author)
The revised manuscript and the point-by-point response contain a significant amount of new experimental data, additional control experiments, and theoretical analyses. The addition of UV-stability tests under combined light/heat stress, the quantitative assembly density measurements, the FOD analysis for radical character, and the critical distinction between covalent and hydrogen bonding via acid washing are all commendable and have substantially improved the manuscript. The updated certified efficiency of 27.69% is also remarkable. The manuscript contains several points that need to be addressed before publishing on Nature.
1. The new control molecule (FMTPA-DCPA) to show that removing the C=C bond and thus disrupting resonance reduces binding energy from -2.31 eV to -1.94 eV. This is a good control. But a quantitative comparison of the resulting anchoring stability under identical stress conditions is suggested to do for convincing new experimental data.
2. The authors have replaced the HOMO-based diradical claim with a proper FOD analysis. The NFOD values (0.10 for 2PACz, 0.43 for FTPA-CPA, 0.66 for FMTPA-CPA) are presented. What is the threshold for the claimed significant radical character? How do these values compare to known stable radicals or diradicals?
3. The UV stability test (Supplementary Fig. 58) indicates that FMTPA-CPA remains 81% after 1080 hours of irradiation. This is lower than the ~99% retention under LED light in the MPPT measurement. The authors should comment on whether this ~20% loss under UV is due to SAM degradation.

Version 2:

Reviewer comments:

Referee #1

(Remarks to the Author)
The authors have adequately addressed my comments. I recommend acceptance of this manuscript.

Referee #2

(Remarks to the Author)
The authors have thoroughly addressed all remaining concerns, substantially strengthening the manuscript. I recommend this work for publication in Nature.

Referee #3

(Remarks to the Author)
The authors have fully addressed all my concerns. The manuscript can be accepted as is.

Response to Reviewers' Comments

We would like to thank all the reviewers for their valuable comments and insightful questions, which have helped us to significantly improve the manuscript. We have now revised the manuscript and added experimental data to address the reviewers' concerns, and a point-by-point response is attached in this document. **These revisions have also been highlighted with red** in the main text and Supplementary Information. We hope that our revised version is now suitable for publication.

Response to Reviewer #1:

In this work, Wu et al. develop a novel SAM molecule for inverted perovskite solar cells, achieving impressive device performance and significantly enhanced stability under various conditions. However, many of the characterizations of the SAM molecules, as well as some of the conclusions drawn, are incorrect, which undermines the overall reliability of the manuscript. Therefore, I do not recommend this article for publication in Nature at the current stage.

Response: Thanks for the reviewer's positive assessment of the device performance and stability enhancement. Regarding the comments that certain characterizations and discussions may not be entirely accurate, we believe this may have arisen from incomplete phrasing in our original manuscript, which could have led to misunderstanding. We have now provided detailed, point-by-point responses to all the raised questions and hope that the revised manuscript addresses the reviewer's concerns.

1. The chemical structures of FTPA–CPA and FMTPA–CAPA presented in this manuscript are incorrect. The configuration of the C=C double bond should be E rather than Z. In other words, the CN group should be located on the same side as the other C=C double bond to minimize steric effects. Consequently, the following characterizations and simulations of these two molecules are not convincing. In addition, there are several errors in the structural drawings in both the manuscript and the Supporting Information.

Response: Thanks for the reviewer's comments. Through systematic Density functional theory (DFT) calculations, we optimize the lowest-energy conformations of both free molecules and anchored molecules on indium tin oxide (ITO) substrates. We find that free molecules and anchored molecules have different stabilized configurations.

For free molecules, FTPA-CPA tends to exhibit E configuration while FMTPA-CPA tends to exhibit Z configuration. Here, we exploited the B3LYP-D3(BJ) to evaluate the intrinsic energies of both E and Z configurations of free molecules. D3(BJ) is a dispersion correction method that incorporates an atom-pairwise dispersion term into the conventional density functional energy, thereby compensating for the insufficient description of London dispersion interactions by traditional density functionals. (*Comput. Chem.*, 2011, 32, 1456) This method allows for a more reliable description of intramolecular and intermolecular noncovalent interactions, and its reliability has been extensively validated in numerous previous studies (*Nature*, 2022,

611, 271; *Nat Commun.*, 2023, 14, 5079). As shown in **Fig. R1** (i.e., **Supplementary Fig. 7** in SI), the energy differences between E and Z configurations of FTPA-CPA and FMTPA-CPA are –0.046 eV and 0.071 eV, respectively, implying that FTPA-CPA tends to exhibit E configuration while FMTPA-CPA tends to exhibit Z configuration. Quantification of the ratio between E and Z configurations can be conducted using the energy differences results according to Boltzmann distribution equation (*Bull. Chem. Soc. Jpn.*, 2017, 90, 1005; *ACS Phys. Chem Au*, 2021, 1, 14).

$$\rho(Z) = \frac{e^{-E_Z/(k_B T)}}{e^{-E_Z/(k_B T)} + e^{-E_E/(k_B T)}}$$

$$\rho(E) = \frac{e^{-E_E/(k_B T)}}{e^{-E_Z/(k_B T)} + e^{-E_E/(k_B T)}}$$

In this equation, $\rho(Z)$ and $\rho(E)$ are the probability of the Z and E configurations with the energies E_Z and E_E, respectively, and k_B is the Boltzmann constant. Consequently, FTPA-CPA exhibits 85% for E configuration and 15% for Z configuration, and FMTPA-CPA exhibits 8% for E configuration and 92% for Z configuration**.**

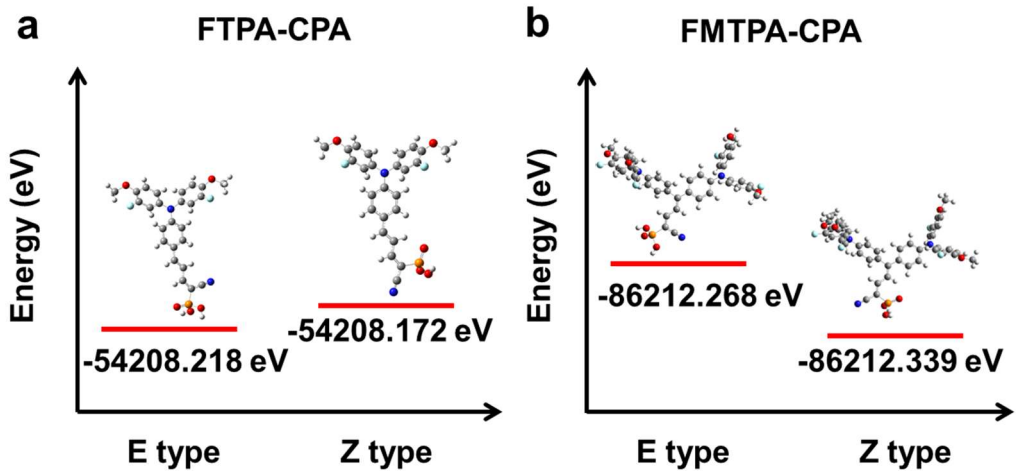

Fig. R1 (i.e., **Supplementary Fig. 7** in SI**)** The intrinsic molecular energies of free (a) FTPA-CPA and (b) FMTPA-CPA molecules.

For molecules anchored on ITO, both FTPA-CPA and FMTPA-CPA exhibit Z configuration. As both FTPA-CPA and FMTPA-CPA are anchored on ITO substrate when applied in pero-SCs, we further compare the total energies of the whole systems composed of both molecules with E (Z) configuration on the ITO substrate (**Fig. R2,** (i.e., **Supplementary Fig. 8** in SI)). The energy differences between E and Z configurations of FTPA-CPA and FMTPA-CPA anchored on ITO are 0.66 eV and 0.51 eV, respectively. With the energy differences exceeding 0.24 eV, the system is almost entirely dominated by the low-energy configuration according to Boltzmann distribution equation (*Bull. Chem. Soc. Jpn.*, 2017, 90, 1005; *ACS Phys. Chem Au*, 2021, 1, 14). Consequently, Boltzmann distribution analysis confirms that both FTPA-CPA and FMTPA-CPA exhibit nearly 100% for Z configuration. These results indicate that, when anchored on ITO substrate, the Z configurations of both molecules are more energetically favored and forms more stable covalent bond anchoring.

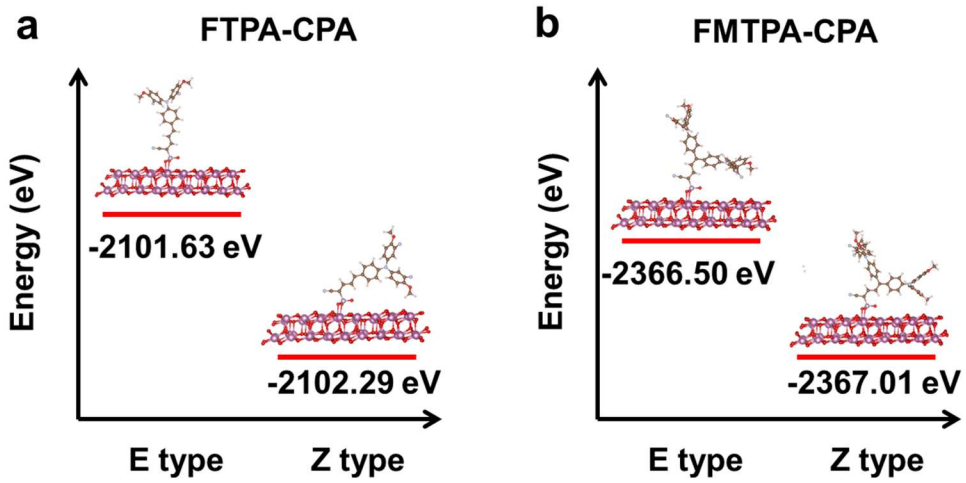

Fig. R2 (i.e., **Supplementary Fig. 8** in SI**)** The total energies of the whole systems composed of (a) FTPA-CPA and (b) FMTPA-CPA with E (Z) configuration on the ITO substrate.

Above all, we revised the chemical drawings of FTPA-CPA free molecular to E configuration and remained the Z configuration for the FMTPA-CPA free molecular (**Fig. R3** (i.e., **Fig. 1a** in main text) & **Supplementary Fig. 1, 2** & **Material Synthesis** in the revised Supplementary Information)). Considering all the DFT simulations aim to elucidate the actual operating condition of both FTPA-CPA and FMTPA-CPA anchored to ITO, where the Z configurations are energetically favored for both molecules, we remained all the DFT simulations results (including electrostatic surface potential (ESP), highest occupied molecular orbital (HOMO), lowest unoccupied molecular orbital (LUMO) and anchoring binding energy) based on Z configuration. We would like to thank the reviewer's insightful comment, which helped us recognize the importance of the molecular configuration and further strengthen quality of our manuscript.

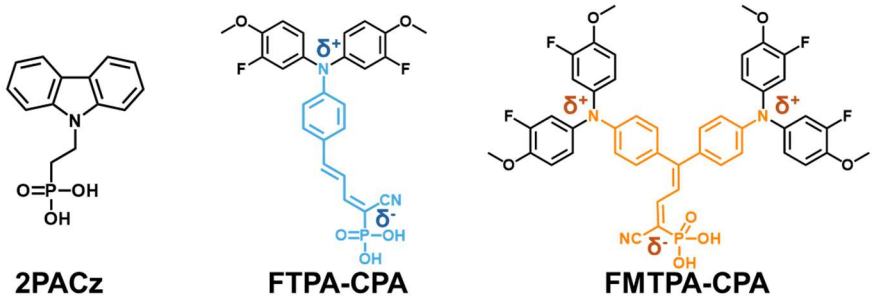

Fig. R3 (i.e., **Fig. 1a** in main text**)** Free molecular structures of 2PACz, FTPA-CPA and FMTPA-CPA (with charge distribution and electronic resonance).

We have revised the chemical structure drawing in the Material Synthesis in the revised Supplementary Information accordingly:
Page 2 in the revised Supplementary Information:

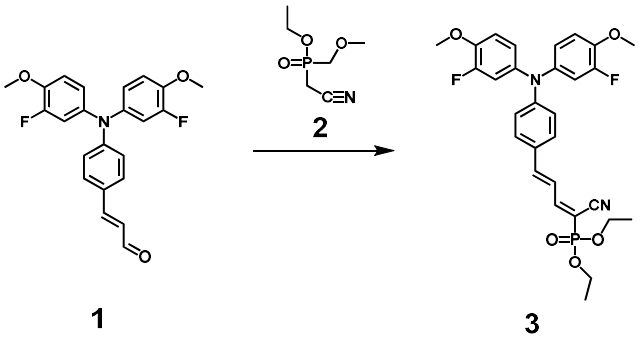

Page 3 in the revised Supplementary Information:

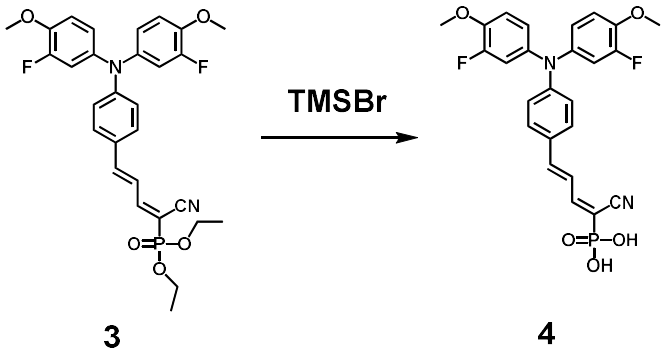

We also added the configuration discussion in the revised Supplementary Information (marked red):

Pages 10~11 in the revised Supplementary Information:

Supplementary Note 1 The discussion of molecular configuration

Through systematic Density functional theory (DFT) calculations, we optimize the lowest-energy conformations of both free molecules and anchored molecules on indium tin oxide (ITO) substrates. We find that free molecules and anchored molecules have different stabilized configurations.

For free molecules, FTPA-CPA tends to exhibit E configuration while FMTPA-CPA tends to exhibit Z configuration. Here, we exploited the B3LYP-D3(BJ) to evaluate the intrinsic energies of both E and Z configurations of free molecules. D3(BJ) is a dispersion correction method that incorporates an atom-pairwise dispersion term into the conventional density functional energy, thereby compensating for the insufficient description of London dispersion interactions by traditional density functionals.[1] This method allows for a more reliable description of intramolecular and intermolecular noncovalent interactions, and its reliability has been extensively validated in numerous previous studies.[2, 3] As shown in **Supplementary Fig. 7**, the energy differences between E and Z configurations of FTPA-CPA and FMTPA-CPA are −0.046 eV and 0.071 eV, respectively, implying that FTPA-CPA tends to exhibit E configuration while FMTPA-CPA tends to exhibit Z configuration. Quantification of the ratio between E and Z configurations can be conducted using the energy differences results according to Boltzmann distribution equation.[4, 5]

$$\rho(Z) = \frac{e^{-E_Z/(k_B T)}}{e^{-E_Z/(k_B T)} + e^{-E_E/(k_B T)}}$$

$$\rho(E) = \frac{e^{-E_E/(k_B T)}}{e^{-E_Z/(k_B T)} + e^{-E_E/(k_B T)}}$$

In this equation, $\rho(Z)$ and $\rho(E)$ are the probability of the Z and E configurations with the energies E_Z and E_E, respectively, and k_B is the Boltzmann constant. Consequently, FTPA-CPA exhibits 85% for E configuration and 15% for Z configuration, and FMTPA-CPA exhibits 8% for E configuration and 92% for Z configuration**.**

For molecules anchored on ITO, both FTPA-CPA and FMTPA-CPA exhibit Z configuration. As both FTPA-CPA and FMTPA-CPA are anchored on ITO substrate when applied in pero-SCs, we further compare the total energies of the whole systems composed of both molecules with E (Z) configuration on the ITO substrate (**Supplementary Fig. 8**). The energy differences between E and Z configurations of FTPA-CPA and FMTPA-CPA anchored on ITO are 0.66 eV and 0.51 eV, respectively. With the energy differences exceeding 0.24 eV, the system is almost entirely dominated by the low-energy configuration according to Boltzmann distribution equation.[4, 5] Consequently, Boltzmann distribution analysis confirms that both FTPA-CPA and FMTPA-CPA exhibit nearly 100% for Z configuration. These results indicate that, when anchored on ITO substrate, the Z configurations of both molecules are more energetically favored and forms more stable covalent bond anchoring. As a result, we conduct DFT simulations on molecular ESP, HOMO and LUMO wavefunctions of both FTPA-CPA and FMTPA-CPA based on Z configuration.

2. Based on my understanding, the intensity of ESR signals cannot be used to indicate the capacity of intramolecular electron transfer within materials. Therefore, the authors should employ additional or alternative measurements to support this assumption. In addition, the conjugated structures of FTPA–CPA and FMTPA–CAPA shown in Fig. 1a do not represent stable resonance structures.

Response: Thanks for the reviewer's comments. In the original manuscript, the claim that "*the red-shifted absorption peak to ~540 nm and strong ESR signal (Fig. 1e) indicate efficient intramolecular electron transfer in FMTPA-CPA*" is indeed somehow misleading. Our intention is to use the electron spin resonance (ESR) signals to show the radical characters of FTPA-CPA and FMTPA-CPA, which results from the charge redistribution between the donor moiety and acceptor moiety in these molecules (*J. Am. Chem. Soc.*, 1997, 119, 10213; *Nat. Commun.*, 2023, 14, 5238). Specifically, the higher ESR signal intensity in FMTPA-CPA shows the stronger radical character, which reflects the more pronounced charge redistribution between donor moiety and acceptor moiety by applying the donor-acceptor-donor (D-A-D) electronic resonance design. Considering that our discussion focuses on the charge density distribution status in SAMs instead of electron transfer process, we will adopt the term "charge redistribution" to replace the "electron transfer" used in the original manuscript.

To provide further quantitative support for the charge redistribution status in different SAMs, we performed DFT calculations and evaluated fragment charges using Atomic dipole corrected Hirshfeld (ADCH) atomic charges in Multiwfn with donor and acceptor fragment partitioning (**Fig. R4** (i.e., **Supplementary Fig. 10** in SI)). Both isolated donor and acceptor fragments are in status of charge neutrality with 0 e. For

2PACz, as the linker group is non-conjugated, the electron-transfer amount between donor and acceptor is only 0.042 e. Interestingly, when replacing the non-conjugated alkyl chain linker to a conjugated linker (**Fig. R4b**), the calculated electron-transfer amount is 0.056 e, suggesting a beneficial charge redistribution through conjugated linker between donor and acceptor moiety. For the FTPA-CPA with a triphenylamine (TPA) donor moiety, a cyanovinyl phosphonic acid (CPA) acceptor moiety, as well as a conjugated linker, the electron-transfer amount increases to 0.115 e (**Fig. R4c**), which implies that an enhancing donor and acceptor moieties can promote the charge redistribution. This assumption can be further demonstrated by FMTPA-CPA, where two TPA donor groups linked with the CPA acceptor group even form electronic resonance, the calculated electron-transfer amount increases to 0.178 e (**Fig. R4d**). It indicates that the design of D-A-D electronic resonance (confirmed by the frontier orbitals calculation results in **Fig. R5** (i.e., **Supplementary Fig. 11** in SI) and molecular crystallography analyze in **Fig R6** (i.e., **Fig. 1f** in main text)) further enhance the charge redistribution and concentrate more negative charge on the acceptor group.

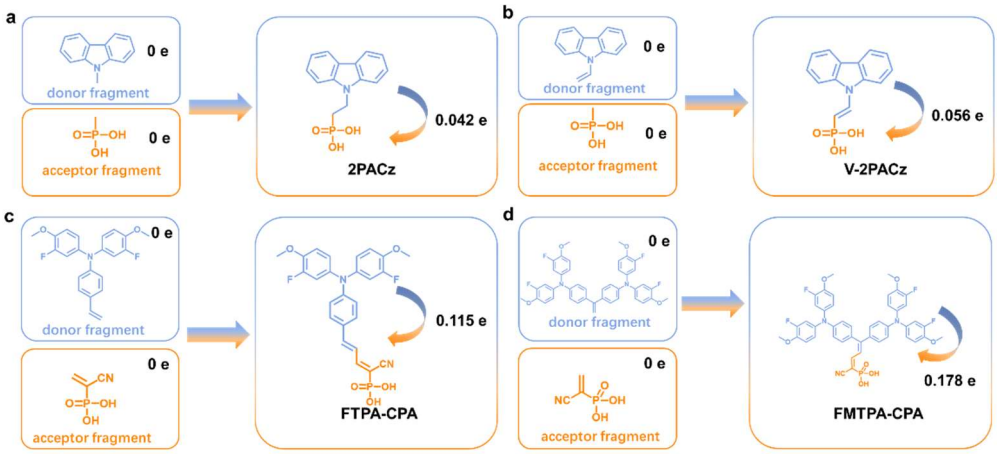

Fig. R4 (i.e., **Supplementary Fig. 10** in SI**)** The donor and acceptor fragmentation charges of (a) 2PACz, (b) V-2PACz, (c) FTPA-CPA and (d) FMTPA-CPA.

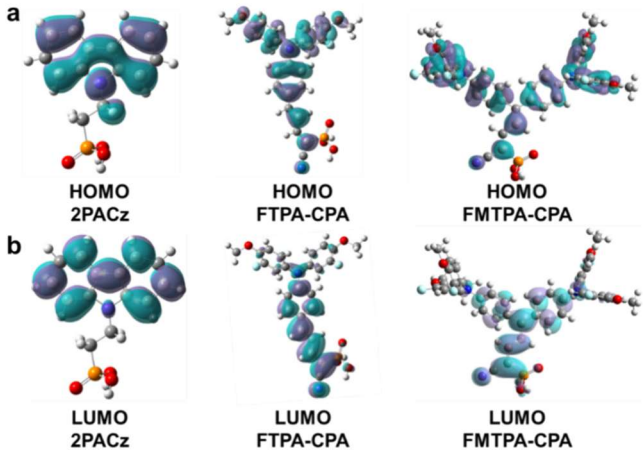

Fig. R5 (i.e., **Supplementary Fig. 11** in SI**)** HOMO and LUMO orbital wavefunctions of 2PACz, FTPA-CPA and FMTPA-CPA at the ground-state.

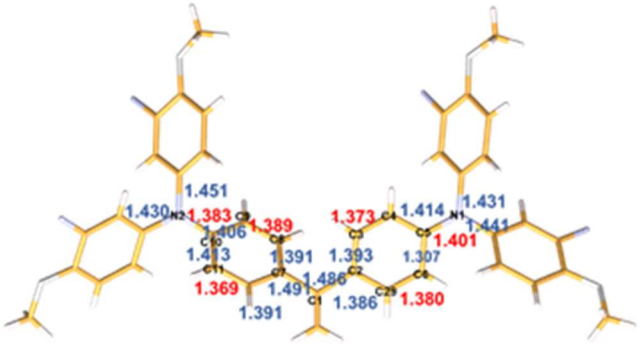

Fig. R6 (i.e., **Fig 1f** in the main text) The conformational isomers in the single-crystal structure of FMTPA-CPA, with selected bond lengths noted. The nitrogen atoms are marked in blue and carbon atoms in yellow.

Above all, the conjugated conducting linker, the stronger donating ability of donor moiety and accepting property of acceptor moiety, and the design of electronic resonance, increase the degree of intramolecular charge redistribution step by step. Especially, the strategy of constructing D-A-D electronic resonance to enhance charge redistribution within SAMs is firstly developed and investigated in our work.

ESR measurements provide the experimental tool for us to monitor the charge distribution in SAMs with different structures. In 2PACz, when the donor moiety carbazole (Cz) and acceptor moiety phosphonic acid (PA) are connected by non-conjugated alkyl chains, negligible ESR signal was observed in **Fig. R7** (i.e., **Fig. 1e** in main text), implying ultra-weak charge redistribution effect. However, when the donor moieties (FTPA and FMTPA) and acceptor moiety (CPA) are connected by a conjugated linker for FTPA-CPA and FMTPA-CPA, the detectable ESR signals demonstrate the radical character, reflects the charge redistribution between donor moiety and acceptor moiety. The more pronounced ESR signal intensity in FMTPA-CPA reflects that the D-A-D electronic resonance structure design induces a more significant charge redistribution, concentrating more negative charge on acceptor CPA anchoring group.

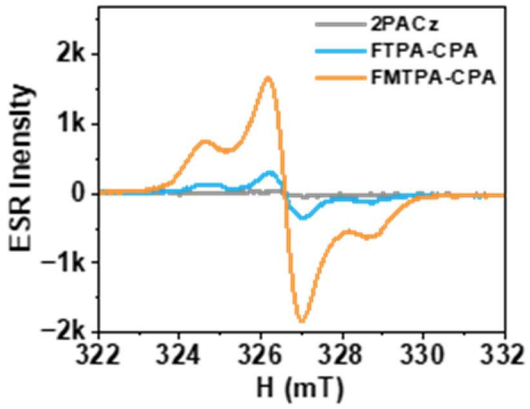

Fig. R7 (i.e., **Fig. 1e** in main text**)** Quantitative ESR spectra of 2PACz, FTPA-CPA and FMTPA-CPA powder.

For the concern that *"the conjugated structures of FTPA–CPA and FMTPA–CAPA shown in Fig. 1a do not represent stable resonance structures"*, we agree with the reviewer's comment. The previously presented structures represent the 1 e electron transfer amount from the donor and acceptor (i.e., a fully charge-separated configuration) in FTPA-CPA and FMTPA-CPA, leading to be energetically unstable. In fact, only partial charge redistribution ($\Delta q < 0.2$ e) occurs within the molecules as previously shown in **Fig. R4**. Following classical organic chemistry principles (F.A. Carey & R.J. Sundberg, *Advanced Organic Chemistry* (Part A: Structure and Mechanisms)), we have revised the resonance structure in **Fig. R3** (i.e., **Fig. 1a** in main text) to present the most stable resonance structures, using the δ^+ and δ^- notation to indicate the partial intramolecular charge redistribution between donor and acceptor moieties.

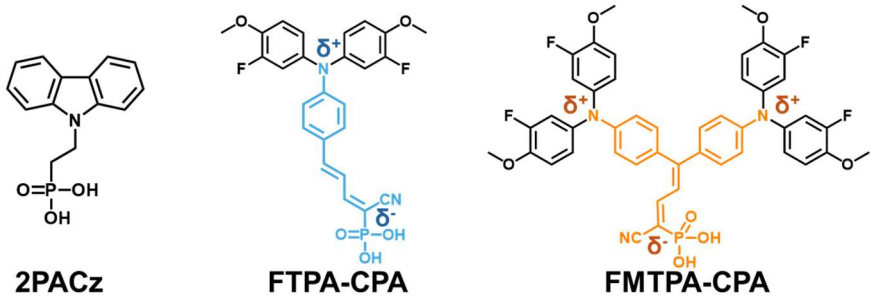

Fig. R3 (i.e., **Fig. 1a** in main text**)** Free molecular structures of 2PACz, FTPA-CPA and FMTPA-CPA (with charge distribution and electronic resonance).

3. The molecular dipole moment reflects the distribution of positive and negative electrical charges within a molecule, which is not directly related to the molecule's intramolecular electron-transfer capacity.

Response: Thanks for the reviewer's comments, which have provided a good opportunity for us to clarify our statements. Our originally description "*Owing to the effective intramolecular electron transfer induced by structure resonance, FMTPA-CPA has substantial dipole moments of 10.5 D*" is somehow misleading. Similar to the response to the above comment 2 of Reviewer #1, with the D-A-D electronic resonance, the significant charge redistribution happens in FMTPA-CPA. Resultingly, more positive charge locates on donor moieties and more negative charge concentrates on anchoring group, which is also consistent with the high ESR signal intensity. According to the definition of the dipole moment:

$$\mu = \Delta q_{D\to A}.R_{D-A}$$

where $\Delta q_{D\to A}$ and R_{D-A} are the amount of electron transfer and the distance from donor to acceptor moieties, respectively. Owing to the largest electron-transfer amount from donor to acceptor moiety in FMTPA-CPA (**Fig. R4** (i.e., **Supplementary Fig. 10** in SI)), it has a large molecular dipole moment of 10.5 D, much larger than that of FTPA-CPA (3.6 D) and 2PACz (2.1 D).

To avoid misleading of the description that causes comments 2 and 3, we revised the corresponding content in the revised manuscript (marked red):

Page 3 in the revised Manuscript: As the SAMs anchoring bond formation is essentially an acid-base condensation with dehydration, enhancing the negative charge density of the coordinating atom serves as the most direct and fundamental strategy to increase acidity and thus strengthening covalent anchoring bond.[25] Although anchoring groups possess fixed chemical structures that are difficult to modify directly, the D-A nature of the SAM benefits from substituent design, providing an important avenue for modifying the anchoring strength.

Rational electronic resonance structure serves as a core strategy for enhancing intramolecular charge redistribution.[26] …

Pages 5~6 in the revised Manuscript: For organic molecules, ultraviolet-visible (UV-vis) absorption spectroscopy and electron spin resonance (ESR) are effective characterization tools for assessing intramolecular charge distribution.[27,28] 2PACz shows a low-intensity absorption edge at ~350 nm and has no ESR signal, implying ultra-weak charge redistribution (~0.042 e, the electron-transfer amount evaluated by our Density functional theory (DFT) calculations in **Supplementary Figs. 9-10**) between the carbazole group and phosphonic acid group (**Figs. 1a & 1d & 1e**). FTPA-CPA exhibits an absorption band with the peak centered at ~490 nm as well as the weak broad peaks in ESR signal. The emergence of ESR signal shows the radical character (**Supplementary Tables 2-3 & Supplementary Note 2**), which reflects higher charge redistribution (~0.115 e) between donor TPA group and acceptor CPA group. In FMTPA-CPA, the further red-shifted absorption peak to ~540 nm and strong broad peaks in ESR signal exhibits the enhanced radical character (**Fig. 1e**), which indicates the more pronounced intramolecular charge redistribution (~0.178 e) between donor moiety and acceptor moiety, resulting in negative charge gathering in CPA group of FMTPA-CPA (**Supplementary Figs. 9-10 & Supplementary Note 2 & Table 2**).

To further explore the origin of the enhanced charge redistribution between donor moiety and acceptor moiety in FMTPA-CPA, we refer to molecular orbital calculations and electrostatic surface potential (ESP) calculations (**Figs. 1b & 1c & Supplementary Fig. 11**). The almost complete overlap of the highest occupied molecular orbital (HOMO) and lowest unoccupied molecular orbital (LUMO) orbital wavefunctions in 2PACz implies a negligible charge redistribution between carbazole group and phosphonic acid group, thus the phosphonic acid group shows negligible negative charge density and the molecular dipole moment is only 2.1 D. For FTPA-CPA, the conjugated linker facilitates charge redistribution between TPA and CPA groups, leading to partial overlapped HOMO and LUMO wavefunction distribution, and higher negative charge density on anchoring group, making the molecular dipole moment increase to 3.6 D. For FMTPA-CPA, we observe less overlap of the HOMO and LUMO wavefunctions, as well as much improved negative charge density on anchoring group and a substantial molecular dipole moment of 10.5 D. At the same time, from the above DFT calculations, we notice the D-A-D electronic resonance across the FMTPA-CPA, which plays a key role in bringing the enhanced charge redistribution.…

4. Phosphonic acid is a strong acid; therefore, the pKa of this type of material is expected to be below 2. The reviewer suggests that the authors remeasure to confirm pKa values.

Response: Thanks for the reviewer's comments. Indeed, pure phosphonic acid in H_2O has pKa value below 2. The relatively-high cid dissociation constant (pKa) value calculated in our work could be due to the low-dielectric ethanol (EtOH) solvent environment and conjugated substitution groups. In addition, the qualitative pKa trend by DFT calculation (**Table R1**) was consistent with the acid-base titration measurements.

We first explore the solvent environment effect on pKa. The experimental pKa of H_3PO_4 (<2) is measured in H_2O, a high-dielectric (ε=81.5) of H_2O that strongly stabilizes the deprotonated conjugate base. Note that the SAMs in this work were prepared using EtOH rather than H_2O, whose lower dielectric constants (ε=25.7) reduce deprotonated conjugate base stabilization and thus result in higher apparent pKa values (*J. Comput. Chem.* 2025, 46, e27517). As shown in **Table R1** (i.e., **Supplementary Table 6** in SI), the calculated pKa_1 values of H_3PO_4 and three SAMs are all higher in EtOH (5.96 for H_3PO_4, 12.84 for 2PACz, 9.59 for FTPA-CPA and 5.80 for FMTPA-CPA) than in H_2O (1.23 for H_3PO_4, 8.26 for 2PACz, 5.34 for FTPA-CPA and 1.66 for FMTPA-CPA). This trend confirms that a lower dielectric constant (EtOH) leads to high pKa values.

Table R1 (i.e., **Supplementary Table 6** in SI) DFT simulations of the acid dissociation constant of phosphonic acid group in different solvents on the 2PACz, FTPA-CPA and FMTPA-CPA.

SAMs	solvent	pKa_1
2PACz	H_2O	8.26
	EtOH	12.84
FTPA-CPA	H_2O	5.34
	EtOH	9.59
FMTPA-CPA	H_2O	1.66
	EtOH	5.80
H_3PO_4	H_2O	1.23
	EtOH	5.96

In addition to solvent effects, **we further explored the effect of the organic substituent (R) attached to the phosphonic group**. For 2PACz, FTPA-CPA and FMTPA-CPA, the R group attached to the phosphonic group result in charge redistribution, thus having impact on the stability of the deprotonated conjugate base (*Angew. Chem. Int. Ed.*, 2018, 57, 4797). The larger charge redistribution degree leads to more stabilized deprotonated conjugate base. Accordingly, the calculated pKa values follow the order of FMTPA-CPA < FTPA-CPA < 2PACz. Specifically, FMTPA-CPA, which contains D-A-D electronic resonance, shows the lowest pKa (1.66 in H_2O, 5.80 in EtOH) due to resonance enhanced charge redistribution effect. Such

substitution-dependent differences confirm the expected trend from electronic resonance characteristic.

At last, **the acid-base titration measurements were conducted to verify the calculated trends** (**Fig. R8** (i.e., **Supplementary Fig. 13** in SI)). The reference H_3PO_4 curve exhibits three distinct buffering regions, consistent with its triprotic nature ($pKa_1 \sim 4.19$). In contrast, 2PACz shows a single, smooth titration transition, characteristic of a weak monoprotic acid ($pKa_1 \sim 9.42$ in H_2O and >11 in EtOH). The titration profiles of FTPA-CPA ($pKa_1 \sim 7.78$ in H_2O and ~ 10.05 in EtOH) and FMTPA-CPA (pKa_1 ~4.92 in H_2O and ~6.31 in EtOH) exhibit similar behavior, with FMTPA-CPA showing lower pKa values. These results agree well with the computational predictions, with minor deviations within experimental uncertainty.

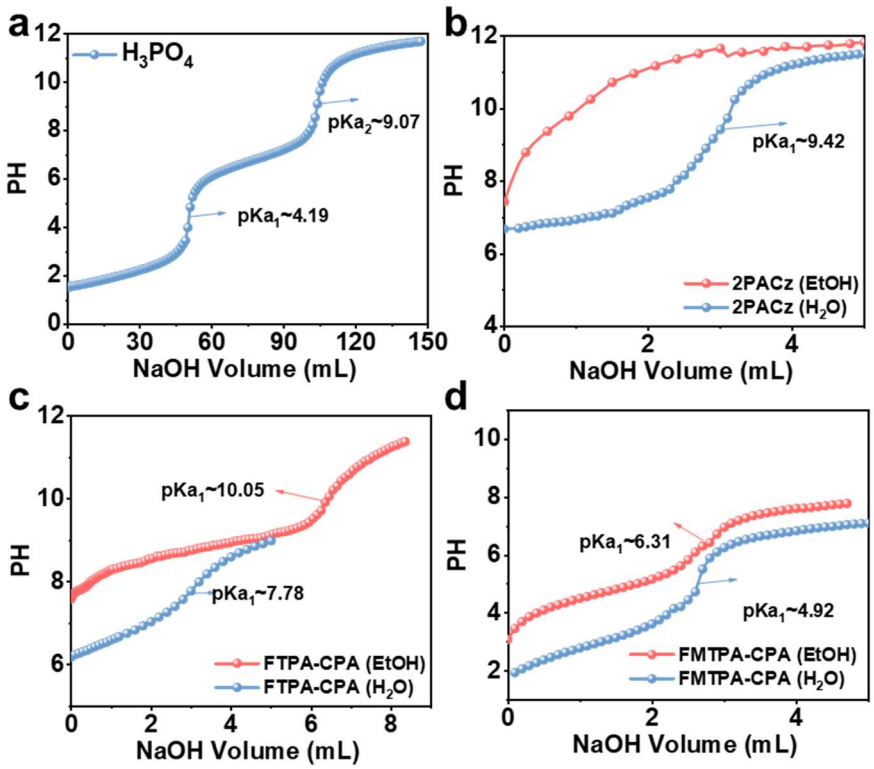

Fig. R8 (i.e., **Supplementary Fig. 13** in SI) The acid-base titration curve of (a) H_3PO_4, (b) 2PACz, (c) FTPA-CPA and (d) FMTPA-CPA.

As a result, we have revised the clarifications about high pKa in the revised Supplementary Information accordingly (marked red). In addition, "EtOH" was included on the y-axis label of the **Fig. 2b** to clarify that the pKa value was obtained from calculations performed in EtOH solvent.

Pages 12~13 in the revised Supplementary Information:

Supplementary Note 4. The acid dissociation constant (pKa) calculation

The pKa was calculated by DFT employing ORCA 6.0.1. The calculation details are shown below:

$$pKa = \left[G_{gas}(A^-) + \Delta G_{sol}(A^-) + G_{gas}(H^+) + \Delta G_{sol}(H^+) - G_{gas}(HA) - \Delta G_{sol}(HA)\right]/1.3644$$

where $G_{gas}(A^-)$, $G_{gas}(HA)$ and $G_{gas}(H^+)$ are the represents the gas free energy of corresponding material. $\Delta G_{sol}(A^-)$, $\Delta G_{sol}(HA)$ and $\Delta G_{sol}(H^+)$ are the represents the solvation free energy of corresponding materials, among that $G_{gas}(H^+)$ and $\Delta G_{sol}(H^+)$ are obtained from experiment data. The gas free energy calculated at B3LYP-D3(BJ)/ma-def2-TZVP//B3LYP-D3(BJ)/def2-SVP level and the solvation free energy was calculated at M052X/6-31G* in SMD solvation model.

In this work, the SAMs were prepared using ethanol (EtOH), thus our calculations were performed in EtOH environments, whose lower dielectric constants reduce conjugated base stabilization and thus result in higher apparent pKa values compared with H_2O (**Supplementary Table 6**). For 2PACz, FTPA-CPA and FMTPA-CPA, the substituents (R) attached to the phosphonic group result in charge redistribution, thus having impact on the stability of the deprotonated conjugate base. FMTPA-CPA, which contains D-A-D electronic resonance, shows the lowest pKa (1.66 in H_2O, 5.80 in EtOH) due to resonance enhanced charge redistribution effect. Therefore, both solvent dielectric and molecular substitution groups have large impact on the pKa value of phosphonic acid group in SAMs compared to pristine H_3PO_4. In addition, the acid-base titration results agree well with the computational predictions, with minor deviations within experimental uncertainty (**Supplementary Fig. 13**).

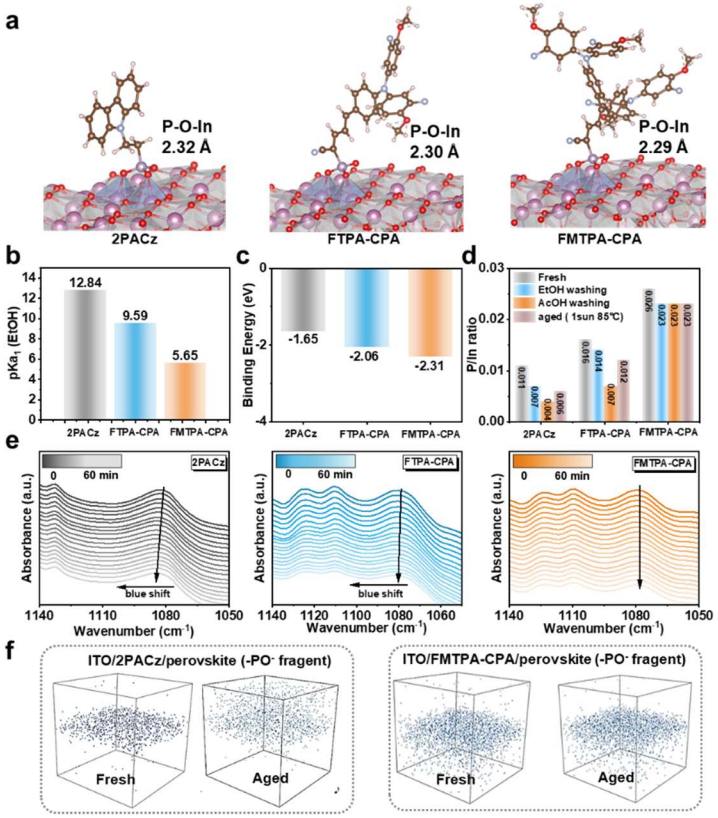

Fig. 2| Robust anchoring to substrate of D-A-D resonant SAM. a, DFT calculation of the anchoring binding energy of 2PACz, FTPA-CPA and FMTPA-CPA with ITO. The

blue regions are the -P-O-In bonds in SAMs bonded with ITO. **b,** DFT simulations of the acid dissociation constant of phosphonic acid group on the 2PACz, FTPA-CPA and FMTPA-CPA. **c,** The binding energies of 2PACz, FTPA-CPA and FMTPA-CPA SAM on ITO substrate. **d,** The P/In ratio by XPS spectroscopy of 2PACz, FTPA-CPA and FMTPA-CPA on ITO substrate. **e,** *In-situ* FTIR spectra of the 2PACz, FTPA-CPA and FMTPA-CPA films with AcOH washing on ITO substrate at 85℃. **f,** The $-PO^-$ signal intensity by ToF-SIMs of ITO/2PACz/perovskite and ITO/FMTPA-CPA/perovskite before and after aging under high-temperature and illumination.

5. The surface energy alignment and charge extraction of the SAM-deposited substrate are determined by the molecular dipole moments of the SAM molecules, rather than by their electron resonance properties.

Response: For this comment, we think that our original description leads to some misleading here. We agree with that the molecular dipole moment determines *the surface energy alignment and charge extraction*, which is also confirmed by numerous previous reports (*Nature*, 2025, 646, 95; *Science*, 2021, 372, 618; *Nat. Photonics*, 2024 18, 1269).

What we want to address here is that the large molecular dipole moment of FMTPA-CPA originates from the D-A-D electronic resonance structure. As we explained in the Response to Comment 2 and 3 of Reviewer #1, the enhanced electronic resonance in FMTPA-CPA lead to more pronounced charge redistribution between donor and acceptor moieties and more negative charge concentration on CPA group, resulting in larger molecular dipole moment.

To avoid misleading of the description, we revise the corresponding content in the revised manuscript (marked red):

Page 10 in the revised Manuscript: From the ultraviolet photoelectron spectroscopy (UPS), the energy difference between the HOMO level and Fermi-level of FMTPA-CPA is similar to that of perovskite, reducing the energy mismatch for hole extraction (**Supplementary Fig. 45**). The energy diagram results imply that the D-A-D resonance leads to larger dipole moment, which ameliorates the band alignment between SAMs and perovskite layer. As a result, the resonant FMTPA-CPA molecule exhibits continuous charge distributions between the molecule and ITO substrate, facilitate carrier extraction more effectively across the interface.[34]

6. Regarding device performance, the authors only provide the PCE of the champion devices; other performance parameters and device PCEs under different conditions should also be included in the manuscript for comparison. In addition, for the stability measurements, the authors should report the initial performance of the devices.

Response: Thanks for the reviewer's suggestions. Detailed performance parameters (open-circuit voltage (V_{oc}), short-circuit current density (J_{sc}), fill factor (FF), power conversion efficiency (PCE)) have been provided in **Table R2 (**i.e., **Supplementary Table 11** in SI**)**. For device PCEs under different conditions, we added 2PACz and FTPA-CPA-based device performance data of small-area rigid devices in page 11 of the manuscript for better comparison. In addition, we also added the 2PACz- and

FTPA-CPA-based small-area flexible devices and the large-are flexible modules performance data in the revised Supplementary Information considering the limited space of the paper, as shown in **Table R2** (i.e., **Supplementary Table 11** in SI) **& Fig. R9** (i.e., **Supplementary Fig. 69** in SI) **& Fig. 4b**.

To follow the suggestions that "*for the stability measurements, the authors should report the initial performance of the devices*", we have provided initial performance of devices applied in the stability measurement in **Table R3** ((i.e., **Supplementary Table 17** in SI), these initial PCE values are measured under AM 1.5G illumination, the light emitting diode (LED), light emitting plasma (LEP), metal halide lamp (MH) solar simulator, 100 mW cm^{-2}). To more accurately evaluate the stability of the devices, the normalized PCE decay curves were replaced with the absolute PCE stability curves (**Fig. 4d-4g, Supplementary Figs. 58 & 60-64**).

We have added the 2PACz and FTPA-CPA-based performance of small-area rigid devices in the the revised manuscript (marked red):
Page 11 in the revised Manuscript: In contrast, the devices based on 2PACz and FTPA-CPA SAMs only achieve PCE of 26.40% and 25.57%, respectively.

[Figure Redacted]

Fig. 4| Enhanced efficiency and stability based on D-A-D resonant SAM. a, *J–V* curves of the champion small-area (0.063 cm^2) pero-SCs based on 2PACz, FTPA-CPA and FMTPA-CPA under AM1.5G 100 mW cm^{-2} illumination in the reverse and forward scan. **b,** *J-V* curves of the flexible small-area (0.063 cm^2) pero-SCs based 2PACz, FTPA-CPA and FMTPA-CPA under AM1.5G 100 mW cm^{-2} illumination in the reverse and forward scan. Inset: a picture of the flexible device. **c,** Statistical of the devices area and the PCE values obtained from the recently reported high-performance rigid and

flexible p-i-n pero-SCs based on SAMs. **d,** Thermal stabilities of the 2PACz, FTPA-CPA and FMTPA-CPA-based pero-SCs at 85±5°C in N_2 atmosphere following ISOS-D-2 protocol. **e,** MPPT of the pero-SCs based on 2PACz, FTPA-CPA and FMTPA-CPA at 85±5°C under a simulated continuous 1 Sun equivalent illumination in an N_2 atmosphere following ISOS-L-2 protocol. **f,** MPPT stability of small-area devices based on 2PACz, FTPA-CPA and FMTPA-CPA at 85±5°C under the illumination of MH lamp (100 mW cm^{-2}, 4.4% UV inside). **g,** Thermal cycling aging of the pero-SCs based on 2PACz, FTPA-CPA and FMTPA-CPA from –40 °C to 85 °C under dark following ISOS-T-3 protocol.

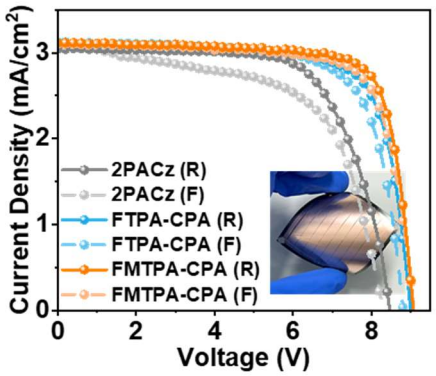

Fig. R9 (i.e., **Supplementary Fig. 69** in SI) *J-V* curves of the champion flexible large-area (15.64 cm^2) modules based FMTPA-CPA. Inset: a picture of the flexible 5×5 cm^2 module.

Table R2 (i.e., **Supplementary Table 11** in SI) Photovoltaic parameters of pero-SCs under AM1.5G, 100 mW/cm^2 illumination. Forward scan: −0.2 V→1.2 V (small-area), −0.5 V→9.5 V (large-area); Reverse scan: 1.2 V→−0.2 V (small-area), 9.5 V→−0.5 V (large-area).

Substrate type	SAMs	Scan direction	V_{oc} (V)	J_{sc} (mA/cm^2)	FF (%)	PCE_{max}[a](PCE_{avg})[a] (%)
Glass/ITO (0.063 cm^2)	2PACz	Reverse	1.18 (1.17±0.02)	26.46 (26.50±0.15)	81.9 (81.9±1.8)	25.57 (25.30±0.20)
		Forward	1.18 (1.16±0.02)	26.47 (26.48±0.13)	79.3 (79.0±1.7)	24.77 (24.35±0.30)
	FTPA-CPA	Reverse	1.19 (1.20±0.02)	26.44 (26.53±0.12)	83.9 (82.6±1.4)	26.40 (26.21±0.14)
		Forward	1.19 (1.19±0.01)	26.57 (26.49±0.13)	79.5 (79.2±1.1)	25.14 (24.91±0.19)
	FMTPA-CPA	Reverse	1.20 (1.20±0.01)	26.59 (26.52±0.10)	86.6 (86.5±0.2)	27.69 (27.62±0.07)
		Forward	1.20 (1.20±0.01)	26.75 (26.65±0.11)	83.3 (82.9±0.5)	26.81 (26.65±0.09)
Glass/ITO (15.64 cm^2)	2PACz	Reverse	8.58 (8.46±0.19)	3.11 (3.10±0.02)	69.3 (69.3±1.0)	18.49 (18.17±0.22)
		Forward	8.37 (8.28±0.15)	3.10 (3.10±0.01)	68.5 (68.0±1.3)	17.77 (17.46±0.21)

	FTPA-CPA	Reverse	8.88 (8.83±0.09)	3.19 (3.18±0.01)	77.0 (76.8±1.0)	21.81 (21.54±0.19)
		Forward	8.87 (8.79±0.09)	3.20 (3.20±0.02)	74.5 (74.3±0.8)	21.15 (20.92±0.16)
	FMTPA-CPA	Reverse	9.00 (9.01±0.08)	3.25 (3.24±0.02)	80.8 (80.6±0.8)	23.63 (23.48±0.08)
		Forward	8.96 (8.94±0.09)	3.24 (3.23±0.02)	79.1 (78.9±0.8)	22.96 (22.80±0.06)
PET/ITO (0.063 cm^2)	2PACz	Reverse	1.17 (1.17±0.02)	25.62 (25.64±0.07)	81.2 (80.3±0.9)	24.35 (23.88±0.22)
		Forward	1.17 (1.16±0.01)	25.04 (25.18±0.07)	79.7 (78.6±0.9)	23.35 (22.95±0.19)
	FTPA-CPA	Reverse	1.19 (1.19±0.01)	25.81 (25.85±0.05)	83.3 (81.9±0.7)	25.58 (25.09±0.20)
		Forward	1.18 (1.17±0.01)	25.88 (25.88±0.08)	80.0 (79.8±0.5)	24.42 (24.25±0.10)
	FMTPA-CPA	Reverse	1.21 (1.20±0.01)	26.17 (26.19±0.09)	84.4 (84.2±0.9)	26.64 (26.45±0.13)
		Forward	1.21 (1.20±0.01)	25.88 (26.04±0.08)	83.9 (83.5±0.7)	26.21 (26.03±0.11)
PET/ITO (15.64 cm^2)	2PACz	Reverse	8.46 (8.23±0.10)	3.11 (3.12±0.01)	64.8 (64.0±0.5)	17.06 (16.48±0.16)
		Forward	8.30 (8.02±0.12)	3.07 (3.10±0.01)	61.4 (61.1±0.5)	15.63 (15.22±0.14)
	FTPA-CPA	Reverse	8.98 (8.78±0.09)	3.14 (3.13±0.01)	74.7 (75.0±0.6)	21.07 (20.64±0.14)
		Forward	8.80 (8.65±0.11)	3.13 (3.13±0.01)	72.9 (72.8±0.8)	20.08 (19.69±0.13)
	FMTPA-CPA	Reverse	9.07 (9.08±0.06)	3.14 (3.14±0.01)	77.9 (77.5±0.5)	22.18 (22.12±0.06)
		Forward	9.07 (9.05±0.07)	3.14 (3.14±0.01)	75.4 (75.3±0.5)	21.46 (21.41±0.05)

[a] The maximum PCE, average PCE, and standard deviations of 20 devices

Table R3 (i.e., **Supplementary Table 17** in SI) The initial photovoltaic parameters of pero-SCs under different stability protocols (measured under AM 1.5G illumination, the light emitting diode (LED), light emitting plasma (LEP), metal halide lamp (MH) solar simulator, 100 mW cm^{-2}).

protocols	SAMs	V_{oc} (V)	J_{sc} (mA/cm^2)	FF (%)	PCE (%)
ISOS-D-2	2PACz	1.16±0.01	26.45±0.08	80.4±0.7	24.66±0.25
	FTPA-CPA	1.18±0.01	26.57±0.13	82.1±0.3	25.70±0.18
	FMTPA-CPA	1.20±0.01	26.59±0.05	83.5±0.3	26.68±0.19
ISOS-T-3	2PACz	1.16±0.01	26.45±0.08	80.5±0.7	24.70±0.26
	FTPA-CPA	1.19±0.01	26.47±0.08	82.1±0.5	25.74±0.22
	FMTPA-CPA	1.20±0.01	26.59±0.07	83.4±0.3	26.69±0.20
ISOS-L-2	2PACz	1.16±0.01	25.81±0.12	80.8±0.5	24.19±0.28

	FTPA-CPA	1.19±0.01	25.89±0.07	82.8±0.4	25.44±0.17
	FMTPA-CPA	1.20±0.01	25.99±0.08	83.9±0.4	26.25±0.13
ISOS-LC-1	2PACz	1.16±0.01	25.69±0.10	80.6±0.5	24.11±0.25
	FTPA-CPA	1.19±0.01	25.78±0.08	82.3±0.5	25.17±0.15
	FMTPA-CPA	1.21±0.01	25.90±0.04	83.3±0.7	26.00±0.11
ISOS-D-3	2PACz	1.16±0.01	26.39±0.12	80.3±0.5	24.59±0.22
	FTPA-CPA	1.18±0.01	26.45±0.10	82.3±0.6	25.77±0.11
	FMTPA-CPA	1.20±0.01	26.56±0.06	83.8±0.8	26.74±0.15
UV irradiation	2PACz	1.17±0.01	26.46±0.09	80.5±0.4	24.89±0.25
	FTPA-CPA	1.19±0.01	26.51±0.08	81.8±0.6	25.82±0.08
	FMTPA-CPA	1.20±0.01	26.58±0.05	83.9±0.6	26.84±0.10
MPPT (MH lamp)	2PACz	1.17±0.01	25.55±0.09	80.2±0.7	23.91±0.29
	FTPA-CPA	1.19±0.01	25.58±0.07	82.1±0.7	25.01±0.17
	FMTPA-CPA	1.21±0.01	25.69±0.03	84.0±0.8	26.02±0.13
MPPT at 85±5°C (LEP lamp)	2PACz	1.17±0.01	25.90±0.14	80.8±0.7	24.46±0.31
	FTPA-CPA	1.19±0.01	26.01±0.07	81.5±0.9	25.25±0.20
	FMTPA-CPA	1.21±0.01	26.06±0.06	83.7±0.8	26.30±0.12
MPPT at 85±5°C (MH lamp)	2PACz	1.17±0.01	25.69±0.07	80.9±0.9	24.26±0.28
	FTPA-CPA	1.19±0.01	25.73±0.06	81.9±0.6	25.04±0.16
	FMTPA-CPA	1.21±0.01	25.78±0.05	83.6±0.8	26.01±0.10

The average PCE, and standard deviations of 10 devices.

Response to Reviewer #2:

Authors report a significant advancement on both power conversion efficiency and operation stability through designing a novel self-assembly molecule with resonant structure. Thus, the originality of this study is a novel SAM molecule, FMTPA-CPA, in which the resonant charge delocalization facilitates efficient carrier transport and the electronic resonance strengthens the phosphonic acid-ITO anchoring bond to prevent the SAM molecule desorption during operation. As a result, the inverted perovskite solar cells with this SAM molecule shows a certified efficiency of 27.45% with excellent stability even under various conditions. Research on SAMs is highly active, focusing on reinforcing SAMs or solving interfacial issues with perovskites. Unlike previous studies, this manuscript focuses on the desorption from ITO, which is undoubtedly a novel and significant issue. Very recently, a study addressing an issue similar to this manuscript was published in Science (10.1126/science. adz7969). This paper not only reports long-term stability in a harsher environment (light including UV + thermal stress) than this manuscript, but also presents long-term stability in large-area modules. Although this manuscript reports a record-high efficiency exceeding 27%, the long-term stability results remain largely similar to those of previously reported studies (e.g., 10.1038/s41586-025-09509-7). Consequently, the actual effect of the proposed resonance-enhanced structure in improving long-term durability remains unclear. While the recent Science report identifying UV light as a critical degradation factor, this manuscript lacks experimental validation under UV-inclusive environments. Thus, the current version does not sufficiently demonstrate the extraordinary conceptual advancement required for Nature. Thus, for publication in Nature, authors should substantially revise the manuscript to provide stronger evidence and new scientific insights that clearly distinguish this study from the recent science paper.

Response: Thanks for the reviewer's positive evaluation of our work that "*Unlike previous studies, this manuscript focuses on the desorption from ITO, which is undoubtedly a novel and significant issue*". For the valuable suggestions and comments, we have added more comprehensive measurements and discussions, based on which the quality of our work has been further improved. The detailed point-to-point responses are provided below.

1. Recent studies have already reported perovskite solar cells with exceptional stability under combined LED and thermal stress (10.1038/s41586-025-09509-7). However, a very recently published Science paper (10.1126/science. adz7969) reports UV light as the primary cause of bond dissociation between ITO and SAMs. This is a critical consideration as actual operating environments inevitably include UV exposure. Nevertheless, this manuscript lacks experimental results addressing this issue. Therefore, experimental verification is required to demonstrate whether the developed SAM maintains a stable bond with ITO under UV light or a combined environment of light including UV and heat.

Response: Thanks for the reviewer's valuable comments. As recently published *Science* paper (10.1126/science. adz7969) stated, *UV light acts as the primary cause of*

bond dissociation between ITO and SAMs. To address this concern, we performed the stability measurements under UV light (365 nm, 56 mW cm^{-2}) illumination in a N_2 glovebox, and combined environment of light including UV (LEP (1.4% UV inside), MH (4.4% UV inside)) and heat (85±5ºC).

As shown in **Fig. R10** (i.e., **Supplementary Fig. 58** in SI), the FMTPA-CPA-based device can maintain ~81% of their initial efficiency after 1,080 h under UV illumination (365nm, 56mW cm^{-2}), whereas only 62% and 43% of the initial efficiency is retained for the FTPA-CPA and 2PACz-based devices after 700 h. These results clearly demonstrate that FMTPA-CPA forms a much more robust interfacial bond with ITO against UV-induced bond cleavage. Importantly, **Table R4** (i.e., **Supplementary Table 16** in SI) suggest that the UV stability of our devices maintain relatively improved UV stability compared with recently reported perovskite solar cells tested under similar UV stress conditions. This comparative analysis highlights the outstanding long-term UV tolerance achieved through the resonant FMTPA-CPA molecular design.

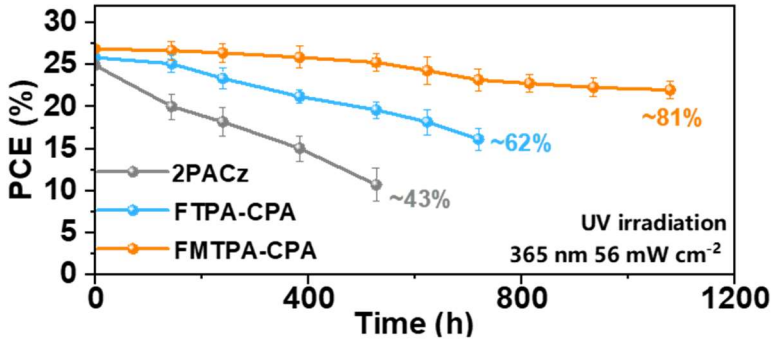

Fig. R10 (i.e., **Supplementary Fig. 58** in SI) The UV irradiation stability at 365 nm (56 mW cm^{-2}) of small-area devices based on 2PACz, FTPA-CPA and FMTPA-CPA.

Table R4 (i.e., **Supplementary Table 16** in SI) Statistical of the UV irradiation stability in references.

Ref.	Initial PCE	Power (mW cm^{-2})	Time (h)	PCE decay
This work	26.84%	56.0	1080	81%
Nature, 2023, 623, 313	25.5%	0.1	1100	95%
Sci. Adv., 2025, 11, eadu3493	26.0%	17.0	500	80%
Joule, 2024, 8, 11, 3142	26.32%	--	110	90%
Adv. Energy Mater., 2025, 15, 2501296	24.68%	50	130	80%
Adv. Funct. Mater., 2024, 34, 2400474	24.73%	50	380	90%
Chem. Eng. J., 2024, 497, 154552	22.46%	50	250	91%

In addition, as suggested by the reviewer, we evaluated device stability under a combined environment of UV-inclusive light and heat (85±5ºC) as shown in **Fig. R11** (i.e., **Supplementary Fig. 61** in SI). The maximum-power-point tracking (MPPT) tests were conducted under 100 mW cm^{-2} LEP light (1.4% UV inside, the spectrum is shown

in **Fig. R12a** (i.e., **Supplementary Fig. 59a** in SI)) exposure at 85±5ºC in N_2 atmosphere, with the FMTPA-CPA-based device maintaining 95% of its initial efficiency after continuous maximum-power-point tracking (MPPT) for 1,080 h, whereas the 2PACz-based and FTPA-CPA-based devices fall to below 44% and 80% of their initial efficiency after 600 h (**Fig. R11a** (i.e., **Supplementary Fig. 61a** in SI)). In addition, under 100 mW cm^{-2} MH light (4.4% UV inside, the spectrum is shown in **Fig. R12b** (i.e., **Supplementary Fig. 59b** in SI)) exposure at 85±5ºC in N_2 atmosphere, the standard MPPT tests reveal that the FMTPA-CPA-based devices retains ~93% after 1,080 h whereas the 2PACz-based and FTPA-CPA-based devices fall to below 26% and 74% of their initial efficiency after 600 h (**Fig. R11b** (i.e., **Supplementary Fig. 61b** in SI)). These UV-inclusive light and heat stability results are comparable with the recent *Science* paper (10.1126/science. adz7969), demonstrating the practical durability of devices using the D-A-D resonant SAM.

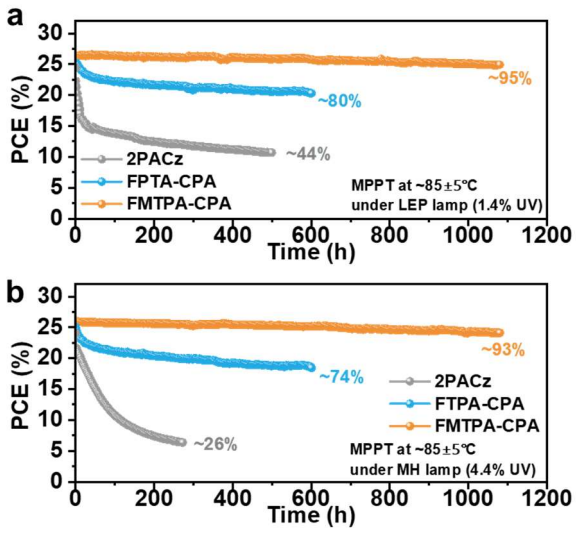

Fig. R11 (i.e., **Supplementary Fig. 61** in SI) Light-soaking stability of small-area devices (MPPT conditions at 85±5°C) based on 2PACz, FTPA-CPA and FMTPA-CPA under the illumination of (a) LEP lamp (100 mW cm^{-2}, 1.4% UV inside) and (b) MH lamp (100 mW cm^{-2}, 4.4% UV inside) in N_2 atmosphere.

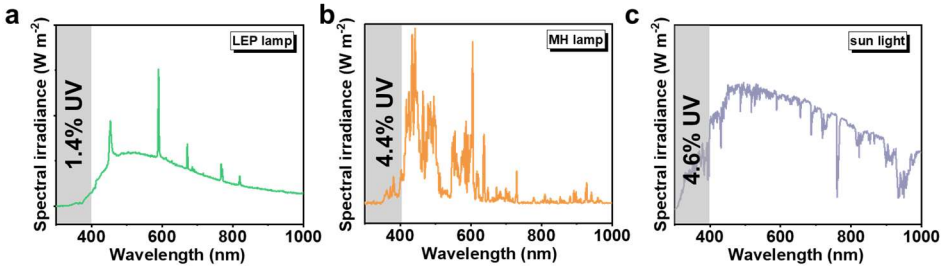

Fig. R12 (i.e., **Supplementary Fig. 59** in SI) Spectrum of the light source for light-soaking stability tests (a) LEP lamp; (b) MH lamp and (c) sunlight. The inset showed the UV ratio of the lamp in each spectrum.

We have added UV illumination and a combined environment of light including UV and thermal stress in the revised Manuscript (**Fig. 4f**) and revised Supplementary Information (marked red):

Page 12 in the revised Manuscript: To evaluate the industrial potential of D-A-D resonant FMTPA-CPA-based devices, we conduct more stability test according to protocols that mimic the real operation process. Considering UV light is the primary cause of bond dissociation between ITO and SAMs, we measure the UV illumination stability of devices under UV light (365 nm, 56 mW cm^{-2}) in a N_2 filled glovebox (**Supplementary Fig. 58 & Table 16**). The FMTPA-CPA-based device can maintain ~81% of their initial efficiency after 1,080 h while the FTPA-CPA and 2PACz-based devices retain only 62% and 43%, respectively, after 700 h. In addition, we evaluate device stability under a combined environment of UV-inclusive light (metal halide (MH) lamp, 100 mW cm^{-2}, 4.4% UV inside, the spectrum in **Supplementary Fig. 59**) and thermal stress (85±5ºC). The FMTPA-CPA-based device maintains 93% of its initial efficiency during continuous MPPT for 1,080 h, while the FTPA-CPA and 2PACz-based devices retain only 74% and 26% after 600 h (**Fig. 4f & Supplementary Fig. 60 & Fig. 61 &** more details of UV-inclusive stability can be found in **Supplementary Note 10**), demonstrating that the D-A-D resonance molecular design strategy substantially enhances practical photothermal stability under realistic UV-inclusive conditions.[17]

Page 18 in the revised Supplementary Information:

Supplementary Note 10 the stability of combined environment of light including UV and heat

We also evaluate device stability under a combined environment of UV-inclusive light and heat (85±5ºC) as shown in **Supplementary Fig. 61**. The maximum-power-point tracking (MPPT) tests were conducted under 100 mW cm^{-2} LEP light (1.4% UV inside, the spectrum is shown in **Supplementary Fig. 59a** exposure at 85±5ºC in N_2 atmosphere, with the FMTPA-CPA-based device maintains 95% of its initial efficiency during continuous MPPT for 1,080 h, whereas the 2PACz-based and FTPA-CPA-based devices fall to below 44% and 80% of their initial efficiency after 600 h (**Supplementary Fig. 61a**). These UV-inclusive light and heat stability results are comparable with the state-of-the-art results,[26] demonstrating the practical durability of devices using the D-A-D resonant SAM.

[Figure Redacted]

Fig. 4| Enhanced efficiency and stability based on D-A-D resonant SAM. a, *J–V* curves of the champion small-area (0.063 cm^2) pero-SCs based on 2PACz, FTPA-CPA and FMTPA-CPA under AM1.5G 100 mW cm^{-2} illumination in the reverse and forward scan. **b,** *J-V* curves of the flexible small-area (0.063 cm^2) pero-SCs based 2PACz, FTPA-CPA and FMTPA-CPA under AM1.5G 100 mW cm^{-2} illumination in the reverse and forward scan. Inset: a picture of the flexible device. **c,** Statistical of the devices area and the PCE values obtained from the recently reported high-performance rigid and flexible p-i-n pero-SCs based on SAMs. **d,** Thermal stabilities of the 2PACz, FTPA-CPA and FMTPA-CPA-based pero-SCs at 85±5°C in N_2 atmosphere following ISOS-D-2 protocol. **e,** MPPT of the pero-SCs based on 2PACz, FTPA-CPA and FMTPA-CPA at 85±5°C under a simulated continuous 1 Sun equivalent illumination in an N_2 atmosphere following ISOS-L-2 protocol. **f,** MPPT stability of small-area devices based on 2PACz, FTPA-CPA and FMTPA-CPA at 85±5°C under the illumination of MH lamp (100 mW cm^{-2}, 4.4% UV inside). **g,** Thermal cycling aging of the pero-SCs based on 2PACz, FTPA-CPA and FMTPA-CPA from –40 °C to 85 °C under dark following ISOS-T-3 protocol.

2. While this manuscript addresses SAM desorption through a resonance-enhanced structure, it lacks a critical qualitative distinction between covalent and hydrogen bonding. As established in recent Science paper, ensuring robust covalent anchoring is essential to prevent UV-induced bond decomposition and subsequent chemical degradation of the perovskite. The current evidence, based on ethanol washing, is insufficient to demonstrate the formation of these critical covalent bonds as opposed to mere hydrogen bonding. Therefore, additional verification, such as acid-washing tests, is required to demonstrate that the resonance effect fundamentally promotes stable

covalent anchoring.

Response: Thanks for the reviewer's comments that help us to deepen the understanding of the SAM anchoring mechanism. We confirmed that the D-A-D resonant FMTPA-CPA achieves robust and stable covalent anchoring through acid-washing (boric acid (H_3BO_3) and acetic acid (AcOH)) tests referring to the recently published *Science* paper (10.1126/science. adz7969).

To demonstrate a critical qualitative distinction between covalent and hydrogen bonding of SAMs, we conducted a washing process with H_3BO_3 and AcOH as shown in **Fig. R13 & Fig. R15** (i.e., **Supplementary Fig. 16** in SI) **& Table R5** (i.e., **Supplementary Table 7** in SI). After acid treatment, the substrates were annealed at 150°C for 10 min to ensure complete removal of residual acid. To quantify the change in the amount of SAM molecules from the ITO substrate, we performed X-ray photoelectron spectroscopy (XPS) measurement of SAMs before and after acid (H_3BO_3 and AcOH) treatment (**Fig. R13**). The P/In signal ratio of 2PACz decreased from the initial value of 0.011 to 0.006 and 0.004 after H_3BO_3 and AcOH acid washing, respectively; the P/In signal ratio in FTPA-CPA declined from the initial value of 0.016 to 0.009 and 0.007 after H_3BO_3 and AcOH acid washing. In contrast, the much higher P/In (0.023) remained almost unchanged after H_3BO_3 and AcOH acid washing, indicating that the FMTPA-CPA majorly forms a more robust covalent anchoring compared with 2PACz and FTPA-CPA.

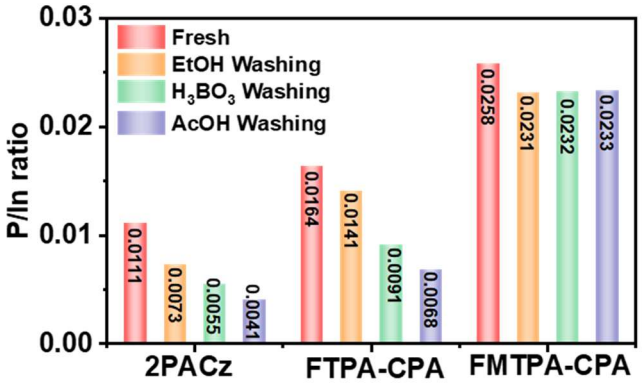

Fig. R13 The P/In ratio by XPS spectroscopy of 2PACz, FTPA-CPA and FMTPA-CPA on ITO substrate without any post-treatment, with ethanol washing, H_3BO_3 washing and AcOH washing post-treatment.

To more precisely evaluate the bonding characteristics of ITO/SAMs, we conducted the scanning electrochemical cell microscopy-thin-layer cyclic voltammetry (SECCM-TLCV) before and after AcOH washing as shown in **Fig. R14** (i.e., **Supplementary Fig. 18** in SI). The SECCM-TLCV measurement, which has high sensitivity and signal-to-noise ratio, facilitates accurate determinations of molecular assembly density. The assembly densities mapping reveal that 2PACz exhibits an uneven distribution, whereas FTPA-CPA demonstrates improved uniformity, and FMTPA-CPA shows the highest assembly density and overall uniformity. After AcOH acid washing, both 2PACz and FTPA-CPA samples show decreased assembly density, whereas FMTPA-CPA sample

remains almost unchanged. This further indicates that 2PACz and FTPA-CPA forms partial hydrogen bonding while FMTPA-CPA majorly forms the robust covalent anchoring.

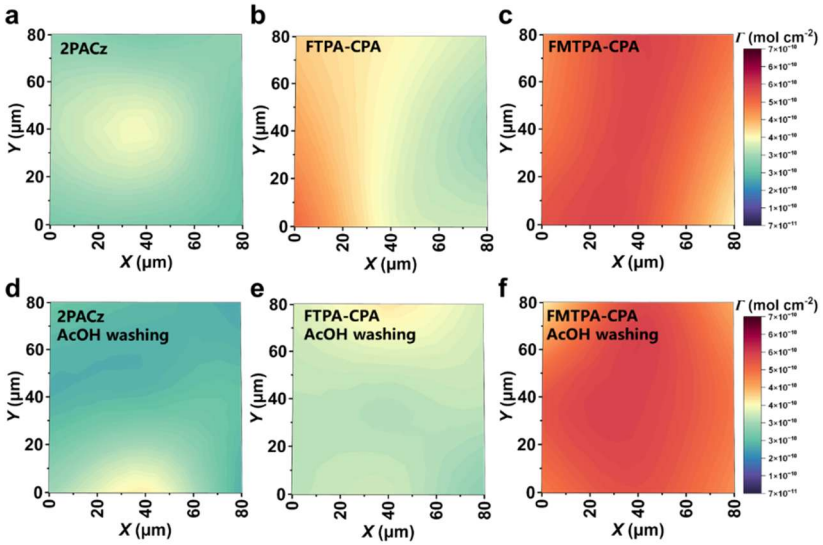

Fig. R14 (i.e., **Supplementary Fig. 18** in SI) Assembly densities mapping of (a) 2PACz, (b) FTPA-CPA and (c) FMTPA-CPA obtained from SECCM-TLCV. Assembly densities mapping of (d) 2PACz, (e) FTPA-CPA and (f) FMTPA-CPA after AcOH washed obtained from SECCM-TLCV.

The corresponding revisions for the revised Manuscript (marked red) are listed below:

Pages 6~7 in the revised Manuscript:

Robust covalent anchoring onto substrate of D-A-D resonant SAM

The large molecular dipole moment and concentrated negative charge on the CPA group leads to robust covalent anchoring strength of FMTPA-CPA onto ITO substrate (**Fig. 2a**). The chemical bonding between the anchoring groups and the ITO substrates is essentially an acid-base reaction (**Supplementary Fig. 12**). The acid dissociation constant (pK_a) of phosphonic acid anchoring group of the FMTPA-CPA SAM is much higher than that of FTPA-CPA and 2PACz (**Fig. 2b & Supplementary Fig. 13 & Table 6 & Note 4**), facilitating its degree of deprotonation. As a result, the P-O-In covalent anchoring bond lengths for 2PACz and FTPA-CPA are 2.32 Å and 2.30 Å on ITO surface, with corresponding binding energy of only –1.65 eV and –2.06 eV, respectively (**Figs. 2a & 2c & Supplementary Fig. 14**). For comparison, the P-O-In length and molecular binding energy of FMTPA-CPA with ITO are 2.29 Å and –2.31 eV, demonstrating their shorter bond length and stronger covalent bonding strength. The enhanced anchoring strength of FMTPA-CPA can be further verified by the remained much higher P/In signal ratio in X-ray photoelectron spectroscopy (XPS) after ethanol washing, even boric acid (H_3BO_3) and acetic acid (AcOH) washing, compared to that of 2PACz and FTPA-CPA (**Fig. 2d & Supplementary Figs. 15-17 & Table 7 & Note 7**).[31] Furthermore, the scanning electrochemical cell microscopy-thin-layer cyclic voltammetry (SECCM-TLCV) measurement indicates the FMTPA-CPA sample possesses uniformly high molecular assembly density, and the anchored molecular

density is well sustained even after AcOH washing (**Supplementary Fig. 18**).

Page 17~18 in the revised Supplementary Information:

Supplementary Note 9. Electrochemical measurement details

Quartz capillaries (I.D./O.D., 0.7/1.0 mm) were drawn into micropipettes with a diameter of 20 μm using an ultra-high temperature puller (MT-PULLER100A). In the SECCM-TLCV experiment, ITO/SAM was used as ITO/SAM was used as the working electrode (WE), Ag wire served as the quasi-reference-counter (QRCE), and a quartz micropipette filled with 0.1 M TBAP in ACN was employed as the SECCM probe. To carry out the SECCM-TLCV experiment, the quartz micropipette with the meniscus was moved to approximately 30 μm above the ITO/SAM. The threshold for surface current feedback is set at 120% to determine when the meniscus contacts the surface of the WE and to stop further movement. Local-CV curves were recorded within the hemispherical droplet formed between the SECCM tip and the WE surface. SECCM images (80 × 80 μm^2 scan area) obtained with the voltametric hopping mode "SECCM + local-CV" protocol, visualizing assembly density distribution of SAMs on ITO.

All localized micro-area electrochemical measurements were conducted using a super-resolution electrochemical microscopy system, with SPRM v1.0 software provided by MinTech (MT-SRECM300 Pro, CAS Applied Chemistry Science & Technology Co. Ltd., Changchun). The experimental setup was installed inside a Faraday cage and placed on a pneumatic damping antivibration platform.

Assembly density (Γ_0) of the SAMs was calculated according to the CV data.

$$\Gamma_0 = \frac{Q}{nFA}$$

Where Q is the integrated charge, n is the electron transfer number for SAMs oxidation, F is the Faraday constant, and A is the geometric area of WE.

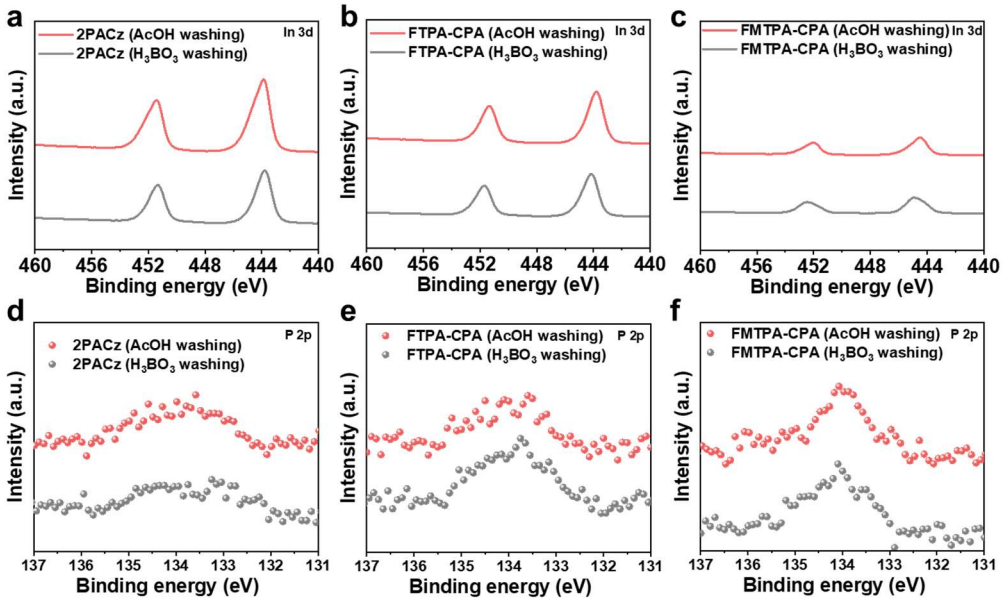

Fig. R15 (i.e., **Supplementary Fig. 16** in SI) XPS spectra of In 3d obtained from the (a) 2PACz, (b) FTPA-CPA and (c) FMTPA-CPA films after H_3BO_3 and ACOH washing; XPS spectra of P 2p obtained from the (d) 2PACz, (e) FTPA-CPA and (f)

FMTPA-CPA films after H_3BO_3 and AcOH washing.

Table R5 (i.e., **Supplementary Table 7** in SI**)** XPS spectra analysis obtained from the 2PACz, FTPA-CPA and FMTPA-CPA films.

SAM	SAMs	In area	P area	P/In
2PACz	fresh	343184.63	3809.36	0.0111
	EtOH washing	481605.70	3525.06	0.0073
	EtOH soaking	949840.88	5760.07	0.0061
	H_3BO_3 washing	745977.20	4105.93	0.0055
	AcOH washing	1124496.71	4625.02	0.0041
	aged (1 sun 85℃)	691893.62	4012.99	0.0058
FTPA-CPA	fresh	340987.59	5591.65	0.0164
	EtOH washing	372394.93	5245.49	0.0141
	EtOH soaking	338204.59	4531.30	0.0134
	H_3BO_3 washing	674946.00	6117.52	0.0091
	AcOH washing	798210.73	5438.88	0.0068
	aged (1 sun 85℃)	422132.45	4945.21	0.0117
FMTPA-CPA	fresh	212334.95	5482.02	0.0258
	EtOH washing	183058.07	4228.57	0.0231
	EtOH soaking	258752.68	5908.21	0.0228
	H_3BO_3 washing	237409.78	5515.63	0.0232
	AcOH washing	229678.72	5339.97	0.0233
	aged (1 sun 85℃)	279105.29	6284.57	0.0225

3. In the top-view SEM images, a significant amount of PbI2 is observed on the perovskite surface. While the presence of PbI2 can positively contribute to efficiency enhancement, it can be detrimental to long-term photostability. Specifically, PbI2 is highly susceptible to decomposition under light below 500 nm, raising concerns about its impact on the device's long-term reliability. The authors should provide SEM images before and after long-term stability to demonstrate the effect of PbI2 on long-term stability.

Response: Thanks for the reviewer's valuable suggestion. The scanning electron microscope (SEM) images provided in the original manuscript are that of the unpassivated perovskite films, just aiming to compare the morphology of perovskite films growth on different SAMs. **For the device stability test, we applied surface 1,3-**

Diaminopropane Dihydroiodide (PDADI) passivation, which eliminates the side effect of PbI_2 on long-term stability.

We agree with the reviewer that "*PbI_2 is highly susceptible to decomposition under light below 500 nm, raising concerns about its impact on the device's long-term reliability.*" Given that the three SAMs show negligible influence on the top-surface morphology, 2PACz was chosen as a representative molecule for analysis. In the top-view SEM images, residual PbI_2 can be clearly observed on the perovskite film surface. As shown in **Fig. R16**, for the pristine perovskite film without any post-treatment, the residual PbI_2 indeed susceptible to decomposition (more cracks appear and grain size reduction) under the ISOS-D-2 (85±5°C) and ISOS-L-2 (continuous-illumination including light below 500nm and 85±5°C) protocols.

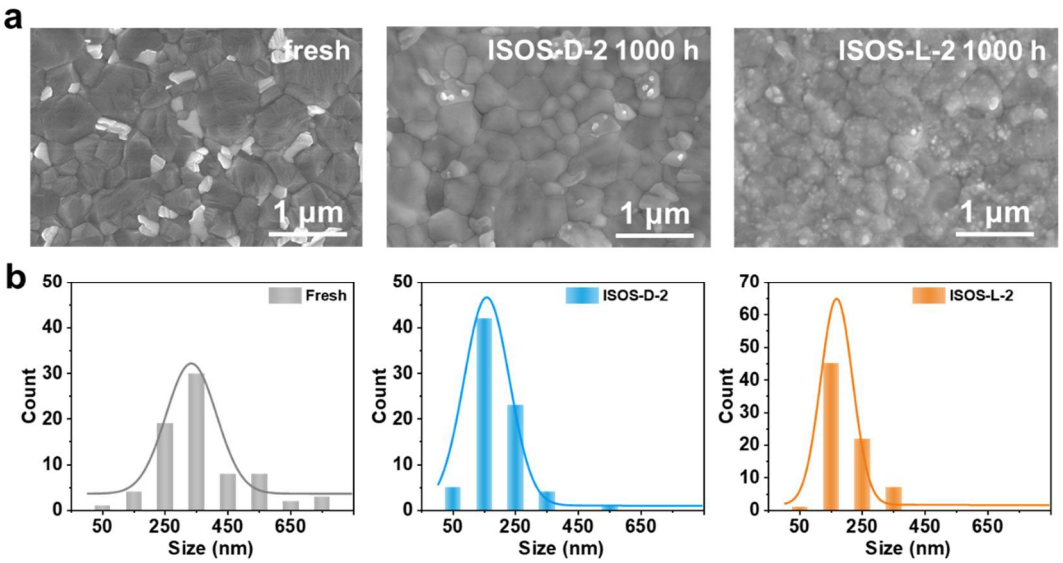

Fig. R16 (a) Top-view SEM images and (b) grain size distribution of perovskite films deposited on 2PACz before and after aging 1000 h under ISOS-D-2 and ISOS-L-2 protocols.

In our work, long-term stability measurements were conducted based on devices with structure of ITO/SAM/perovskite/PDADI/ fullerene (C_{60})/ atomic layer-deposited tin oxide (ALD-SnO_x)/Cu. **In the device, the perovskite top surface was passivated using the organic ammonium salt PDADI.** After PDADI treatment. As shown in **Fig. R17**, the amount of residual PbI_2 on the surface decreases, indicating the possibility of forming low-dimensional perovskites (*Adv. Mater.,* 2025, 37, 2411027). The Dion-Jacobson-phase quasi-2D perovskite generation are also confirmed by Grazing-Incidence Wide-Angle X-ray Scattering (GIWAXS) and photoluminescence (PL) and measurements (**Fig. R17a & Fig. R17b**), which revealed peaks at 0.70, 0.64, 0.45 Å in GIWAXS patterns and an emission peak at 695 nm in the photoluminescence (PL) spectra from the top surface side. The conversion of PbI_2 to low-dimensional perovskite capping layer can inhibit the decomposition of perovskite active layer, thereby mitigating device degradation. To further clarify this observation, we fabricated complete devices, which was aged 1000 h under the ISOS-D-2 and ISOS-L-2 protocols. After aging, the Cu electrodes and ALD-SnO_x were peeled off, and the C_{60} was

removed using chlorobenzene. The surface morphology of the perovskite films before and after aging 1000 h are shown in **Fig. R17c**. The perovskite films exhibited negligible morphology change, and the crystal size of aged samples remains similar to the fresh samples (**Fig. R17d**). In addition, the perovskite film based on FTPA-CPA and FMTPA-CPA also exhibited similar trends (**Fig. R18**), confirming the devices applying PDADI passivation exhibit long-term stability.

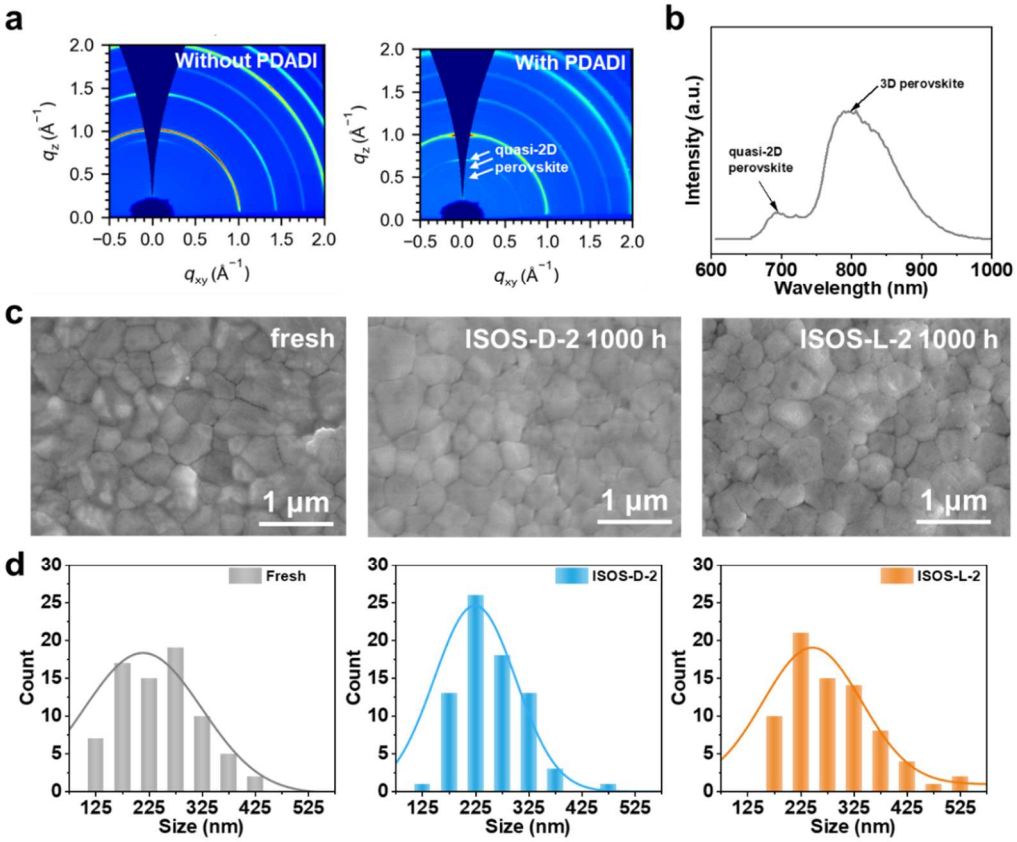

Fig. R17 (a) GIWAXS maps of perovskite films deposited on 2PACz without and with PDADI treatment; (b) PL of perovskite films deposited on 2PACz with PDADI treatment (from the top surface side); (c) Top-view SEM images, (d) grain size distribution, of perovskite films deposited on 2PACz before and after aging 1000 h under ISOS-D-2 and ISOS-L-2 protocols. Scale bar: 1 μm.

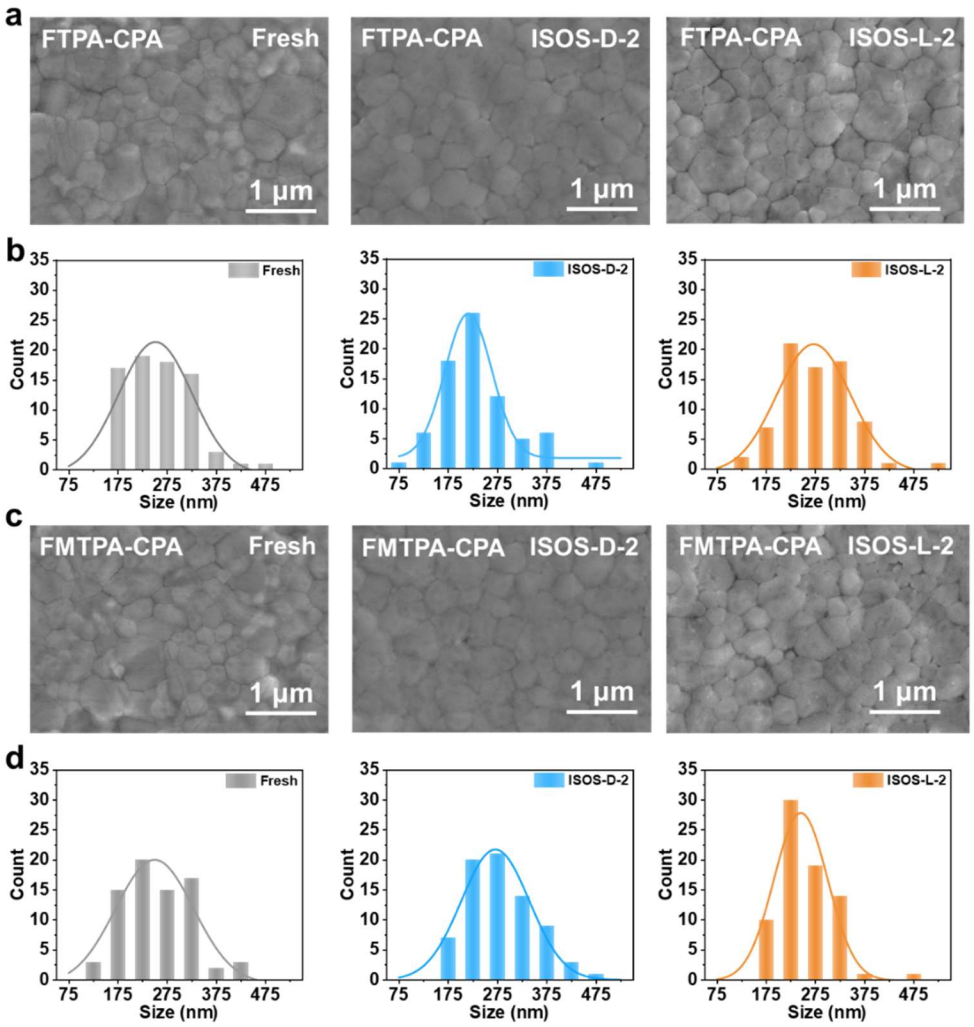

Fig. R18 (a) Top-view SEM images, (b) grain size distribution, of perovskite films deposited on FTPA-CPA before and after aging 1000 h under ISOS-D-2 and ISOS-L-2 protocols. (c) Top-view SEM images, (d) grain size distribution, of perovskite films deposited on FMTPA-CPA before and after aging 1000 h under ISOS-D-2 and ISOS-L-2 protocols. Scale bar: 1 μm.

4. It is essential to provide long-term stability data under a combined environment of UV-inclusive light and thermal stress. Providing this result should be presented as a key result to demonstrate practical durability.

Response: Thanks for the reviewer's valuable comments regarding the UV-inclusive light and thermal stress. We have followed the suggestions from the reviewer and the detailed results can be referred to the response to Comment 1 for Reviewer #2.

5. The current manuscript lacks logical justification for this strategy. Therefore, the introduction should be substantially revised to emphasize the significance of the proposed strategy and clearly differentiate it from a recent paper.

Response: Thanks for the reviewer's comments. **The recent published *Science* paper (10.1126/science. adz7969), from the mechanistic aspect, reveals the importance of covalent bond anchoring of SAMs on the ITO substrate is vital to the device**

stability. At the same time, numerous works on SAMs engineering developed a lot of effective strategies, like donor moiety engineering (*Science*, 389, 2025, 195; *Nature*, 2025, 646, 95), steric hindrance optimization (*Science*, 2024, 384, 1126), and multidentate coordination implement (*Science*, 2024, 383, 1236; *Adv. Mater.*, 2026, 38, e14735) etc., to construct more covalent bonding of SAMs through molecular aggregation suppression or binding sites increase. **However, in this work, we target to strengthen the covalent bonding energy between SAMs and ITO through a new concept using the molecular resonance design strategy** (especially for the design of electronic resonance that greatly affects the chemical property of the anchoring group) of SAMs. It could induce significant intramolecular redistribution of positive and negative charges (nearly 0.2 e). As a result, the phosphonic acid anchoring group bears more negative charge and is more capable of donating protons to form robust covalent bonds with the ITO substrate rather than hydrogen bonds. **Our approach provides a scientific principle as well as a broadly applicable molecular design strategy to intrinsically enhance the covalent bonding of SAMs anchored to ITO.** In this regard, our study can be facially superimposed with recent reported strategies. Importantly, the perovskite solar cells based on resonance design strategy achieved champion certified efficiency of 27.69% with excellent stability even under various protocols.

As suggested, we revised the introduction part to better emphasize the significance of the resonant structure design strategy and the relationship between this work and the recently published *Science* (10.1126/science. adz7969) paper (marked red).

Page 3 in the revised Manuscript:

…Despite the high efficiency, SAMs suffer from detachment issue during long-term real operation, The conjugated donor moiety has high tendency to aggregate,[13,14] and affects the anchoring bonding strength of the acceptor moiety, which severely restricts the robust SAMs anchoring.[15,16]

A recent report reveals that assisting the formation of covalent bonding between SAMs and indium tin oxide (ITO) substrate, other than hydrogen bonding or weak bonding aggregates, is vital to improve the device stability.[17] As a result, researchers developed donor moiety engineering,[18, 19] steric hindrance optimization,[20] and multidentate coordination implement,[21, 22] to construct more covalent bonding by either suppressing molecular aggregation or increasing binding sites.[23, 24] However, these strategies have negligible effect on the chemical property of the anchoring group. There lacks effective strategy targeting to intrinsically enhancing the covalent bonding strength, *i.e.*, increasing the binding energy of the P-O-In bond, which limits the device stability under even more harsh operating conditions.[17]

As the SAMs anchoring bond formation is essentially an acid-base condensation with dehydration, enhancing the negative charge density of the coordinating atom serves as the most direct and fundamental strategy to increase acidity and thus strengthening covalent anchoring bond.[25] Although anchoring groups possess fixed chemical structures that are difficult to modify directly, the D-A nature of the SAM benefits from substituent design, providing an important avenue for modifying the anchoring strength. Rational electronic resonance structure serves as a core strategy for enhancing intramolecular charge redistribution.[26] …

6. The C-AFM images (Fig. 3c) are currently missing scale bars. Authors should add the scale bars.

Response: Thanks for the reviewer's careful suggestion. **The scale bars in conductive atomic force microscopy (C-AFM) images have been added (Fig. 3f,** original **Fig. 3c).**

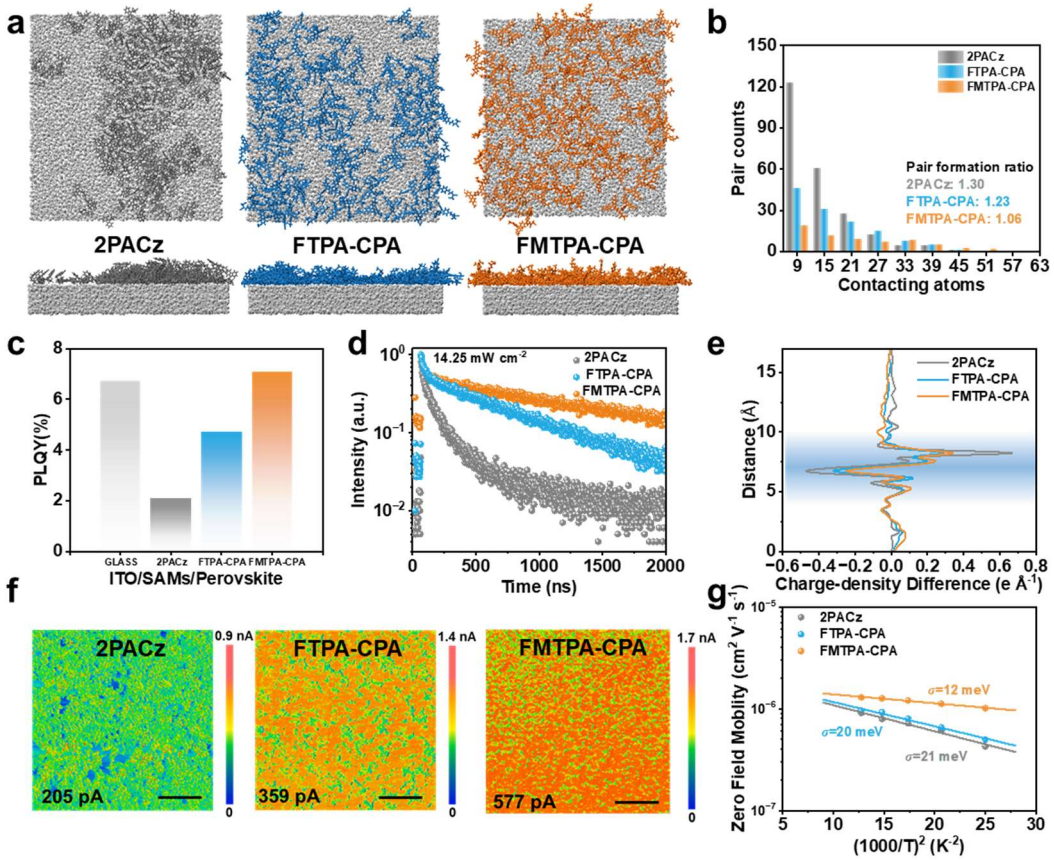

Fig. 3| Compact, homogeneous D-A-D resonant SAM and resulting high quality perovskite film. a, Top views and side views of equilibrated molecular representations of 2PACz, FTPA-CPA and FMTPA-CPA systems in MD simulations. **b,** MD simulated equilibrated snapshots and counts of dimer clusters for 2PACz, FTPA-CPA and FMTPA-CPA. **c,** PLQY of perovskite films on 2PACz, FTPA-CPA and FMTPA-CPA SAMs. **d,** Photoluminescence decays of perovskite films on 2PACz, FTPA-CPA and FMTPA-CPA SAMs. **e,** Calculated charge-density difference along the vertical direction to the ITO surface. **f,** C-AFM images of the 2PACz, FTPA-CPA and FMTPA-CPA (the scale bars represent 1 μm). **g,** Hole mobilities of the 2PACz, FTPA-CPA and FMTPA-CPA films as a function of $1/T^2$ were obtained using the equation for GDM.

7. To ensure the reproducibility of the reported 27.45% efficiency and long-term stability data, the exact number of independent cells used for each statistical analysis must be clearly stated.

Response: Thanks for the reviewer's suggestion. We previously have already provided the statistical analysis of PCEs in **Table R2** (i.e., **Supplementary Table 11** in SI). Now we added the detailed PCE values and exact cell numbers for statistical analysis of PCE

and stability.

We used **20 independent cells** to evaluate reproducibility of champion photovoltaic performance. The PCE distribution and standard deviations are detailed in **Table R2** (i.e., **Supplementary Table 11** in SI) and the corresponding statistical data of reported champion efficiency have been added in the revised Supplementary Information (**Table R6**). The champion device exhibits an average of 27.39% with a standard deviation of 0.06, which is nearly identical to 27.45%. During the period of revision, with further optimizations on the perovskite crystallization, we improve the champion efficiency to 27.69%, with the updated efficiency statistics summarized in the **Table R7** (i.e., **Supplementary Table 14** in SI) & **Table R2** (i.e., **Supplementary Table 11** in SI) & **Fig. R19** (i.e., **Supplementary Fig. 56** in SI). The champion device exhibits an average of 27.62% with a standard deviation of 0.07, which is nearly identical to 27.69%.

Table R2 (i.e., **Supplementary Table 11** in SI) Photovoltaic parameters of pero-SCs under AM1.5G, 100 mW/cm^2 illumination. Forward scan: –0.2 V→1.2 V (small-area), –0.5 V→9.5 V (large-area); Reverse scan: 1.2 V→–0.2 V (small-area), 9.5 V→–0.5 V (large-area).

Substrate type	SAMs	Scan direction	V_{oc} (V)	J_{sc} (mA/cm^2)	FF (%)	PCE$_{max}$[a](PCE$_{avg}$)[a] (%)
Glass/ITO (0.063 cm^2)	2PACz	Reverse	1.18 (1.17±0.02)	26.46 (26.50±0.15)	81.9 (81.9±1.8)	25.57 (25.30±0.20)
		Forward	1.18 (1.16±0.02)	26.47 (26.48±0.13)	79.3 (79.0±1.7)	24.77 (24.35±0.30)
	FTPA-CPA	Reverse	1.19 (1.20±0.02)	26.44 (26.53±0.12)	83.9 (82.6±1.4)	26.40 (26.21±0.14)
		Forward	1.19 (1.19±0.01)	26.57 (26.49±0.13)	79.5 (79.2±1.1)	25.14 (24.91±0.19)
	FMTPA-CPA	Reverse	1.20 (1.20±0.01)	26.59 (26.52±0.10)	86.6 (86.5±0.2)	27.69 (27.62±0.07)
		Forward	1.20 (1.20±0.01)	26.75 (26.65±0.11)	83.3 (82.9±0.5)	26.81 (26.65±0.09)
Glass/ITO (15.64 cm^2)	2PACz	Reverse	8.58 (8.46±0.19)	3.11 (3.10±0.02)	69.3 (69.3±1.0)	18.49 (18.17±0.22)
		Forward	8.37 (8.28±0.15)	3.10 (3.10±0.01)	68.5 (68.0±1.3)	17.77 (17.46±0.21)
	FTPA-CPA	Reverse	8.88 (8.83±0.09)	3.19 (3.18±0.01)	77.0 (76.8±1.0)	21.81 (21.54±0.19)
		Forward	8.87 (8.79±0.09)	3.20 (3.20±0.02)	74.5 (74.3±0.8)	21.15 (20.92±0.16)
	FMTPA-CPA	Reverse	9.00 (9.01±0.08)	3.25 (3.24±0.02)	80.8 (80.6±0.8)	23.63 (23.48±0.08)
		Forward	8.96 (8.94±0.09)	3.24 (3.23±0.02)	79.1 (78.9±0.8)	22.96 (22.80±0.06)
PET/ITO (0.063 cm^2)	2PACz	Reverse	1.17 (1.17±0.02)	25.62 (25.64±0.07)	81.2 (80.3±0.9)	24.35 (23.88±0.22)
		Forward	1.17 (1.16±0.01)	25.04 (25.18±0.07)	79.7 (78.6±0.9)	23.35 (22.95±0.19)

	FTPA-CPA	Reverse	1.19 (1.19±0.01)	25.81 (25.85±0.05)	83.3 (81.9±0.7)	25.58 (25.09±0.20)
		Forward	1.18 (1.17±0.01)	25.88 (25.88±0.08)	80.0 (79.8±0.5)	24.42 (24.25±0.10)
	FMTPA-CPA	Reverse	1.21 (1.20±0.01)	26.17 (26.19±0.09)	84.4 (84.2±0.9)	26.64 (26.45±0.13)
		Forward	1.21 (1.20±0.01)	25.88 (26.04±0.08)	83.9 (83.5±0.7)	26.21 (26.03±0.11)
PET/ITO (15.64 cm^2)	2PACz	Reverse	8.46 (8.23±0.10)	3.11 (3.12±0.01)	64.8 (64.0±0.5)	17.06 (16.48±0.16)
		Forward	8.30 (8.02±0.12)	3.07 (3.10±0.01)	61.4 (61.1±0.5)	15.63 (15.22±0.14)
	FTPA-CPA	Reverse	8.98 (8.78±0.09)	3.14 (3.13±0.01)	74.7 (75.0±0.6)	21.07 (20.64±0.14)
		Forward	8.80 (8.65±0.11)	3.13 (3.13±0.01)	72.9 (72.8±0.8)	20.08 (19.69±0.13)
	FMTPA-CPA	Reverse	9.07 (9.08±0.06)	3.14 (3.14±0.01)	77.9 (77.5±0.5)	22.18 (22.12±0.06)
		Forward	9.07 (9.05±0.07)	3.14 (3.14±0.01)	75.4 (75.3±0.5)	21.46 (21.41±0.05)

[a] The maximum PCE, average PCE, and standard deviations of 20 devices

Table R6 Photovoltaic parameters of 20 independent pero-SCs based on FMTPA-CPA under AM1.5G, 100 mW/cm^2 illumination. Forward scan: –0.2 V→1.2 V; Reverse scan: 1.2 V→–0.2 V.

	V_{oc} (V)	J_{sc} (mA/cm^2)	FF (%)	PCE_{max}[a](PCE_{avg})[a] (%)
1#	1.21	26.68	85.03	27.45
2#	1.20	26.79	84.92	27.30
3#	1.21	26.64	85.06	27.42
4#	1.22	26.48	84.78	27.39
5#	1.22	26.56	84.50	27.38
6#	1.21	26.78	84.62	27.42
7#	1.21	26.75	84.56	27.37
8#	1.20	26.85	85.07	27.41
9#	1.21	26.71	84.87	27.43
10#	1.21	26.68	85.00	27.44
11#	1.21	26.69	84.84	27.40
12#	1.22	26.56	84.50	27.38
13#	1.20	26.71	85.27	27.33
14#	1.20	26.63	85.62	27.36
15#	1.21	26.71	84.81	27.41

16#	1.22	26.58	84.65	27.45
17#	1.21	26.51	85.23	27.34
18#	1.20	26.83	85.41	27.50
19#	1.20	26.59	85.84	27.39
20#	1.21	26.51	84.86	27.22
	1.21±0.01	26.66±0.11	85.0±0.06	27.39±0.06

Table R7 (i.e., **Supplementary Table 14** in SI) Photovoltaic parameters of 20 independent pero-SCs based on FMTPA-CPA under AM1.5G, 100 mW/cm^2 illumination. Forward scan: –0.2 V→1.2 V; Reverse scan: 1.2 V→–0.2 V.

	V_{oc} (V)	J_{sc} (mA/cm^2)	FF (%)	PCE_{max}[a](PCE_{avg})[a] (%)
1#	1.20	26.59	86.64	27.69
2#	1.20	26.61	86.33	27.57
3#	1.20	26.58	86.34	27.54
4#	1.21	26.35	86.62	27.62
5#	1.21	26.37	86.52	27.61
6#	1.20	26.52	86.23	27.44
7#	1.20	26.61	86.61	27.66
8#	1.20	26.54	86.59	27.58
9#	1.20	26.59	86.62	27.64
10#	1.21	26.47	86.18	27.60
11#	1.20	26.58	86.60	27.62
12#	1.21	26.47	86.59	27.73
13#	1.20	26.55	86.57	27.58
14#	1.21	26.54	86.58	27.80
15#	1.21	26.35	86.59	27.61
16#	1.20	26.56	86.60	27.60
17#	1.21	26.37	86.51	27.60
18#	1.20	26.63	86.57	27.66
19#	1.20	26.63	86.58	27.67
20#	1.21	26.43	86.29	27.60
	1.20±0.01	26.52±0.10	86.5±0.15	27.62±0.07

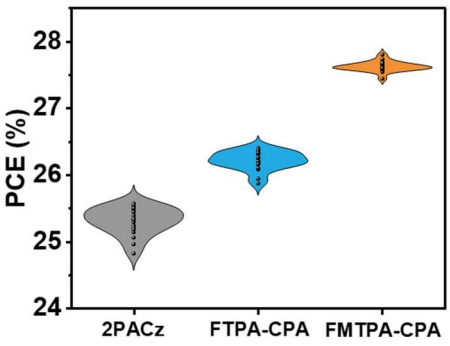

Fig. R19 (i.e., **Supplementary Fig. 56** in SI) The statistics of PCE values obtained from *J-V* characteristic for devices based on 2PACz, FTPA-CPA and FMTPA-CPA SAMs (20 devices).

The stability of the devices under ISOS-D-2, ISOS-T-3, ISOS-D-3 and UV light illumination stability was evaluated using **10 independent cells.** The stabilities under ISOS-L-2, ISOS-LC-1 and MPPT under LEP, MH lamp illumination were initially evaluated using one independent cell. To get a more reliable stability assessment of the devices under thermal heating, thermal cycling and UV light illumination, the stability measurements according to ISOS-L-2, ISOS-LC-1 protocols and MPPT tracking under LEP, MH lamp illumination was re-evaluated, with identical measurements performed on 10 independent cells (**Fig. R20** (i.e., **Supplementary Fig. 64** in SI). These results are consistent with the previously measured stability of one independent cell, confirming the enhanced stability of devices based on FMTPA-CPA under varied protocols.

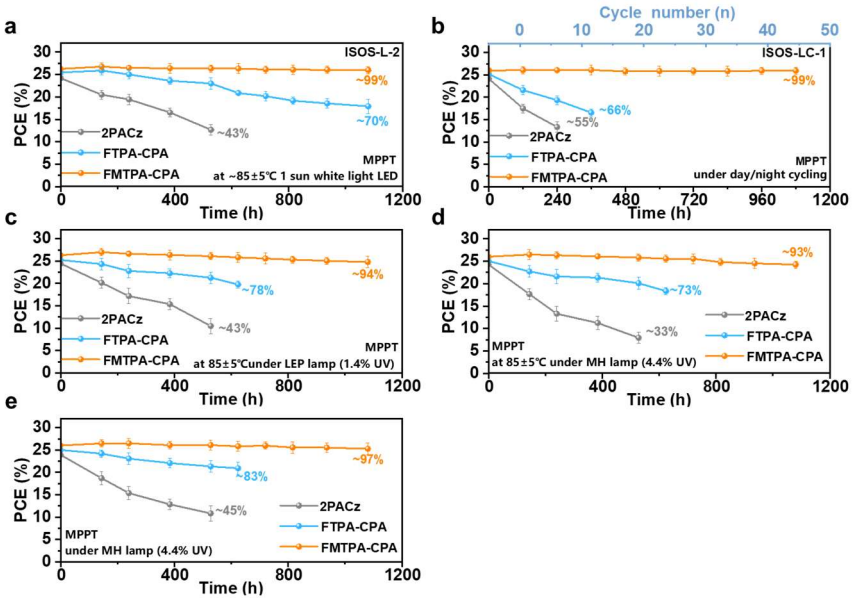

Fig. R20 (i.e., **Supplementary Fig. 64** in SI) (a) Light-soaking stability of small-area devices (MPPT conditions, 85±5°C) under ISOS-L-2 protocol; (b) Light-soaking stability of small-area devices (MPPT conditions under day/night cycling) under ISOS-LC-1; (c) Light-soaking stability of small-are devices (MPPT conditions under LEP

lamp, 85±5°C); (d) Light-soaking stability of small-are devices (MPPT conditions under MH lamp, 85±5°C); (e) Light-soaking stability of small-are devices (MPPT conditions under MH lamp).

We added the number of independent cells used for stability statistical analysis in the revised manuscript (marked red):

Page 11 in the revised Manuscript: The robust anchoring of FMTPA-CPA encouraged us to evaluate the stability of pero-SCs devices under varied aging protocols. The FMTPA-CPA-based devices retained approximately 95% of the initial efficiency after 3,000 h of 85±5°C thermal stress (according to ISOS-D-2, 10 devices), which is much superior to that of the 2PACz- and FTPA-CPA-based device (**Fig. 4d**).

Page 12 in the revised Manuscript: The PCE of the 2PACz-based and FTPA-CPA-based device rapidly declined during aging with about 720 thermal cycles (from –40°C to 85 °C following ISOS-T-3, 10 devices, **Fig. 4g**). However, the stable FMTPA-CPA anchoring enabled the device to maintain 97% of its initial PCE even after enduring 720 rigorous thermal cycles (2,000 h).

Response to Reviewer #3:

This manuscript presents an impressive advance in the field of perovskite solar cells by introducing an electronic-resonance enhanced self-assembled monolayer (SAM) of FMTPA-CPA. The core concept of using a symmetric D-A-D-like resonant molecular structure to intrinsically enhance the negative charge density at the phosphonic acid anchoring site is innovative and significant. The reported results are outstanding, with a certified PCE of 27.45% for rigid small-area devices, 26.64% for flexible devices, and 23.63% for a mini-module. The operational stability results under various conditions (99% PCE retention after 1080 h MPPT at 85°C, 97% after 1000 h day/night cycling, 98% after 720 thermal cycles) are state-of-the-art and address a critical bottleneck for commercialization. The work is undoubtedly suitable for a high-impact journal. However, to establish the proposed mechanisms and validate the extraordinary claims, substantial revisions and clarifications are required. Several key aspects of the experimental evidence, data interpretation, and mechanistic depth are currently insufficient or give rise to questions. The manuscript should be reconsidered after revisions addressing the following points.

Response: Thanks for the reviewer's positive evaluation of our work that "*The operational stability results under various conditions are state-of-the-art and address a critical bottleneck for commercialization.*" and valuable suggestions, based on which we have further improved the quality of our work. We have responded to the concerns point-to-point as follows.

1. The authors attribute the stability to robust monolayer anchoring. However, the evidence for a complete, uniform monolayer of different molecules on ITO, both initially and after aging, is indirect. It is possible that the initial coverage includes multilayers or aggregates, and the observed stability during aging might simply reflect the desorption of only weakly bound excess molecules, not the anchored monolayer itself. The authors should provide more direct and conclusive evidence.

Response: Thanks for the reviewer's insightful comments. With more systematic investigations, we find after EtOH washing, the initial coverage of 2PACz and FTPA-CPA may include a tiny amount of multilayers or aggregates, but the D-A-D resonant FMTPA-CPA tends to form a robust and stable covalently anchored monolayer. The covalently bonded monolayer is the critical factor determining the stability of devices. Here are the details of these systematic post-treatment and characterization results.

The electron-resonant FMTPA-CPA forms robust and stable covalently anchored monolayer. During the device fabrication process, EtOH washing can minimize the formation of multilayer structures or molecular aggregates. EtOH soaking, and AcOH washing can be further used to remove weakly bound aggregates or multilayers. As shown in **Fig. R21 & Table R8** (i.e., **Supplementary Table 7** in SI) **& Fig. R25** (i.e., **Supplementary Fig. 17** in SI), the high P/In (0.023) of FMTPA-CPA has negligible change, whereas those of 2PACz (from 0.011 to 0.007, 0.006 and 0.004) and FTPA-CPA (from 0.016 to 0.014, 0.013 and 0.007) significantly decreased after EtOH washing, EtOH soaking and AcOH washing post-treatments, respectively. This

indicates that FMTPA-CPA majorly forms the stable covalent anchored monolayer, while 2PACz and FTPA-CPA samples initially contain a tiny amount of multilayer or aggregated molecules.

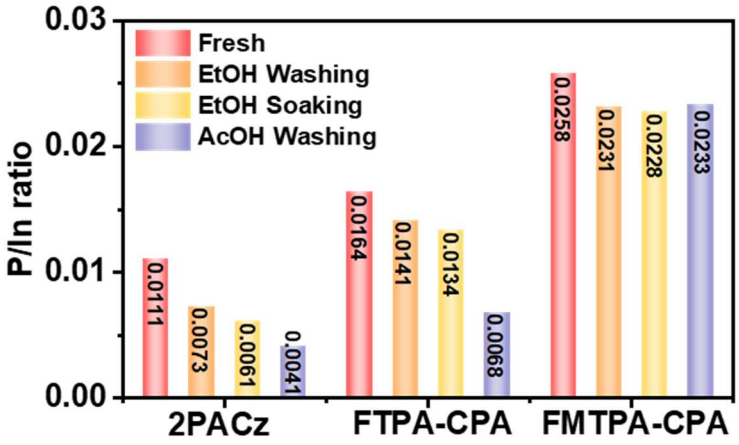

Fig. R21 The P/In ratio by XPS spectroscopy of 2PACz, FTPA-CPA and FMTPA-CPA on ITO substrate without any post-treatment, with EtOH washing, EtOH soaking and AcOH washing post-treatments.

We fabricated complete devices using SAMs with different post-treatments (without washing, with ethanol washing and with ethanol soaking). The devices based on 2PACz, FTPA-CPA, and FMTPA-CPA exhibited nearly identical photovoltaic performance (**Fig. R22 & Table R9**), **confirming that the desorption of weakly bound excess molecules has negligible impact on device PCE**.

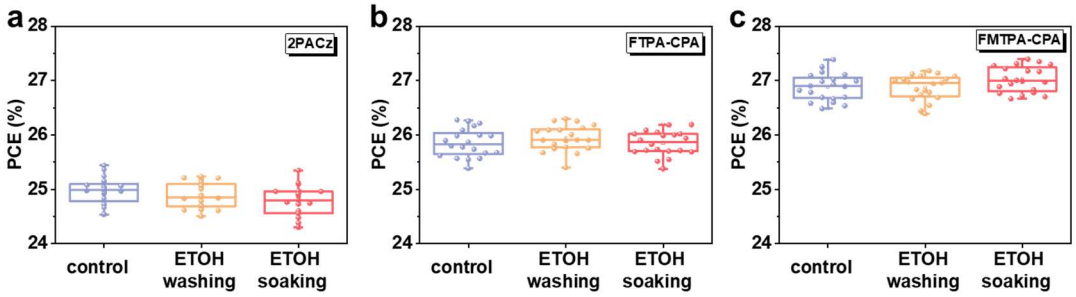

Fig. R22 The statistics PCE values obtained from *J-V* characteristic for devices based on (a) 2PACz, (b) FTPA-CPA and (c) FMTPA-CPA without any post-treatment, with ethanol washing, and with ethanol soaking post-treatment.

Furthermore, we investigated the effect of the P-O-In covalent bonding on device stability. The XPS O 1s orbital spectrum had four fitting peaks at 533.6, 532.4, 530.9, and 529.7 eV, representing P-O-In, In-O-H, surface oxygen vacancies (V_O), and In/Sn-O, respectively. We can extract the quantity of P-O-In covalent anchoring bonding through peak deconvolution on the XPS O 1s spectra (**Fig. R23**). After AcOH washing, the amount of P-O-In covalent bonding decreased by 55% and 24% for 2PACz and FTPA-CPA, but remained nearly unchanged for FMTPA-CPA, showing that the AcOH washing partially breaks the P-O-In covalent bond for 2PACz and FTPA-CPA, while it has little effect on P-O-In covalent bond for FMTPA-CPA. In line with the device

performance (**Fig. R24 & Table R9**), only 2PACz and FTPA-CPA samples show photovoltaic performance loss, while the PCE of FMTPA-CPA sample show no obvious decay after AcOH washing. **These results indicate that device PCE decay during operation arises mainly from cleavage of P-O-In covalent bonds, not from desorption of weakly bound excess molecules.** Therefore, we ascribe the enhanced stability to the robust monolayer anchoring of FMTPA-CPA.

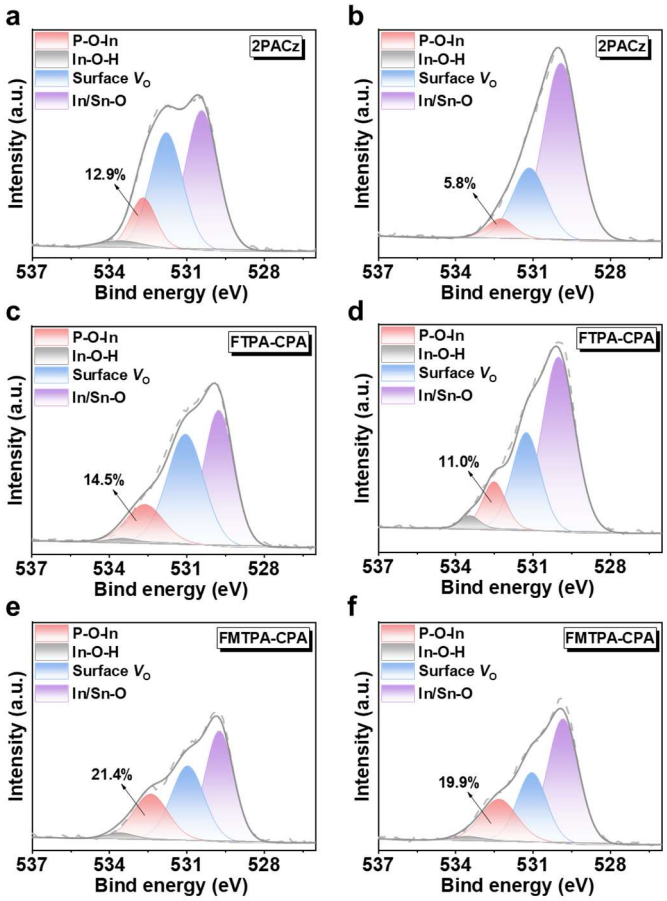

Fig. R23 XPS spectra of O 1s obtained from the 2PACz (a) before and (b) after AcOH washing; XPS spectra of O 1s obtained from the FTPA-CPA (c) before and (d) after AcOH washing; XPS spectra of O 1s obtained from the FMTPA-CPA (e) before and (f) after AcOH washing.

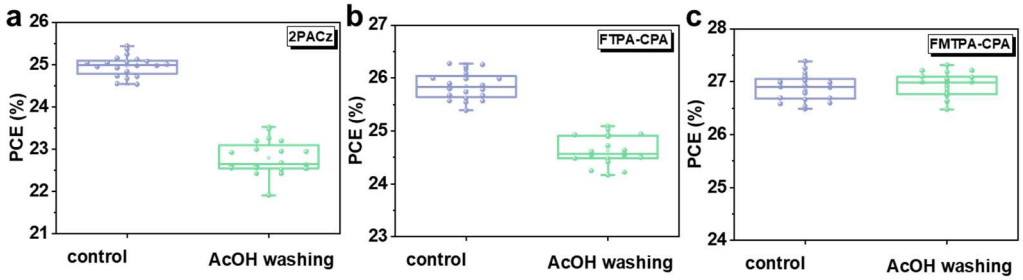

Fig. R24 The statistics PCE values obtained from *J-V* characteristic for devices based on (a) 2PACz, (b) FTPA-CPA and (c) FMTPA-CPA without any post-treatment and with AcOH washing.

We have revised the corresponding description in the revised manuscript and revised Supplementary Information (marked red):

Pages 12~13 in the revised Manuscript: Considering the potential extreme harsh working environments, the FMTPA-CPA-based devices maintained 98% of their initial PCEs over 1080 h under damp heat (85±5%RH & 85±5°C) aging, whereas the devices with FTPA-CPA and 2PACz SAMs retained only 76% and 53% of their initial PCEs respectively, within the same aging time (**Supplementary Fig. 63**). The enhanced stability originates from the robust monolayer covalent anchoring of FMTPA-CPA, avoiding protonation activated hydrolysis of anchoring group under multiple stability protocol (**Supplementary Figs. 64-67 & Tables 17-18 & Supplementary Note 7 & Note 11**).

Page 15 in the revised Supplementary Information:

Supplementary Note 7 The initial aggregate of 2PACz, FTPA-CPA and FMTPA-CPA

The initial coverage of 2PACz and FTPA-CPA may include multilayers or aggregates, but the resonant FMTPA-CPA tends to form a robust and stable covalently anchored monolayer after EtOH washing. The covalently bonded monolayer is the critical factor determining the stability of devices. During the device fabrication process, EtOH washing was applied to minimize the formation of multilayer structures or molecular aggregates. Ethanol soaking, and AcOH washing were further applied to remove weakly bound aggregates. As shown in **Supplementary Fig. 17 & Table 7**, the high P/In (0.023) of FMTPA-CPA has negligible change, whereas those of 2PACz (from 0.011 to 0.007, 0.006 and 0.004) and FTPA-CPA (from 0.016 to 0.014, 0.013 and 0.007) significantly decreased. This indicates that FMTPA-CPA majorly forms the stable covalent anchored monolayer after EtOH washing, while 2PACz and FTPA-CPA samples initially contain a tiny amount of multilayer or aggregated molecules.

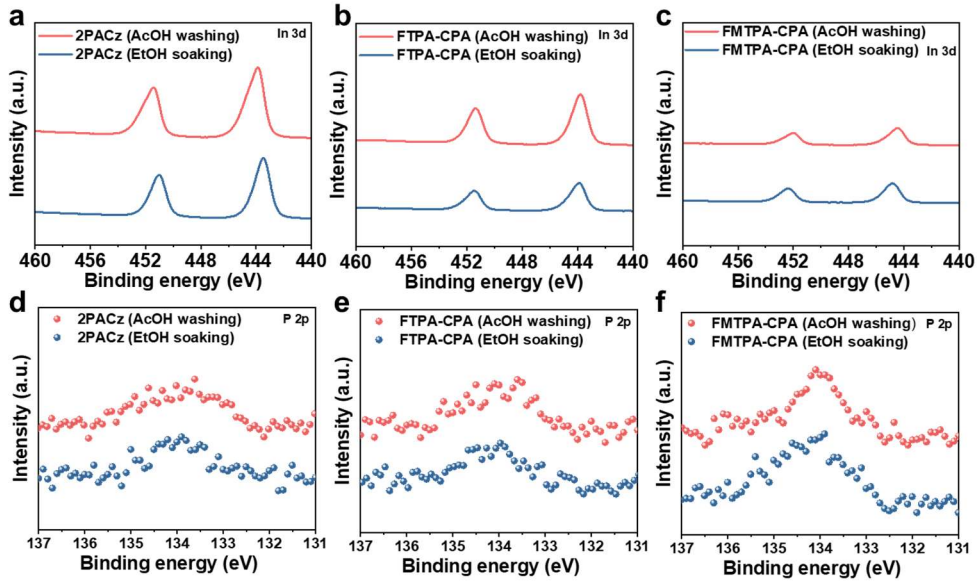

Fig. R25 (i.e., **Supplementary Fig. 17** in SI) XPS spectra of In 3d obtained from the (a) 2PACz, (b) FTPA-CPA and (c) FMTPA-CPA films after EtOH soaking and AcOH washing; XPS spectra of P 2p obtained from the (d) 2PACz, (e) FTPA-CPA and (f)

FMTPA-CPA films after EtOH soaking and AcOH washing.

Table R8 (i.e., **Supplementary Table 7** in SI) XPS spectra analysis obtained from the 2PACz, FTPA-CPA and FMTPA-CPA films.

SAM	SAMs	In area	P area	P/In
2PACz	fresh	343184.63	3809.36	0.0111
	EtOH washing	481605.70	3525.06	0.0073
	EtOH soaking	949840.88	5760.07	0.0061
	H_3BO_3 washing	745977.20	4105.93	0.0055
	AcOH washing	1124496.71	4625.02	0.0041
	aged (1 sun 85°C)	691893.62	4012.99	0.0058
FTPA-CPA	fresh	340987.59	5591.65	0.0164
	EtOH washing	372394.93	5245.49	0.0141
	EtOH soaking	338204.59	4531.30	0.0134
	H_3BO_3 washing	674946.00	6117.52	0.0091
	AcOH washing	798210.73	5438.88	0.0068
	aged (1 sun 85°C)	422132.45	4945.21	0.0117
FMTPA-CPA	fresh	212334.95	5482.02	0.0258
	EtOH washing	183058.07	4228.57	0.0231
	EtOH soaking	258752.68	5908.21	0.0228
	H_3BO_3 washing	237409.78	5515.63	0.0232
	AcOH washing	229678.72	5339.97	0.0233
	aged (1 sun 85°C)	279105.29	6284.57	0.0225

Table R9 Photovoltaic parameters of pero-SCs with and without post-treatment under AM1.5G, 100 mW/cm^2 illumination. Forward scan: −0.2 V→1.2 V; Reverse scan: 1.2 V→−0.2 V.

SAMs	post-treatment	V_{oc} (V)	J_{sc} (mA/cm^2)	FF (%)	PCE_{max}[a](PCE_{avg})[a] (%)
2PACz	--	1.18 (1.17±0.01)	26.41 (26.23±0.12)	81.0 (81.5±0.50)	25.24 (24.97±0.25)
	EtOH washing	1.18 (1.17±0.01)	26.40 (26.19±0.10)	81.0 (81.0±0.50)	25.23 (24.88±0.23)

	EtOH soaking	1.18 (1.17±0.01)	26.18 (26.19±0.09)	81.3 (80.8±0.49)	25.12 (24.78±0.29)
	AcOH washing	1.17 (1.14±0.01)	26.04 (26.05±0.06)	77.2 (76.45±0.96)	23.52 (22.79±0.40)
FTPA-CPA	--	1.19 (1.18±0.01)	26.42 (26.28±0.15)	83.5 (83.2±0.47)	26.25 (25.85±0.26)
	EtOH washing	1.19 (1.18±0.01)	26.43 (26.29±0.10)	83.6 (83.4±0.47)	26.29 (25.94±0.24)
	EtOH soaking	1.19 (1.18±0.01)	26.45 (26.23±0.11)	83.2 (83.4±0.28)	26.19 (25.84±0.23)
	AcOH washing	1.18 (1.16±0.01)	26.25 (26.18±0.12)	81.0 (81.2±0.62)	25.09 (24.62±0.27)
FMTPA-CPA	--	1.21 (1.20±0.01)	26.69 (26.46±0.18)	84.8 (84.6±0.44)	27.39 (26.93±0.26)
	EtOH washing	1.21 (1.20±0.01)	26.58 (26.40±0.13)	84.5 (84.7±0.42)	27.18 (26.92±0.24)
	EtOH soaking	1.21 (1.20±0.01)	26.57 (26.49±0.10)	85.2 (84.7±0.41)	27.39 (27.02±0.23)
	AcOH washing	1.21 (1.20±0.01)	26.59 (26.50±0.10)	84.9 (84.6±0.32)	27.32 (26.93±0.22)

[a] The maximum PCE, average PCE, and standard deviations of 20 devices.

2. The manuscript compellingly argues that resonance enhances charge density at the anchor. However, a critical question remains: how much stronger is the anchoring due to resonance compared to other established strategies for improving SAM anchoring stability? Recent works (Science 2024, 383, 1236; Adv. Mater. 2025, adma.202514735; Nature 2025, 646, 95) have also achieved improved stability. The authors should calculate and compare the intrinsic P-O-In binding energies and, if possible, experimentally measure the desorption activation energies for their resonant SAM versus representative molecules from these other strategic classes. This is essential to contextualize the novelty and superiority of the resonance approach within the rapidly evolving field of stable SAMs.

Response: Thanks for the reviewer' comments. The D-A-D electronic resonance approach proposed in this work provides a simple molecular-level design strategy of SAM to intrinsically increase the anchoring bond strength, which is different to the previously reported strategies to increase covalent binding sites and inhibit aggregation. In addition, our approach can be superimposed with those reported strategies to further enhance device stability.

We first view through the key points in "*Recent works (Science 2024, 383, 1236; Adv. Mater. 2025, adma.202514735; Nature 2025, 646, 95)*."

1. For the *Science* paper, it introduces atomic-layer deposition to create an indium tin oxide substrate with a fully covalent hydroxyl-covered surface for SAM anchoring, thus ensuring SAM is anchored on substrates by covalent bonding, rather than hydrogen bonded. The major cause for improved stability is increased covalent binding sites.
2. Similarly, for the *Nature* paper, it employs a cross-linkable co-SAM to enhance the conformational stability of hole-selective SAMs against external stresses. Through crosslinking, the SAMs have two phosphonic acid anchoring sites, which minimizes substrate surface exposure caused by wiggling of loose SAMs. This strategy improves stability also by increased covalent binding sites.
3. For the *Adv. Mater.* paper, it uses an additive, sulfadiazine (SDZ) molecules, to deprotonate phosphonic acid groups in SAMs, generating phosphate anions that strengthen electrostatic interactions with the positively charged transparent conductive oxide (TCO) substrates. The key point is also assisting the SAMs covalent anchoring with TCO substrates.

The three previously reported strategies have demonstrated to be reliable and effective to assist the formation of covalent anchoring. However, all of them has negligible effect on the chemical property of the anchoring group after P-O-In bond formation, and thus the intrinsic covalent P-O-In bonding energy between SAMs and ITO is not affected. Here, the molecular electronic resonance approach proposed in this work provides a novel molecular-level design route of SAMs chemical structure that not only targets to intrinsically increasing covalent bonding strength of SAMs on ITO, but also can be facially superimposed with those strategies to further enhance anchoring strength.

We have revised introduction to more clearly highlight the resonance strategy discussed in the revised manuscript (marked red):

Page 3 in the revised Manuscript: A recent report reveals that assisting the formation of covalent bonding between SAMs and indium tin oxide (ITO) substrate, other than hydrogen bonding or weak bonding aggregates, is vital to improve the device stability.[17] As a result, researchers developed donor moiety engineering,[18, 19] steric hindrance optimization,[20] and multidentate coordination implement,[21, 22] to construct more covalent bonding by either suppressing molecular aggregation or increasing binding sites.[23, 24] However, these strategies have negligible effect on the chemical property of the anchoring group. There lacks effective strategy targeting to intrinsically enhancing the covalent bonding strength, *i.e.,* increasing the binding energy of the P-O-In bond, which limits the device stability under even more harsh operating conditions.[17]

In response to the comment that "*The authors should calculate and compare the intrinsic P-O-In binding energies*", three representative molecules were designed to investigate the corresponding bonding mechanism. As shown in **Fig. R26**, methylphosphonic acid (MPA) and (1-cyanovinyl)phosphonic acid (CPA) were designed to represent the intrinsic P-O-In covalent bonding by excluding donor group effect, whereas the (E)-(4,4-bis(4-(bis(3-fluoro-4-methoxyphenyl)amino)phenyl)-1-

cyanobut-1-en-1-yl)phosphonic acid (FMTPA-DCPA) was designed to suppress D-A-D electronic resonance by removing the conjugated C=C double bond.

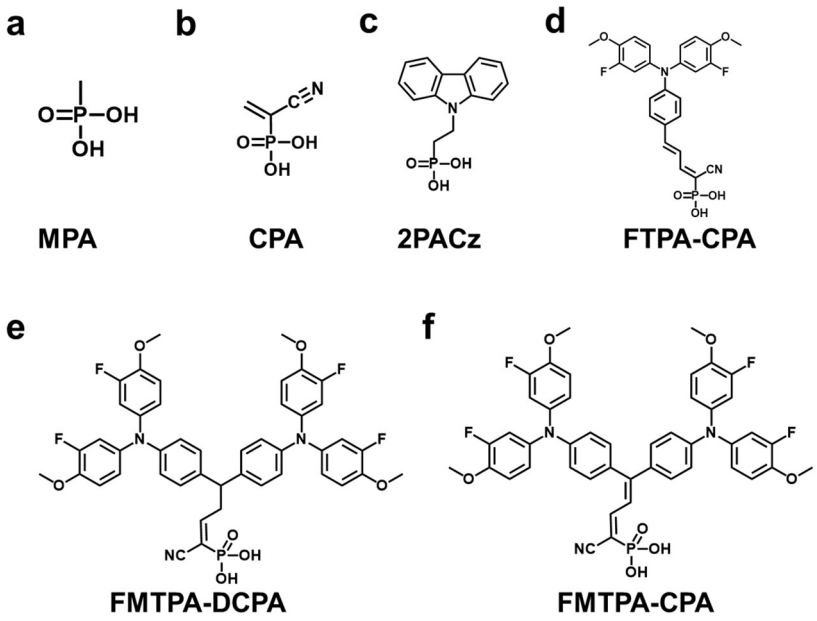

Fig. R26 Molecule structure of (a) MPA, (b) CPA, (c) 2PACz, (d) FTPA-CPA, (e) FMTPA-DCPA and (f) FMTPA-DCPA.

DFT calculations indicate that the MPA and CPA exhibit smaller steric hindrance and therefore covalent bond more readily to the ITO surface forming intrinsic P-O-In covalent bonding in **Fig. R27**. The P-O-In anchoring binding energies (-2.12 eV for MPA and -2.02 eV for CPA) are stronger than that of commonly SAMs 2PACz (-1.65 eV) and comparable to FTPA-CPA (-2.06 eV). As for the electronic-resonance FMTPA-CPA, it shows an obviously higher binding energy of -2.31 eV. While once removing the C=C double bond in FMTPA-DCPA disrupts the electronic resonance, leading to a lower binding energy (-1.94 eV). These results demonstrate that the D-A-D electronic resonance in FMTPA-CPA enhances P-O-In binding strength, increasing intrinsic binding energy by approximately 0.4 eV relative to non-resonant analogs.

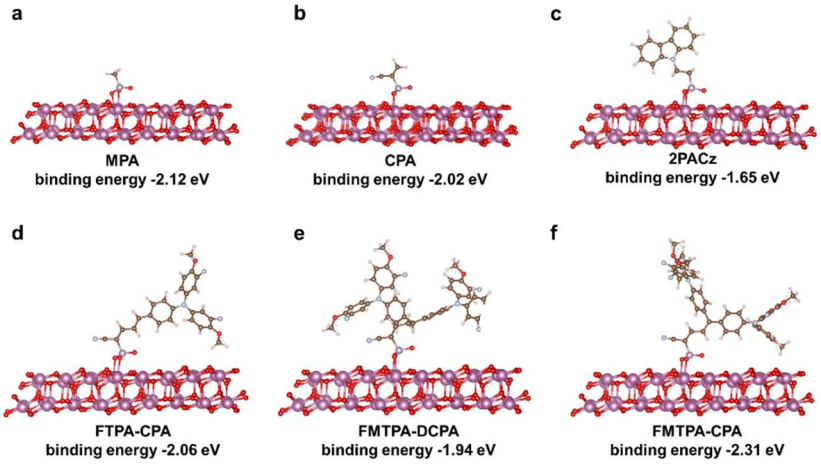

Fig. R27 DFT calculation of the anchoring binding energy of (a) MPA, (b) CPA, (c)

2PACz, (d) FTPA-CPA, (e) FMTPA-DCPA and (f) FMTPA-DCPA with ITO.

For the comment that "*experimentally measure the desorption activation energies for their resonant SAM*", the desorption resistance of SAMs against EtOH and acid washing reflects their desorption activation energies. As described in **Fig. R25** (i.e., **Supplementary Fig. 17** in SI) **& Table R8** (i.e., **Supplementary Table 7** in SI), 2PACz desorbed readily, FTPA-CPA partially desorbed, while the D-A-D resonant FMTPA-CPA remained intact even after AcOH washing, indicating desorption activation energies of FMTPA-CPA > FTPA-CPA> 2PACz. These results confirm that the electronic resonance within the D-A-D structure intrinsically strengthens desorption activation barrier. With a covalent binding energy of −2.31 eV (similar to that of FMTPA-CPA anchoring on ITO), the P-O-In bond is strong enough to avoid dissociation during practical operation.

3. The manuscript discusses preventing desorption but does not explicitly address what causes the covalent P-O-In bond to break in the first place during device operation. Is it primarily thermally activated hydrolysis? Electrochemical reactions driven by bias and moisture? Photochemical degradation? Or mechanical stress from perovskite lattice expansion? A deeper investigation into the failure mechanism of the reference SAMs (2PACz, FTPA-CPA) is needed. Clarifying this root cause is vital to explain why the increased negative charge density from resonance offers superior protection.

Response: Thanks for the reviewer's comments. With more detailed investigations, we prefer to ascribed the covalent P-O-In bond cleavage to the **thermally activated hydrolysis**, where the P-O-In bond was attacked by the protons released from organic cations in perovskite.

To verify the complex degradation mechanism, we firstly check the intrinsic stability of anchored reference SAMs. We prepared 2PACz films with EtOH soaking, which were subjected to five accelerated aging conditions, including high temperature (85±5℃ for 1000 h), light illumination (1000 h), electrical bias stressing (–2.0 V for 10 h), high humidity (85±5% RH for 1000 h), and bending stress (10000 cycles, 5 mm radius). After these accelerated aging tests, XPS characterization revealed no significant changes in **Fig. R28** (i.e., **Supplementary Fig. 65** in SI), indicating robust stability of the pristine 2PACz films.

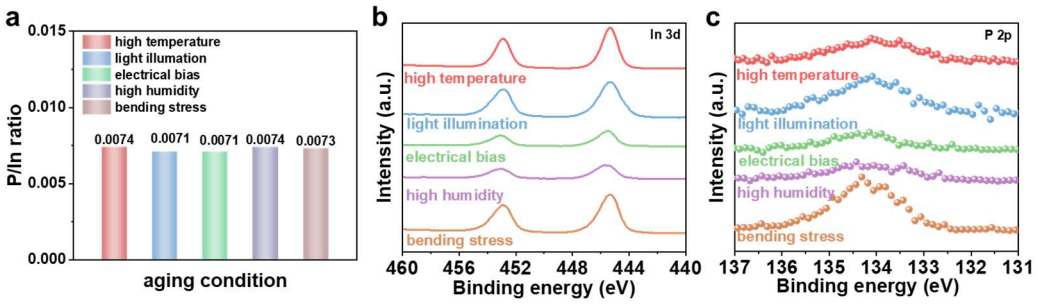

Fig. R28 (i.e., Supplementary Fig. 65 in SI) (a) The P/In ratio, (b) In 3d and (c) P 2p in XPS spectroscopy of 2PACz on ITO substrate before and after aging conditions, including high temperature (85±5℃ for 1000 h), light illumination (1000 h), electrical

bias stressing (-2.0 V for 10 h), high humidity (85±5% RH for 1000 h), and bending stress (10000 cycles, 5 mm radius).

Based on this, the failure mechanism of the reference SAMs should have strong relation with the perovskite layer. We further prepared 2PACz and FTPA-CPA films (still using EtOH soaking to avoid weakly bonded aggregates) with PbI_2 deposition, formamidinium iodide (FAI) deposition and AcOH soaking, respectively, followed by 1000 h of thermal aging in N_2 atmosphere. The samples were subjected to solvent cleaning after aging, and the 2PACz and FTPA-CPA samples with PbI_2 layer on top showed negligible changes. The P/In signal ratios of 2PACz and FTPA-CPA decreased markedly with FAI film deposition, and the SAMs desorption is even more severe after AcOH soaking in **Figs. R29 & R30** (i.e., **Supplementary Figs. 66 & Fig. 67** in SI). Considering both FAI and AcOH can provide proton during long-term heat treatment, these results indicate that **protonic attack under thermal play a key role in activating P-O-In bond cleavage**. In contrast, the P/In ratio of FMTPA-CPA remains nearly unchanged under all aging conditions in **Fig. R30** (i.e., **Supplementary Fig. 67** in SI)**, confirming that its D-A-D electronic resonance fundamentally reinforces the P-O-In bond strength**.

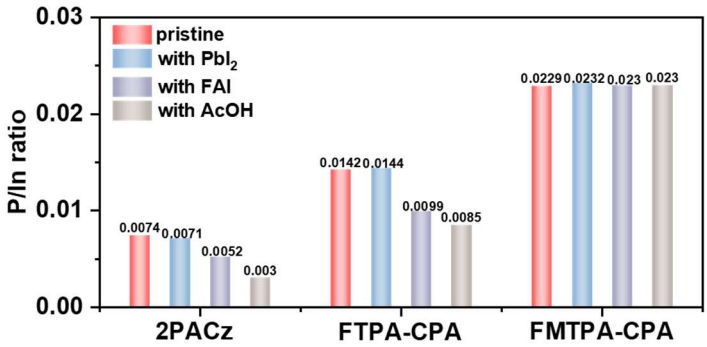

Fig. R29 (i.e., Supplementary Fig. 66 in SI) The P/In ratio of XPS spectroscopy of pristine 2PACz, FTPA-CPA and FMTPA-CPA on ITO substrate and with PbI_2 deposition, FAI deposition and AcOH soaking after aging under high temperature (85±5°C for 1000 h).

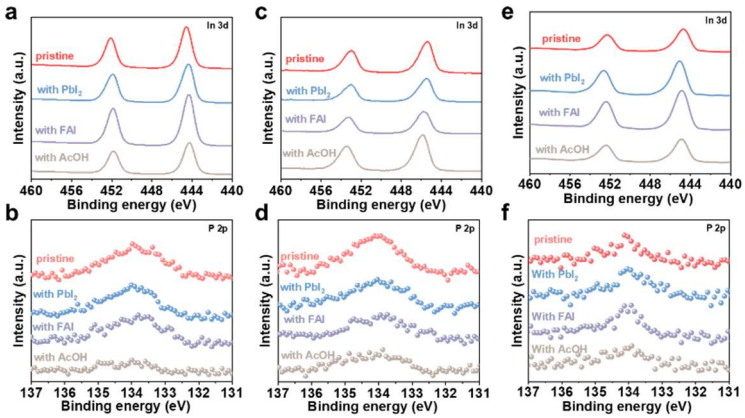

Fig. R30 (i.e., **Supplementary Fig. 67** in SI) XPS spectra of (a) In 3d and (b) P 2p obtained from the pristine 2PACz and 2PACz with PbI_2 deposition, FAI deposition and

AcOH soaking after aging under high temperature (85±5℃ for 1000 h). XPS spectra of (c) In 3d and (d) P 2p obtained from the pristine FTPA-CPA and FTPA-CPA with PbI_2 deposition, FAI deposition and AcOH soaking after aging under high temperature (85±5℃ for 1000 h). XPS spectra of (e) In 3d and (f) P 2p obtained from the pristine FMTPA-CPA and FMTPA-CPA with PbI_2 deposition, FAI deposition and AcOH soaking after aging under high temperature (85±5℃ for 1000 h).

Table R10 (i.e., **Supplementary Table 18** in SI) XPS spectra analysis obtained from the 2PACz, FTPA-CPA and FMTPA-CPA films under multiple failure mechanism.

SAMs	aging condition	In area	P area	P/In
Pristine 2PACz	high temperature (85±5℃ for 1000 h)	934130.12	6941.91	0.0074
	light illumination (1000 h)	1013991.61	7161.91	0.0071
	electrical bias stressing (-2.0 V for 10 h)	456323.60	3250.85	0.0071
	high humidity (85±5% RH for 1000 h)	449742.31	3328.31	0.0074
	bending stress (10000 cycles, 5 mm radius)	1189163.52	8670.55	0.0073
2PACz high temperature (85±5℃ for 1000 h)	pristine	934131.12	6941.91	0.0074
	with PbI_2	956322.65	6747.31	0.0071
	with FAI	1212534.10	6328.28	0.0052
	with AcOH	753585.27	2284.49	0.0030
FTPA-CPA high temperature (85±5℃ for 1000 h)	pristine	524176.56	7426.34	0.0142
	with PbI_2	422221.17	6092.63	0.0144
	with FAI	464195.17	4592.30	0.0099
	with AcOH	654074.12	5560.07	0.0085
FMTPA-CPA high temperature (85±5℃ for 1000 h)	pristine	193731.8	4428.35	0.0229
	with PbI_2	289357.9	6713.91	0.0232
	with FAI	325733.1	7495.70	0.0230
	with AcOH	198972.6	4582.45	0.0230

As the analysis above, we attribute the failure mechanism of P-O-In bond cleavage to thermally activated hydrolysis. During device operation, perovskite degradation can release protonic species (H^+, NH_4^+, or other proton) from FA^+/MA^+ cations (*Nat.*

Commun., 2016, 7, 13422; *Adv. Energy Mater.*, 2020, 10, 1904054). Once accumulated at the ITO substrate, the protonic readily attack the electrophilic P-O moiety in the anchoring group, resulting in protonation of the bridging oxygen and subsequent hydrolytic cleavage of the P-O-In bonds (*Chem. Soc. Rev.*, 1993, 22, 9; *J. Am. Chem. Soc.*, 2009, 131, 39, 14057; *Angew. Chem. Int. Ed.*, 2024, 63, e202404360). With a covalent binding energy of –2.31 eV (similar to that of FMTPA-CPA anchoring on ITO), the P-O-In bond is strong enough to avoid dissociation during practical operation.

$$\text{P-O-In} + H^+ \rightarrow \text{P-OH}^+\text{-O-In} \rightarrow \text{P-OH} + \text{In-OH}$$

The corresponding revisions for the revised Manuscript and revised Supplementary Information (marked red) are listed below:

Pages 12~13 in the revised Manuscript: Considering the potential extreme harsh working environments, the FMTPA-CPA-based devices maintained 98% of their initial PCEs over 1080 h under damp heat (85±5%RH & 85±5°C) aging, whereas the devices with FTPA-CPA and 2PACz SAMs retained only 76% and 53% of their initial PCEs respectively, within the same aging time (**Supplementary Fig. 63**). The enhanced stability originates from the robust monolayer covalent anchoring of FMTPA-CPA, avoiding protonation activated hydrolysis of anchoring group under multiple stability protocol (**Supplementary Figs. 64-67 & Tables 17-18 & Supplementary Note 7 & Note 11**).

Pages 19~20 in the revised Supplementary Information:

Supplementary Note 11 Stability Mechanism Analysis

With more detailed investigations, we prefer to ascribed the covalent P-O-In bond cleavage to the thermally activated hydrolysis, where the P-O-In bond was attacked by the protons released from organic cations in perovskite.

To verify the complex degradation mechanism, we firstly check the intrinsic stability of anchored reference SAMs. We prepared 2PACz films with EtOH washing, which were subjected to five accelerated aging conditions, including high temperature (85±5℃ for 1000 h), light illumination (1000 h), electrical bias stressing (−2.0 V for 10 h), high humidity (85±5% RH for 1000 h), and bending stress (10000 cycles, 5 mm radius). After these accelerated aging tests, XPS characterization revealed no significant changes in **Supplementary Fig. 65**, indicating environmental stability of the pristine 2PACz films.

Based on this, the failure mechanism of the reference SAMs should have strong relation with the perovskite layer. We further prepared 2PACz and FTPA-CPA films (still using EtOH washing to avoid weakly bonded aggregates) with PbI_2 deposition, formamidinium iodide (FAI) deposition and AcOH soaking, respectively, followed by 1000 h of thermal aging in N_2 atmosphere. The 2PACz and FTPA-CPA samples with PbI_2 layer on top showed negligible changes. The P/In signal ratios of 2PACz and FTPA-CPA decreased markedly with FAI film deposition, and the SAMs desorption is even more severe after AcOH soaking in **Supplementary Fig. 66 & Fig. 67**. Considering both FAI and AcOH can provide proton during long-term heat treatment, these results indicate that protonic attack under thermal play a key role in activating P-

O-In bond cleavage. In contrast, the P/In ratio of FMTPA-CPA remains nearly unchanged under all aging conditions in **Supplementary Fig. 66**, confirming that its D-A-D electronic resonance fundamentally reinforces the P-O-In bond strength.

As the analysis above, we attribute the failure mechanism of P-O-In bond cleavage to thermally activated hydrolysis. During device operation, perovskite degradation can release protonic species (H^+, NH_4^+, or other proton) from FA^+/MA^+ cations.[27, 28] Once accumulated at the ITO substrate, the protonic readily attack the electrophilic P-O moiety in the anchoring group, resulting in protonation of the bridging oxygen and subsequent hydrolytic cleavage of the P-O-In bonds).[29-31] With the covalent binding energy of -2.31 eV between FMTPA-CPA and ITO, the P-O-In bond is strong enough to suppress proton attack. With a covalent binding energy of -2.31 eV (similar to that of FMTPA-CPA anchoring on ITO), the P-O-In bond is strong enough to avoid dissociation during practical operation.

$$\text{P-O-In} + H^+ \rightarrow \text{P-OH}^+\text{-O-In} \rightarrow \text{P-OH} + \text{In-OH}$$

4. The description of FMTPA-CPA as a "D-A-D" structure is chemically misleading. The two TPA donors are not conjugated to each other through the acceptor. They are independently linked to the central cyanovinyl bridge. Therefore, the electronic structure is better described as two independent D-(π-A) pathways or a symmetric double-D-A system, not a delocalized D-A-D triad.
In addition, comparing FMTPA-CPA (with a CPA anchor) to 2PACz (with a simpler PA anchor) is problematic because the anchoring chemistry itself is different. The observed improvements could be partly attributable to the inherent properties of CPA group (stronger acidity, different coordination geometry) rather than solely the resonance effect. A much fairer and more critical control would be a non-resonant SAM molecule featuring the exact same CPA anchoring group, but without the symmetric donor structure. This control is essential to isolate the effect of the resonant electronic structure.

Response: Thanks for the reviewer' comments. We separately reply to the two comments below:

For the comment that "*The description of FMTPA-CPA as a "D-A-D" structure is chemically misleading*", we want to provide a more comprehensive explanation of the rationale behind our nomenclature. The nomenclature of the designed molecule FMTPA-CPA was inspired by the D-A-D architecture commonly adopted in organic photovoltaic (OPV) systems (*Nat. Rev. Mater.*, 2025, 10, 617; *Nat. Mater*., 2025, 24, 444; *Angew. Chem. Int. Ed*., 2025, 64, e202506252). In this D-A-D configuration, the HOMOs are typically delocalized and both two donor moieties are π-conjugated with the central acceptor core. In our study, each TPA group in FMTPA-CPA is indeed linked to the CPA acceptor group through a conjugated bridge; but the calculated HOMO wavefunctions exhibit pronounced delocalization of the HOMO over both TPA donor groups and the conjugated bridge (**Fig. 1b**). This suggests effective electronic coupling between the two TPA units mediated by the conjugated bridge, rather than complete isolation, that behaves functionally as the common D-A-D-type molecules.

For the reviewer's suggestion that "*the electronic structure is better described as two independent D-(π-A) pathways*", we feel that it emphasizes the D-A interaction while can hardly capture the strategic inclusion of delicate electronic resonance between two donor groups. To enable a more precise description of the FMTPA-CPA molecular design, we finally decide to use "D-A-D resonance" structure.

In response to the suggestion "*A much fairer and more critical control would be a non-resonant SAM molecule featuring the exact same CPA anchoring group, but without the symmetric donor structure*". D-A-D electronic resonance in FMTPA-CPA arises when two electron donors and electron acceptor units connected through a conjugated bridge to form an axially symmetric molecular structure, which is similar to the common D-π-D electronic resonance. In the manuscript, we chose FTPA-CPA featuring only one TPA donor group and CPA acceptor group as the control sample "*featuring the exact same CPA anchoring group, but without the symmetric donor structure*". Unlike FMTPA-CPA, FTPA-CPA only exhibits charge redistribution between donor moiety and acceptor moiety, but has no D-A-D electronic resonance.

To have a clearer clarification, we replace the "D-A-D" with the specific "D-A-D resonance" in the revised manuscript (marked red).
Page 3 in the revised Manuscript: Here, we develop a strong donor-acceptor-donor (D-A-D) resonant SAM molecule FMTPA-CPA featuring two symmetric…
Page 4 in the revised Manuscript: In addition, the symmetric donor TPA groups and the conjugated linker results in D-A-D resonance stabilized charge delocalization…
Page 10 in the revised Manuscript: At the same time, the FMTPA-CPA with strong D-A-D resonance features a delocalized charge distribution, which affects the surface energetic alignment and charge extraction…

To further investigate how donor asymmetry influences electronic resonance and anchoring strength, we designed **two D-A-D' SAMs**, FTPAPh-CPA (TPA and benzene) and FTPACz-CPA (TPA and carbazole) **(Fig. R31)**. Given the synthesis complexity and multiple side reactions, the electronic resonance characteristics and anchoring strengths were evaluated by DFT calculations.

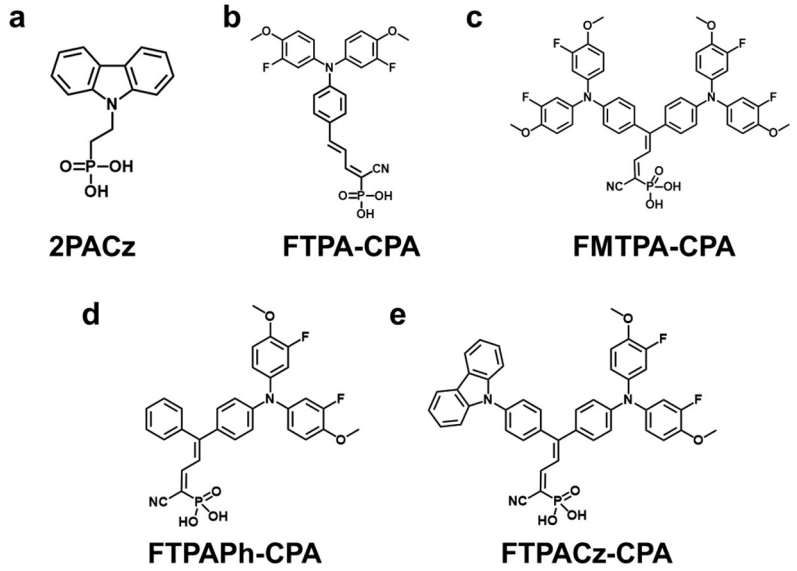

Fig. R31 molecular structures of (a) 2PACz, (b) FTPA-CPA, (c) FMTPA-CPA, (d) FTPAPh-CPA and (e) FTPACz-CPA.

DFT calculations (**Fig. R32)** revealed that FTPAPh-CPA (6.0 D) and FTPACz-CPA (6.5 D) possess smaller molecular dipole moments than that of FMTPA-CPA (10.5 D). Both FTPAPh-CPA and FTPACz-CPA exhibit HOMO wavefunctions delocalization over the donor units. However, owing to the weak electron-donating ability of the phenyl ring in FTPAPh-CPA and the poor coplanarity in FTPACz-CPA between the Cz and TPA, the HOMO wavefunction is scarcely distributed on the phenyl and Cz moieties. Accordingly, the electrostatic potential on the phosphonic acid group follows the trend FTPA-CPA < FTPAPh-CPA<FTPACz-CPA < FMTPA-CPA, consistent with the electrostatic potential in **Table R11**.

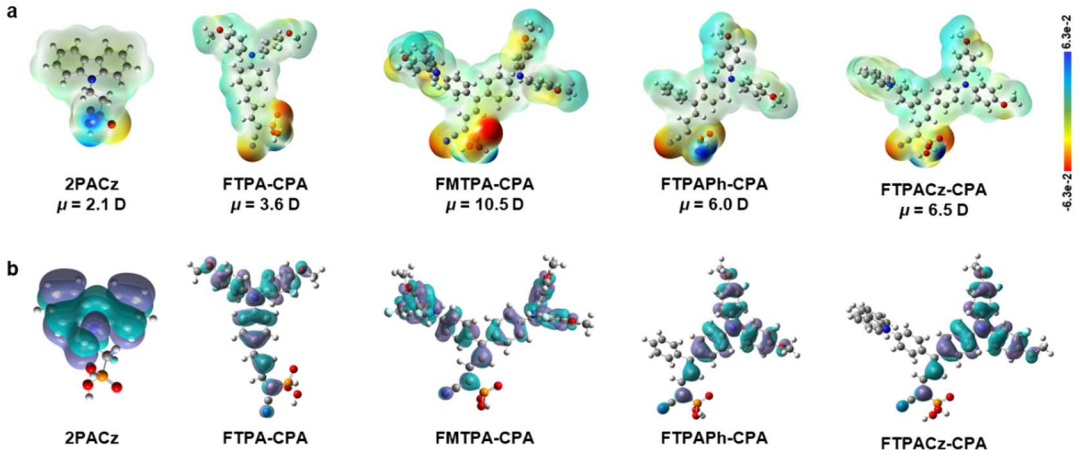

Fig. R32 (a) ESP distributions and corresponding dipole moments of 2PACz, FTPA-CPA, FMTPA-CPA, FTPAPh-CPA and FTPACz-CPA. (b) HOMO orbital distributions of 2PACz, FTPA-CPA, FMTPA-CPA, FTPAPh-CPA and FTPACz-CPA.

Table R11 The electrostatic potential of oxygen atoms within phosphate groups from ESP calculation.

SAMs	-P-OH(1) (kcal/mol)	-P-OH(2) (kcal/mol)
2PACz	–6.45	–6.46
FTPA-CPA	–18.88	–14.61
FMTPA-CPA	–20.72	–15.61
FTPAPh-CPA	–19.76	–15.70
FTPACz-CPA	–19.66	–13.60

DFT calculations show that electron-resonance critically determines SAM anchoring on ITO (**Fig. R33**). FTPAPh-CPA exhibits slightly stronger binding energy (–2.12 eV) than FTPA-CPA (–2.06 eV), while FTPACz-CPA (–2.25 eV) still weaker than FMTPA-CPA (–2.31 eV). Thus, although incorporating two asymmetric donors with strong electron-donating ability can increase the charge redistribution to some extent, its contribution to electronic resonance remains limited due to the reduced coplanarity. These results suggest that designing strong symmetric donors with higher coplanarity is more effective in promoting electronic resonance within the SAMs.

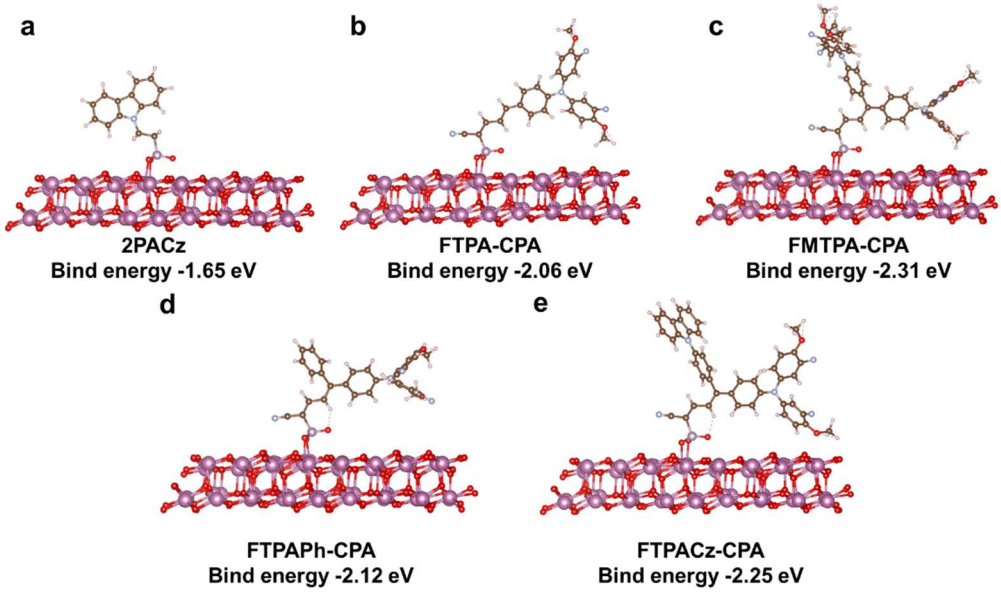

Fig. R33 DFT calculation of the anchoring binding energy of (a) 2PACz, (b) FTPA-CPA, (c) FMTPA-CPA, (d) FTPAPh-CPA and (d) FTPACz-CPA with ITO.

5. The 1H NMR and 13C NMR of FTPA-CPA seems not so pure. The authors should input details 13C NMR data of FTPA-CPA and FMTPA-CPA in the experimental part, and provide their element analysis data to confirm the purity of final SAM materials.

Response: We appreciate the reviewer' comments. We checked the ^{1}H and ^{13}C nuclear magnetic resonance (NMR) of FTPA-CPA and find the impurity signal (3.60, 3.44, 4.02 in ^{1}H NMR; 31.43 in ^{13}C NMR) comes from the remained petroleum ether and methanol which is used for FTPA-CPA purification. Considering the low boiling point of petroleum ether and methanol solvents, we **subsequently dried the material at**

50 °C for 24 h to fully remove residual trace solvent. After this, the ^{1}H NMR and ^{13}C NMR of FTPA-CPA was conducted again and the corrected results **are presented in Fig. R34** (i.e., **Supplementary Fig. 1** in SI) **& Fig. R35** (i.e., **Supplementary Fig. 2** in SI).

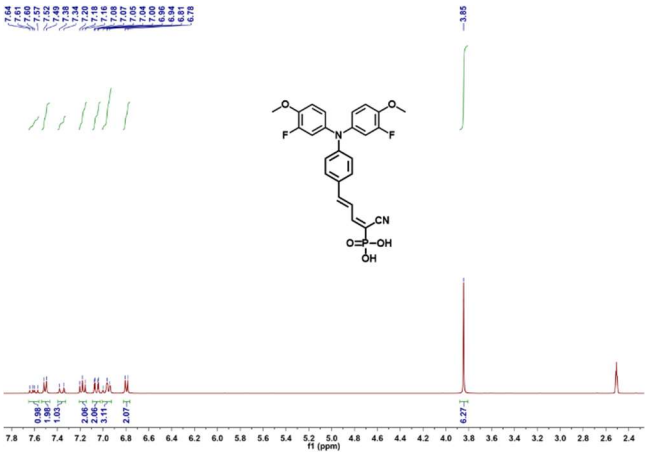

Fig. R34 (i.e., Supplementary Fig. 1 in SI) ^{1}H NMR spectrum of FTPA-CPA.

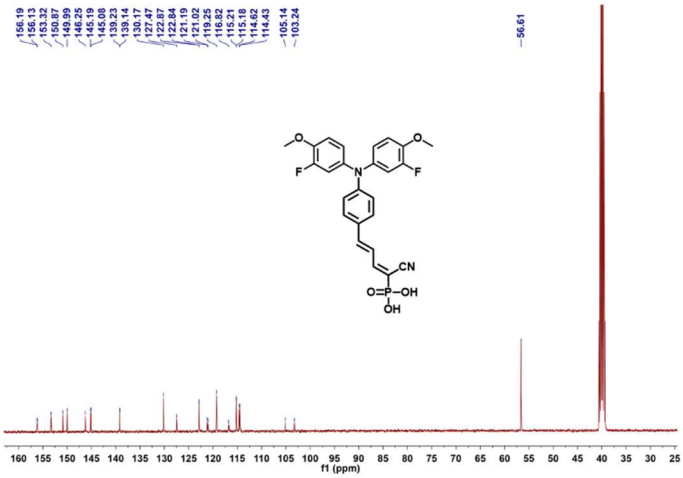

Fig. R35 (i.e., Supplementary Fig. 2 in SI) ^{13}C NMR spectrum of FTPA-CPA.

To assess the possible impact of trace residual solvent on device performance, the devices were fabricated and tested. The results demonstrate that the presence of petroleum ether does not significantly affect the device photovoltaic performance as shown in **Table R12 & Fig. R36,** which may be ascribed to that the residual trace volatile solvent can be removed during SAMs annealing process. In addition, detailed ^{13}C NMR data of FTPA-CPA and FMTPA-CPA are provided in the experimental part of the Supplementary Materials.

Table R12 Photovoltaic parameters of the pero-SCs based on FTPA-CPA before and after dried under AM1.5G, 100 mW/cm^2 illumination.

SAMs	V_{oc} (V)	J_{sc} (mA/cm^2)	FF (%)	PCE$_{max}$[a](PCE$_{avg}$)[a] (%)
original FTPA-CPA	1.20±0.02	26.53±0.12	82.6±1.4	26.21±0.14
New FTPA-CPA	1.20±0.02	26.46±0.13	82.5±1.1	26.10±0.24

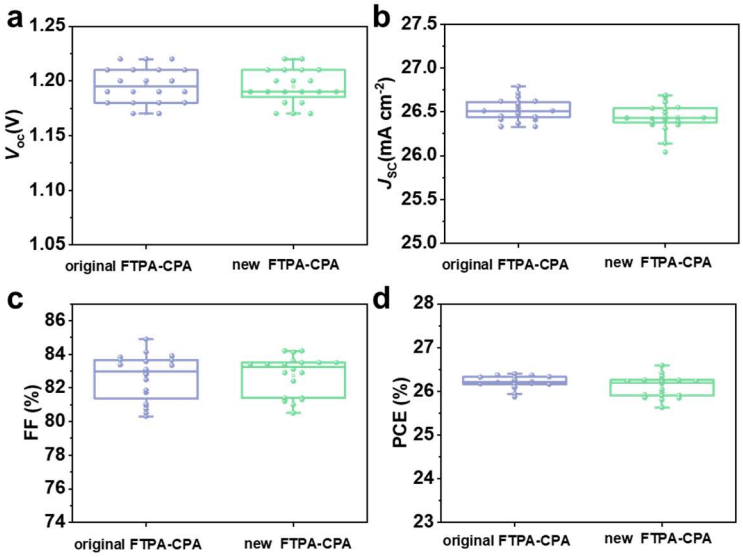

Fig. R36 The statistics (a) V_{oc}, (b) J_{sc}, (c) FF and (d) PCE values obtained from *J-V* characteristic for the devices based on FTPA-CPA before and after dried.

In addition, to follow the reviewer's suggestion, elemental analysis is performed for C, H, and N using the Elemental Analyzer as shown in **Table R13** (i.e., **Supplementary Table 1** in SI). The C, H, N results match well with the theoretical values calculated from the molecular formula, indicating the high purity of the organic framework of the SAMs. Because F, O, and P cannot be determined by the Elemental Analyzer method, their presence is confirmed by energy dispersive spectrometer (EDS) measurements (**Fig. R37**), which are consistent with the molecular structures. NMR and elemental analysis consistently confirm the high purity of the synthesized FTPA-CPA.

Table R13 (i.e., **Supplementary Table 1** in SI) The element mass of FTPA-CPA and FMTPA-CPA.

Molecule	C (wt%)	N (wt%)	H (wt%)	CHN result	Molecular formula
FTPA-CPA	5.34	57.25	4.03	$NC_{12.51}H_{10.49}$	$N_2C_{25}H_{21}F_2O_5P$
FMTPA-CPA	5.60	71.98	4.83	$NC_{14.99}H_{11.99}$	$N_3C_{45}H_{36}F_4O_7P$

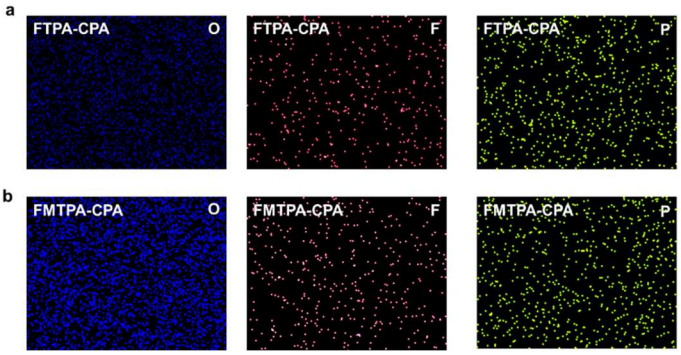

Fig. R37 The EDS element analysis of (a) FTPA-CPA and (b) FMTPA-CPA.

The corresponding revisions for the revised manuscript and revised Supplementary Information (marked red) are listed below:

Pages 4~5 in the revised Manuscript: We synthesize and compare the intramolecular charge transfer characteristics of the three self-assemble monolayers (SAMs) molecules: (2-Carbazol-9-ylethyl)-phosphonic acid (2PACz), ((1Z,3E)-4-(4-(bis(3-fluoro-4-methoxyphenyl)amino)phenyl)-1-isocyanobuta-1,3-dien-1-yl)phosphonic acid (FTPA-CPA) and (resonant-D)-π-A type conjugated (Z)-(4,4-bis(4-(bis(3-fluoro-4-methoxyphenyl)amino)phenyl)-1-isocyanobuta-1,3-dien-1-yl)phosphonic acid (FMTPA-CPA) (the synthesis route of FTPA-CPA and FMTPA-CPA are shown in **Supplementary Note 1**, and the molecular structures were confirmed by ^{1}H, ^{13}C nuclear magnetic resonance (NMR) spectrum, mass spectroscopy (MS) and elemental analysis, (**Supplementary Figs. 1-8 & Supplementary Table 1 & Note 1**).

Pages 3~4 in the revised Supplementary Information:

Compound **3** (3.6 g, 6.5 mmol) and TMSBr (16.8 g, 110 mmol) were added in a flask, then dichloromethane (125 mL) was us ed to dissolve them. Under an argon atmosphere, the mixture was stirred at room temperature overnight. After reaction completion, add 10 mL of methanol to quench the reaction. The solvent was distilled off under reduced pressure. The residue was added to petroleum ether to obtain the product as a yellow solid FTPA-CPA (Compound **4**) (2.5 g, 78% yield). ^{1}H NMR (600 MHz, DMSO-*d*6) δ 7.61 (dd, J=17.0, 11.3 Hz, 1H), 7.51 (d, J=8.8 Hz, 2H), 7.36 (d, J=15.1 Hz, 1H), 7.18 (t, J=9.3 Hz, 2H), 7.06 (dd, J=12.6, 2.6 Hz, 2H), 7.01 – 6.93 (m, 3H), 6.80 (d, J=8.9 Hz, 2H), 3.85 (s, 6H). ^{13}C NMR (101 MHz DMSO-d_6) δ 156.19, 156.13, 153.32, 150.87, 149.99, 146.25, 145.19, 145.08, 139.23, 139.14, 130.17, 127.47, 122.87, 122.84, 121.19, 121.02, 119.25, 116.82, 115.21, 115.18, 114.62, 114.43, 105.14, 103.24, 56.61. HR-MS (MALDI-TOF) m/z calcd. for ($C_{25}H_{21}F_2N_2O_5P$): 498.19. Found: 498.19.

Compound **6** (3.8 g, 4.2 mmol) and TMSBr (10.7 g, 70 mmol) were added in a flask, then dichloromethane (80 mL) was used to dissolve them. Under an argon atmosphere, the mixture was stirred at room temperature overnight. After reaction completion, add 10 mL of methanol to quench the reaction. The solvent was distilled off under reduced pressure. The residue was added to petroleum ether to obtain the product as a yellow solid FMTPA-CPA (Compound **7**) (2.6 g, 73% yield). ^{1}H NMR (600 MHz, DMSO-*d*6) δ 8.37 (s, 1H), 7.38 (dd, J=16.9, 11.8 Hz, 1H), 7.20 (d, J=8.8 Hz, 2H), 7.14 (dt, J=9.3, 4.6 Hz, 4H), 7.06 (dd, J=12.5, 2.3 Hz, 2H), 7.04 – 6.98 (m, 4H), 6.96 (d, J=8.4 Hz, 2H), 6.92 (d, J=8.6 Hz, 2H), 6.85 – 6.82 (m, 1H), 6.80 (d, J=8.5 Hz, 2H), 6.77 (d, J=8.8 Hz, 2H), 3.81 (s, 12H). ^{13}C NMR (151 MHz, DMSO-d_6) δ 152.92, 151.26, 149.62, 148.81, 145.01, 144.94, 139.43, 139.33, 131.97, 130.33, 122.82, 122.70, 119.12, 118.68, 115.20, 114.56, 114.44, 114.32, 56.60, 51.86, 44.14. HR-MS (MALDI-TOF) m/z calcd. for ($C_{47}H_{40}F_4N_3O_7P$): 837.32. Found:837.32.

6. The claim in Fig. 1c and the text that the HOMO orbital distribution "confirms the formation of delocalized diradicals" is unsubstantiated and likely incorrect. The plotted HOMO is a ground-state molecular orbital, not a singly occupied molecular orbital (SOMO) characteristic of a radical. The presence of diradicals or radical character should be investigated through proper theoretical methods. Relying on the HOMO plot for such a claim weakens the theoretical analysis.

Response: Thanks for the reviewer' comments and correction. We agree that the original description "*In addition, the dual broad peaks in ESR signal of FMTPA-CPA implies the formation of delocalized diradicals on the electron donating and accepting groups separately, which is also confirmed by electronic orbitals calculations (Fig. 1c)*" is misleading. As the reply to previously comment 2 of Reviewer#1, the ground-state molecular orbital (HOMO and LUMO) indeed cannot verify the radical character. Our aim is to confirm the charge redistribution between donor moiety and acceptor moiety in FMTPA-CPA through the HOMO and LUMO calculation.

To follow the suggestions on "*The presence of diradicals or radical character should be investigated through proper theoretical methods.*", we analyze radical character by fractional occupation density number (N_{FOD}) calculation (*PCCP*, 2025, 27, 5973). A larger N_{FOD} indicates obvious radical character. Based on the N_{FOD} analysis, the 2PACz showing very low N_{FOD} (0.10) consistent with negligible radical character in **Table R14** (i.e., **Supplementary Table 2** in SI). Intermediate values for FTPA-CPA (0.43) suggest moderate radical character, while FMTPA-CPA (0.66) exhibit significantly higher N_{FOD} values, implying stronger radical character. The N_{FOD} results therefore provide a more appropriate theoretical basis for discussing radical character.

Table R14 (i.e., **Supplementary Table 2** in SI) The N_{FOD} values of 2PACz, FTPA-CPA and FMTPA-CPA.

Molecule	2PACz	FTPA-CPA	FMTPA-CPA
N_{FOD}	0.10	0.43	0.66

We have revised the corresponding contents accordingly in the the revised Manuscript (marked red).

Page 5 in the revised Manuscript: In FMTPA-CPA, the further red-shifted absorption peak to ~540 nm and strong broad peaks in ESR signal exhibits the enhanced radical character (**Fig. 1e**), which indicates the more pronounced intramolecular charge redistribution (~0.178 e) between donor moiety and acceptor moiety, resulting in negative charge gathering in CPA group of FMTPA-CPA (**Supplementary Figs. 9-10 & Supplementary Note 2 & Table 2**).

Pages 5~6 in the revised Manuscript: To further explore the origin of the enhanced charge redistribution between donor moiety and acceptor moiety in FMTPA-CPA, we refer to molecular orbital calculations and electrostatic surface potential (ESP) calculations (**Figs. 1b & 1c & Supplementary Fig. 11**). The almost complete overlap of the highest occupied molecular orbital (HOMO) and lowest unoccupied molecular orbital (LUMO) orbital wavefunctions in 2PACz implies a negligible charge redistribution between carbazole group and phosphonic acid group, thus the phosphonic acid group shows negligible negative charge density and the molecular dipole moment is only 2.1 D. For FTPA-CPA, the conjugated linker facilitates charge redistribution between TPA and CPA groups, leading to partial overlapped HOMO and LUMO wavefunction distribution, and higher negative charge density on anchoring group, making the molecular dipole moment increase to 3.6 D. For FMTPA-CPA, we observe less overlap of the HOMO and LUMO wavefunctions, as well as much improved negative charge density on anchoring group and a substantial molecular dipole moment

of 10.5 D. At the same time, from the DFT calculations, we notice the strong electronic resonance across the D-A-D FMTPA-CPA, which plays a key role in bringing the enhanced charge redistribution.

Page 11 in the revised Supplementary Information:

Supplementary Note 2. Ground-state geometry optimizations and radical character analysis

To analyze diradical character by theoretical methods, fractional occupation density number (N_{FOD}) was calculated.[6] A larger N_{FOD} indicates obvious radical character. Based on the N_{FOD} analysis, the 2PACz showing very low N_{FOD} (0.10) consistent with negligible radical characteristics in **Supplementary Table 2**. Intermediate values for FTPA-CPA (0.43) suggest moderate radical characteristics, while FMTPA-CPA (0.66) exhibit significantly higher N_{FOD} values, implying stronger radical characteristic. The N_{FOD} results therefore provide a more appropriate theoretical basis for discussing radical character.

Fractional occupation density (FOD) analysis was carried out using the ORCA quantum chemistry program package (version 4.2.1).[7] The calculations were performed at the FOD-DFT level employing the TPSS functional in combination with the def2-TZVP basis set. A Fermi-Dirac smearing temperature of 5000 K was applied to introduce fractional occupations, enabling visualization and quantification of static correlation effects and polyradical character.

7. The in-situ FTIR signals (Fig. 2g-i; Fig. S13) are surprisingly strong for a SAM layer. Were these spectra collected on well-defined monolayers or on as-deposited films that may contain multilayers/physiosorbed material? If they are from monolayers, what experimental setup (grazing incidence, multiple internal reflections) was used to achieve sufficient sensitivity? This detail is crucial, as conventional transmission FTIR is notoriously insensitive to sub-nanometer layers. If they are form multilayers, the observed peak shifts and decrease in intensity for 2PACz and FTPA-CPA could be due to the desorption of weakly bound multilayers rather than changes in the bonded monolayer. Control experiments verifying the monolayer nature of the initial film are necessary to interpret these FTIR trends correctly.

Response: Thanks for the reviewer' professional comments. About your concerns on the signal intensity of monolayers and sensitivity of Fourier transform infrared (FTIR) measurement set up, we performed *in-situ* FTIR spectroscopy in the reflection mode at grazing incidence of ~70° (relative to the normal of substrates) rather than conventional transmission mode, and the signals were collected using a high-sensitivity mercury-cadmium-telluride (MCT) detector. This mode ensures detectable signal intensity even with ultra-thin monolayer samples (*Nat Commun.*, 2025, 16, 4516; *Nature*, 2023, 624, 289; *Adv. Energy Mater.*, 2018, 8, 1801892).

For the comment that "*Were these spectra collected on well-defined monolayers or on as-deposited films that may contain multilayers/physiosorbed material?*". The SAM films were prepared on ITO substrates *via* spin-coating followed by EtOH washing. As noted earlier (Response to Comment 1 of Reviewer#3), the initial coverage for

2PACz and FTPA-CPA may involve few multilayers or aggregates, whereas the electronic resonance FMTPA-CPA forms robust covalently anchored monolayers after EtOH washing.

For the comment that "*grazing incidence, multiple internal reflections*" and "*This detail is crucial, as conventional transmission FTIR is notoriously insensitive to sub-nanometer layers.*". For ultrathin films at the nanometer scale, the path length is extremely small, leading to very low absorbance and consequently weak signal-to-noise ratios (Roodenko, K., etc., *Ellipsometry of Functional Organic Surfaces and Films* (Part: Springer Series in Surface Sciences)). As a result, conventional transmission IR is not sufficiently sensitive for nanoscale films unless the material exhibits very strong absorption bands or the spectrum is enhanced by specialized techniques.

To overcome this, the *in-situ* FTIR spectroscopy in our work was performed in the reflection mode at grazing incidence of ~70° (relative to the normal of substrates) rather than conventional transmission. Such geometry enhances surface sensitivity to the vibrational features of molecular groups at the surface (*Energy Environ. Mater.*, 2025, 8, e70059). Moreover, the FTIR spectra were collected using a high-sensitivity MCT detector, which incorporates a multi-mirror optical design to maximize signal collection efficiency as shown in **Fig. R38**. Owing to its high sensitivity and fast response, the MCT detector enables real-time monitoring of sub-nanometer-thick organic layers on oxide substrates (*Nat Commun.*, 2025, 16, 4516; *Nature*, 2023, 624, 289; *Adv. Energy Mater.*, 2018, 8, 1801892).

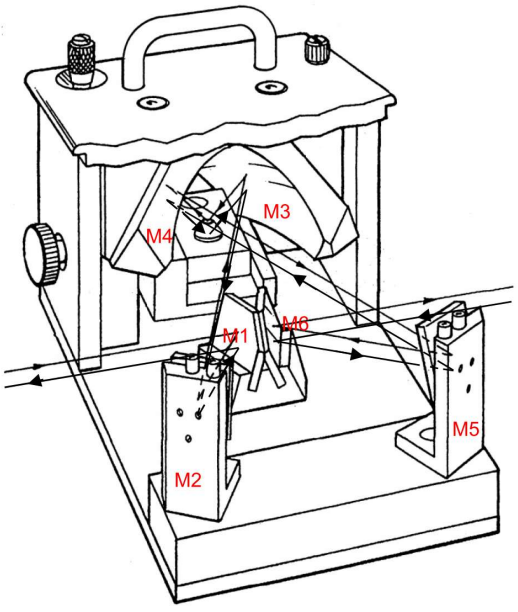

Fig. R38 Interior view of the MCT detector.

For the comment that "*Control experiments verifying the monolayer nature of the initial film are necessary to interpret these FTIR trends correctly.*", we have verified that EtOH washing can remove the vast majority of weakly bonded SAMs or aggregates to remain covalent anchored monolayer, while the AcOH washing can partially break the covalent

bonded 2PACz and FTPA-CPA in the response to the Comment 1 of reviewer #3. Based on this analysis, to further elucidate if the origin of the spectral variations comes from the monolayer, comparative *in-situ* FTIR measurements were performed on the SAMs after AcOH washing, as shown in **Fig. R39** (i.e., **Fig. 2e** in main text). Even after acid washing, the characteristic bands ($-PO_3^{2-}$) still exhibited a noticeable blue shift for 2PACz and FTPA-CPA, indicating that the spectral evolution originates from intrinsic structural changes within the P-O-In bond.

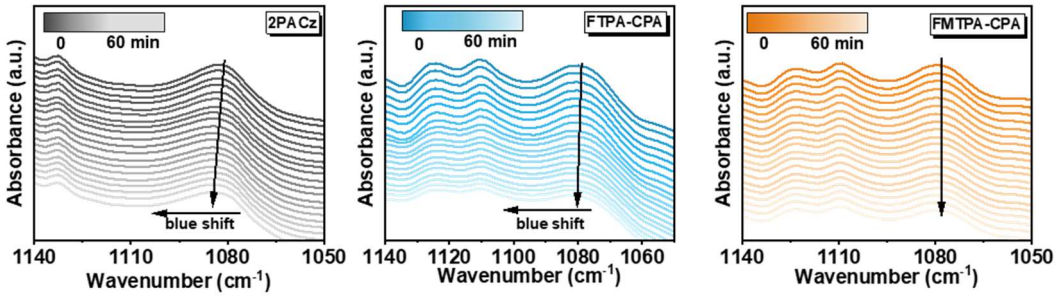

Fig. R39 (i.e., **Fig. 2e** in main text) *In situ* FTIR spectra of the 2PACz, FTPA-CPA and FMTPA-CPA films with AcOH washing on ITO substrate at 85°C.

The corresponding revisions for the revised Manuscript and revised Supplementary Information (marked red) are listed below:

Page 7 in the revised Manuscript: By contrast, the wavenumbers of FMTPA-CPA remain stable, confirming the survive of robust bidentate binding between FMTPA-CPA and ITO even at high temperature (85°C, **Supplementary Fig. 20**; 100°C, **Supplementary Fig. 21**).[9,32] The similar trend in an additional *in situ* high-temperature FTIR measurement on AcOH washed samples make sure the FTIR results indeed reflect the covalent bond cleavage process (**Fig. 2e**).

Page 7 in the revised Supplementary Information:

***In situ* Fourier transform infrared (FTIR) spectra.** *In situ* FTIR spectra were performed on a Thermo Fisher Scientific Nicolet iS50 spectrometer equipped with a Harrick high-temperature cell with ZnSe windows and a high-sensitivity mercury-cadmium-telluride (MCT) detector. Typically, an acquisition time of 30 s at a resolution of 4 cm^{-1} was used for spectrum collection. The SAM samples by coated on the ITO substrate was heated up at 85 or 100°C before the test. Then, keep the sample at 85 °C or 100°C while continuously monitoring the signal for one hour. The SAM film was prepared on an ITO substrate via spin-coating, followed by ethanol or AcOH washing.

8. For the probing PO3H2- signal in Tof-SIMS data (Fig. S14), once the phosphonic acid anchors to ITO, it loses protons to form P-O-In bonds. The PO3H2- signal, therefore, predominantly originates from non-bound or protonated species such as free molecules, molecules bonded in a monodentate fashion retaining an -OH, or molecules that have hydrolyzed from the surface. Tracking its diffusion into the perovskite may not report on the stability of the covalently anchored monolayer but rather on the mobility of loosely associated acidic species. The authors should justify this choice and complement it with a signal more specific to the anchored state. In addition, the

significant noise near the baseline in the PO3H2- profiles for samples in Fig. S14c,d are concerning. The authors should explain the potential source of this noise.

Response: Thanks for the reviewer's rigorous comments and correction. In the original manuscript, we denote the signal -PO_3H_2 to represent the SAM. In fact, the observed signal originates from the fragment peak of the SAM, namely the -PO^- moiety, rather than intact protonated phosphonic species. Therefore, to ensure description accuracy and avoid misunderstanding, we have revised the notation of this fragment peak signal to -PO^- in **Fig. 2j & 2h & Fig. R40** (i.e., **Supplementary Fig. 22** in SI, original **Supplementary Fig. 14**).

About the concern that *"tracking the diffusion into the perovskite may not reflect the stability of the covalently anchored monolayer but rather the mobility of loosely associated acidic species"*, as we discussed in the response of comment 1 of Reviewer #3, the EtOH washing can remove the vast majority of weakly bonded or loosely associated SAMs. In addition, during the spin-coating of perovskite layer, the precursor solutions typically contain highly polar solvents such as N, N-dimethylformamide (DMF) and dimethyl sulfoxide (DMSO). If there remain unanchored SAM molecules, the perovskite deposition could facilitate their incorporation into the perovskite film. Experimentally, in fresh devices based on 2PACz, FTPA-CPA, and FMTPA-CPA, **all -PO^- signals are detected in a narrow spatial distribution between ITO and perovskite and no -PO^- signals can be detected inside perovskite layer.** This observation indicates that the EtOH washing during SAM preparation efficiently removes mostly unanchored molecules and thus prevents adverse effects of unanchored SAM molecule on the subsequent device long-term stability.

In addition, concerning *"the significant noise near the baseline in the -PO3H2 profiles for samples in Fig. S14c, d"*, we consulted the instructor responsible for time-of-flight secondary ion mass spectrometry (ToF-SIMS) measurements. This issue was attributed to instrumental factors: during that measurement, the high-sensitivity mode of the instrument was inoperative, and only the low-sensitivity mode could be used. In the low-sensitivity mode, the measured signal intensity was relatively weak, resulting in the increased normalized noise level. Although this led to a reduction in overall signal intensity, it did not affect the analysis of the measurement results. To reduce the signal noise, we aged the perovskite films based on FTPA-CPA and repeated the measurements under high-sensitivity mode. As shown in the **Fig. R40** (i.e., **Supplementary Fig. 22** in SI), the retested data now avoids the significant noise issue.

The corresponding revisions for the revised Manuscript (marked red) are listed below:
Pages 7~8 in the revised manuscript: For the ITO/2PACz/perovskite and ITO/FTPA-CPA/perovskite samples, along with the aging time evolution, the PO^- signals tracked from time-of-flight secondary ion mass spectrometry (ToF-SIMS) evolve from a narrow spatial distribution between ITO and perovskite to a broad distribution across the whole perovskite layer (**Fig. 2f** & **Supplementary Fig. 22**). In contrast, ITO/FMTPA-CPA/perovskite sample displays negligible distribution evolution of the PO^- signal, showing a narrow spatial distribution between ITO and perovskite.

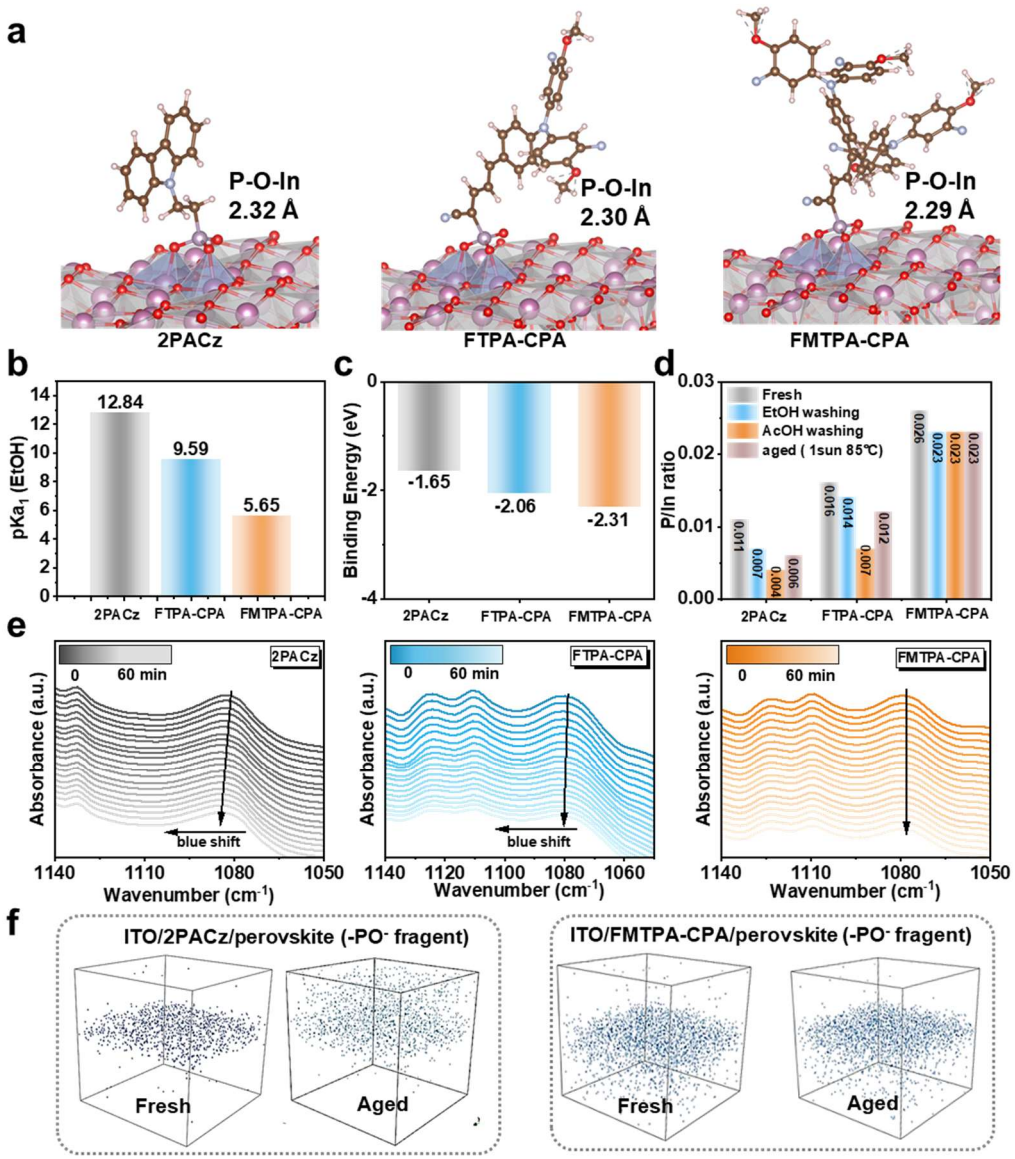

Fig. 2| Robust anchoring to substrate of D-A-D resonant SAM. a, DFT calculation of the anchoring binding energy of 2PACz, FTPA-CPA and FMTPA-CPA with ITO. The blue regions are the -P-O-In bonds in SAMs bonded with ITO. **b,** DFT simulations of the acid dissociation constant of phosphonic acid group on the 2PACz, FTPA-CPA and FMTPA-CPA. **c,** The binding energies of 2PACz, FTPA-CPA and FMTPA-CPA SAM on ITO substrate. **d,** The P/In ratio by XPS spectroscopy of 2PACz, FTPA-CPA and FMTPA-CPA on ITO substrate. **e,** *In-situ* FTIR spectra of the 2PACz, FTPA-CPA and FMTPA-CPA films with AcOH washing on ITO substrate at 85°C. **f,** The -PO^- signal intensity by ToF-SIMs of ITO/2PACz/perovskite and ITO/FMTPA-CPA/perovskite before and after aging under high-temperature and illumination.

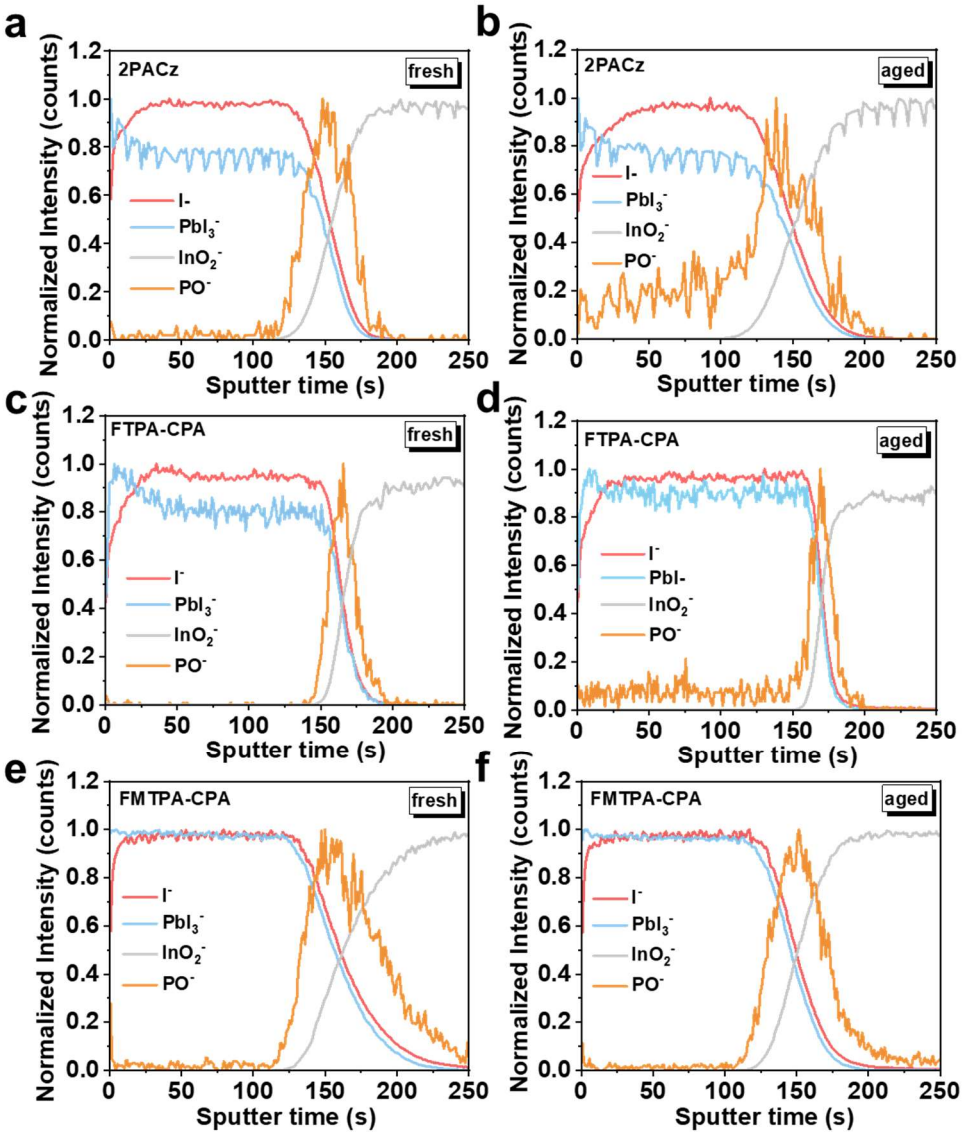

Fig. R40 (i.e., **Supplementary Fig. 22** in SI) ToF-SIMS depth profiles of 2PACz (a) before and (b) after aging under high temperature and illumination conditions; ToF-SIMS depth profiles of FTPA-CPA (c) before and (d) after aging under high temperature and illumination conditions; ToF-SIMS depth profiles of FMTPA-CPA (e) before and (f) after aging under high temperature and illumination conditions.

9. The use of XPS peak area ratios (P/In) to quantitatively compare SAM coverage across different molecules is highly problematic and a major weakness. XPS is semi-quantitative, and signals from ultrathin layers are prone to large errors, and the P signal intensity is not directly proportional to the number of molecules if their structures differ significantly. To substantiate the coverage and stability claims, the authors must employ more reliable quantitative measurements.

Response: Thanks for the reviewer's insightful comments. Initially, we refer to several previous reports that uses XPS to monitor the SAM desorption process (*Science*, 2024, 383, 1236; *Nature*, 2024, 628, 93; *Joule*, 2024, 8, 2123). To address the concern that "*XPS is semi-quantitative, and signals from ultrathin layers are prone to large errors,*

and the P signal intensity is not directly proportional to the number of molecules if their structures differ significantly", we refer to a recently reported *Science* paper (*Science*, 2025, 389, 195), to additionally conduct SECCM-TLCV measurement to quantitatively determine the assembly densities of the SAMs. The SECCM-TLCV measurement, which has high sensitivity and signal-to-noise ratio, facilitates accurate determinations of molecular assembly density. The detailed measurement method has been provided in Comment 2 of Reviewer #2. As shown in **Fig. R41** (i.e., **Supplementary Fig. 18** in SI), the assembly densities mapping reveal that 2PACz exhibits an uneven distribution with an average assembly density of 2.99×10^{-10} mol cm^{-2}. In contrast, FTPA-CPA displays enhanced uniformity, with an average assembly density of 3.95×10^{-10} mol cm^{-2}. Notably, resonant FMTPA-CPA shows the highest assembly density with 5.03×10^{-10} mol cm^{-2} and overall uniformity. These findings demonstrate that the D-A-D electronic resonance fundamentally reinforce the bond strength of the P-O-In anchoring, significantly suffering from molecular aggregation.

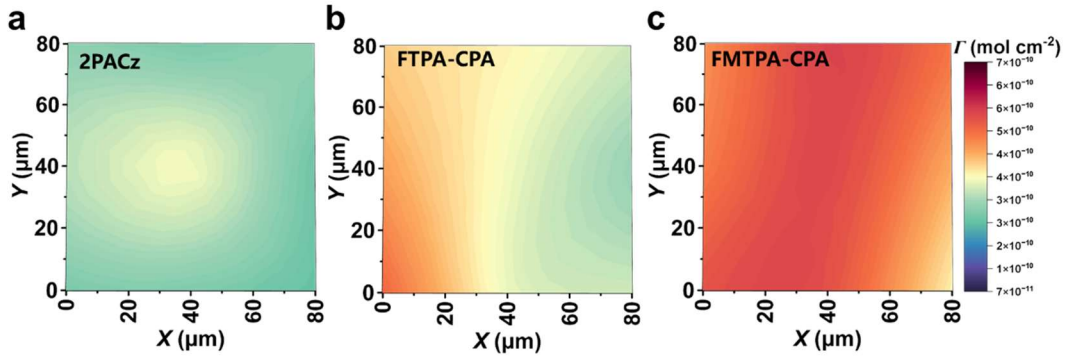

Fig. R41 (i.e., **Supplementary Fig. 18** in SI) Assembly densities mapping of (a) 2PACz, (b) FTPA-CPA and (c) FMTPA-CPA obtained from SECCM-TLCV.

The corresponding revisions for the revised Manuscript (marked red) are listed below:
Page 7 in the revised Manuscript: Furthermore, the scanning electrochemical cell microscopy-thin-layer cyclic voltammetry (SECCM-TLCV) measurement indicates the FMTPA-CPA sample possesses uniformly high molecular assembly density, and the anchored molecular density is well sustained even after AcOH washing (**Supplementary Fig. 18**).
Pages 8~9 in the revised Manuscript: AFM-IR and SECCM-TLCV measurement results also reflect the compact and homogeneous FMTPA-CPA coverage on the ITO substrate (**Supplementary Fig. 18 & Fig. 28**), which is even well sustained after thermal and illumination aging (**Supplementary Fig. 28**). The above analysis implies that FMTPA-CPA avoids suffering from molecular aggregation with the dedicated D-A-D electronic resonance design, thereby achieving an optimal balance between stability and large-area uniformity.

10. Supplementary Fig. 23 appears to show same images for different samples. This must be corrected immediately. In addition, the statement that perovskite on FMTPA-CPA shows higher XRD peak intensity requires quantification. The proposed reason (improved wettability leading to better crystallization) is plausible but should be supported by additional analysis.

Response: Thanks for the reviewer's careful comments.

We are very sorry for the mistake that *Supplementary Fig. 23 appears to show same images for different samples*. This figure presents the top surface morphology of perovskite films based on 2PACz, FTPA-CPA, and FMTPA-CPA. As we use antisolvent during the perovskite crystallization process, according to previous investigations, the perovskite films crystallize from the top surface to the bottom interface. Therefore, the top surfaces morphology based the three SAMs are nearly identical, making it prone to be misidentified (**Fig. R42** (i.e., **Supplementary Fig. 31** in SI) **& Fig. R43**). The surface morphology figure of FTPA-CPA was mistakenly inserted in the initial submission due to the similar surface morphology. We have immediately corrected this error in the revised manuscript, as shown in **Fig. R42** (i.e., **Supplementary Fig. 31** in SI, previously Supplementary Fig. 23).

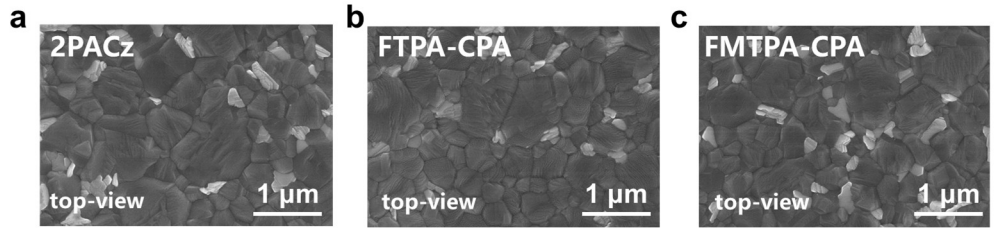

Fig. R42 (i.e., **Supplementary Fig. 31** in SI) Top-view SEM images of perovskite films deposited on (a) 2PACz, (b) FTPA-CPA and (c) FMTPA-CPA SAMs. Scale bar: 1 μm.

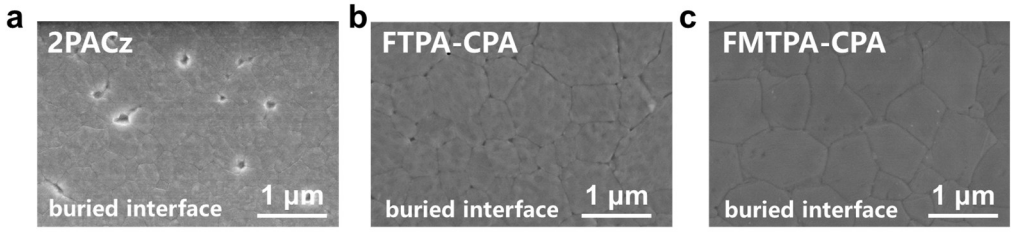

Fig. R43 SEM images of the buried interface of perovskite films deposited on (a) 2PACz, (b) FTPA-CPA and (c) FMTPA-CPA. Scale bar: 1 μm.

For the comment that "*In addition, the statement that perovskite on FMTPA-CPA shows higher XRD peak intensity requires quantification.*". The perovskite films crystallize from the top surface to the bottom interface during the antisolvent assisted perovskite crystallization process, resulting in the buried interface quality being largely dependent on the SAM characteristics. As shown in **Fig. R43**, the obvious nanovoids at the buried interface of the perovskite grown on 2PACz and FTPA-CPA can be observed, but compact and homogeneous perovskite buried morphology can be achieved on FMTPA-CPA. To quantify perovskite film quality on different SAMs, we further analyze peak intensity and full width at half maximum (FWHM) of (100) diffraction peak at 14.2°. The peak intensity of the (100) diffraction peak was examined, which possesses 2206.5, 2496.9, and 2929.2 for the perovskite films based on 2PACz, FTPA-CPA, and FMTPA-CPA, respectively. In addition, the (100) diffraction peak exhibited FWHMs of 0.11°, 0.10°, and 0.09°, for 2PACz, FTPA-CPA, and FMTPA-CPA, respectively. The intensity analyzes have been added in **Fig. R44** (i.e., **Supplementary Fig. 37** in SI).

These finding indicate that the buried perovskite interface based on the FMTPA-CPA possesses the excellent crystallization quality.

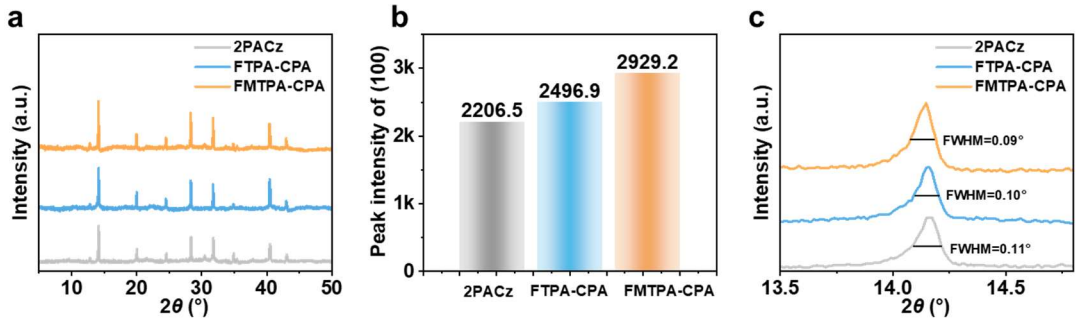

Fig. R44 (i.e., **Supplementary Fig. 37** in SI) (a) XRD of the buried interface of perovskite deposited on 2PACz, FTPA-CPA and FMTPA-CPA SAMs; (b) the intensity and (c) FWHM of (100) diffraction peak of buried perovskite interface based on 2PACz, FTPA-CPA, and FMTPA-CPA.

To address the concern that "*The proposed reason (improved wettability leading to better crystallization) is plausible*", additional analysis is provided. Specifically, during the deposition of perovskite active layers on organic SAM, the perovskite precursor solution typically employs strongly polar solvents (DMF and DMSO). There are several previous reports also claim that precursor solution exhibits improved wettability on organic materials possessing larger dipole moments (*Science*, 2023, 380, 404; *Nature*, 2025, 646, 95; *Angew. Chem. Int. Ed.*, 2025, 64, e202419608). Owing to the D-A-D resonance, FMTPA-CPA has the largest dipole moments of 10.5 D, which is nearly twice and four times greater than those observed in FTPA-CPA (3.6 D) and 2PACz (2.1 D) as shown in **Fig. 1b**, respectively. In addition, the polar terminated groups (-F and -OMe) present in the organic molecules can form weak chemical interactions with the perovskite precursor species, which consequently promote more uniform spreading as well as the ameliorated crystallization on the FMTPA-CPA. As shown in **Fig. R45** (i.e., **Supplementary Fig. 29** in SI), perovskite precursor solution has a much smaller contact angle (<4°) on FMTPA-CPA compared to that on 2PACz (27.07°) and FTPA-CPA (13.69°). The ameliorated wettability enables compact and full perovskite layer coverage on large-scale substrates (**Fig. R46** (i.e., **Supplementary Fig. 30** in SI)). These effects collectively lead to enhanced buried interface of perovskite film as shown in **Fig. R43**.

Fig. R45 (i.e., **Supplementary Fig. 29** in SI) Contact angels of the perovskite precursor solution on the 2PACz, FTPA-CPA and FMTPA-CPA SAMs.

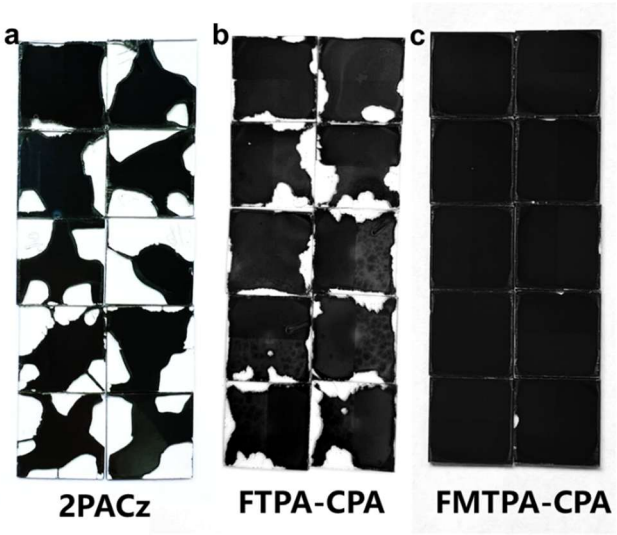

Fig. R46 (i.e., **Supplementary Fig. 30** in SI) Photographs of perovskite films deposited on (a) 2PACz, (b) FTPA-CPA and (c) FMTPA-CPA SAMs.

We have revised the corresponding contents to better discuss effect of wettability on perovskite crystallization in the revised Manuscript (marked red).

Page 9 in the revised Manuscript: In addition to the improved coverage and uniformity, the FMTPA-CPA exhibits superwetting characteristics regard to perovskite precursor solution due to the polar terminated groups (-F and -OMe). This promotes more uniform spreading as well as the ameliorated crystallization on FMTPA-CPA and thus leads to high-quality perovskite. As shown in **Supplementary Fig. 29**, perovskite precursor solution has a much smaller contact angle (<4°) on the FMTPA-CPA SAM compared to that on 2PACz (27.07°) and FTPA-CPA (13.69°).

Page 9 in the revised Manuscript: The improved perovskite film quality grown on FMTPA-CPA compared with FTPA-CPA and 2PACz can be further validated by higher intensity and smaller full width at half maximum (FWHM) of diffraction peaks in grazing-incidence wide-angle X-ray scattering (GIWAXS), X-ray diffraction (XRD) and photoluminescence (PL) mapping (**Supplementary Figs. 36-41**)

11. The similar PLQY of perovskite on FMTPA-CPA and on bare glass (Fig. 3e) is unusual. Glass/perovskite interfaces are typically highly defective, leading to low PLQY. Therefore, the result requires explanation. Full PLQY spectra and detailed experimental conditions (excitation wavelength, power density, integration sphere calibration procedure) should be provided. The TRPL decays (Fig. 3f) also look unusual, particularly the very long tail for FMTPA-CPA. The test conditions (excitation wavelength, fluence, repetition rate) are mandatory for interpretation. The decays should be measured under identical conditions for all samples. The TRPL of glass/perovskite sample should be provided. The reported SRH lifetimes should be extracted from a proper recombination model with a detailed discussion.

Response: Thanks for the reviewer's comments. We response to this comment with the following three parts.

For the comment that "*Glass/perovskite interfaces are typically highly defective,*

leading to low PLQY", we find clean and defective-less glass substrate can also lead to high photoluminescence quantum yield (PLQY). Firstly, the Glass substrates were thoroughly cleaned with acetone and isopropanol and subsequently treated by ultraviolet-ozone prior to perovskite deposition. This process removes organic residues and increases surface hydrophilicity, yielding an exceptionally clean surface. As a result, the clean surface and high wettability promote uniform nucleation and compact film formation on glass, which contributes to the higher PLQY of the perovskite layer. In addition, since glass is an inert insulator without SAM, no interfacial charge extraction occurs, minimizing carrier quenching at the interface. Combining these two points, the perovskite layers formed on cleaned Glass substrates exhibit relatively high PLQY values, compared to 2PACz/perovskite and FTPA-CPA/perovskite films (*Nature*, 2024, 632, 536; *Nature*, 2023, 618, 80; *Energy Environ. Sci.*, 2019, 12, 2778-2788; *Adv. Funct. Mater.*, 2022, 32, 2209563).

To follow the reviewer's suggestion, we provide the detailed experimental conditions of PLQY measurements here. **Fig. R47** (i.e., **Supplementary Fig. 42** in SI) is complete PLQY spectra. The excitation wavelength was set as 405 nm (the spectral integration was performed over the wavelength range of 390-420 nm), and power density was 100 mW/cm^2 (one standard sun light).

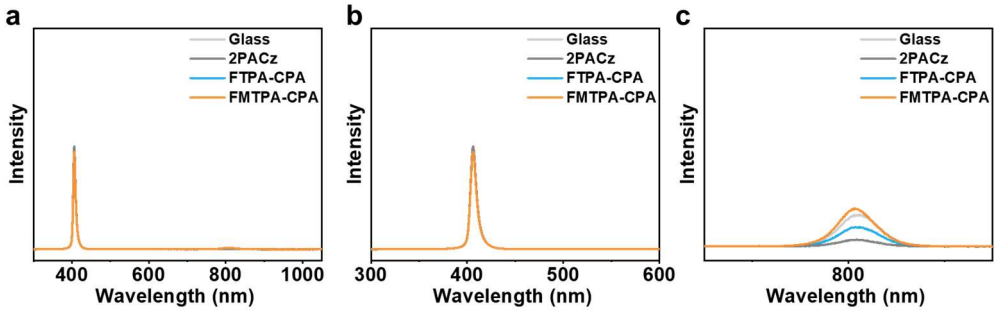

Fig. R47 (i.e., Supplementary Fig. 42 in SI) The complete PLQY spectra of perovskite films on 2PACz, FTPA-CPA and FMTPA-CPA SAMs.

For the comment that "*integration sphere calibration procedure should be provided*", the calibration process is integrated into the instrument system. The detailed procedure is described as follows:

1) Spectral response calibration: A pre-calibrated standard calibration light source (by the Suzhou Research Institute as shown in **Fig. R48**) was measured within the integrating sphere system. The recorded detector signals were compared with the theoretical emission spectrum to determine the instrument response curve and calibration factor, which was subsequently applied to all sample measurements.
2) Integrating-sphere reflectance and geometric calibration: Corrections for excitation-light incidence angle, sample positioning, and port size are made based on measurements of a reference sample such as a Spectral on plate, which defines the integrating-sphere collection efficiency.
3) Excitation-light intensity calibration: The excitation power is calibrated using a power meter or an energy meter to measure the absolute intensity of the incident

light reaching the sphere. This ensures accurate determination of the number of absorbed photons when calculating excitation energies.

4) Dark-noise and background calibration: The background signal of the empty sphere (without sample) is recorded to subtract the detector's dark current and stray-light contributions from subsequent measurements.

5) PLQY measurement after calibration: After completing the calibration routines, PLQY measurements are performed by first recording the intensity of incident light inside the integrating sphere without a sample (excitation reference), and then measuring both the excitation and emission signals after the sample is introduced. The number of absorbed and emitted photons is calculated to determine the PLQY.

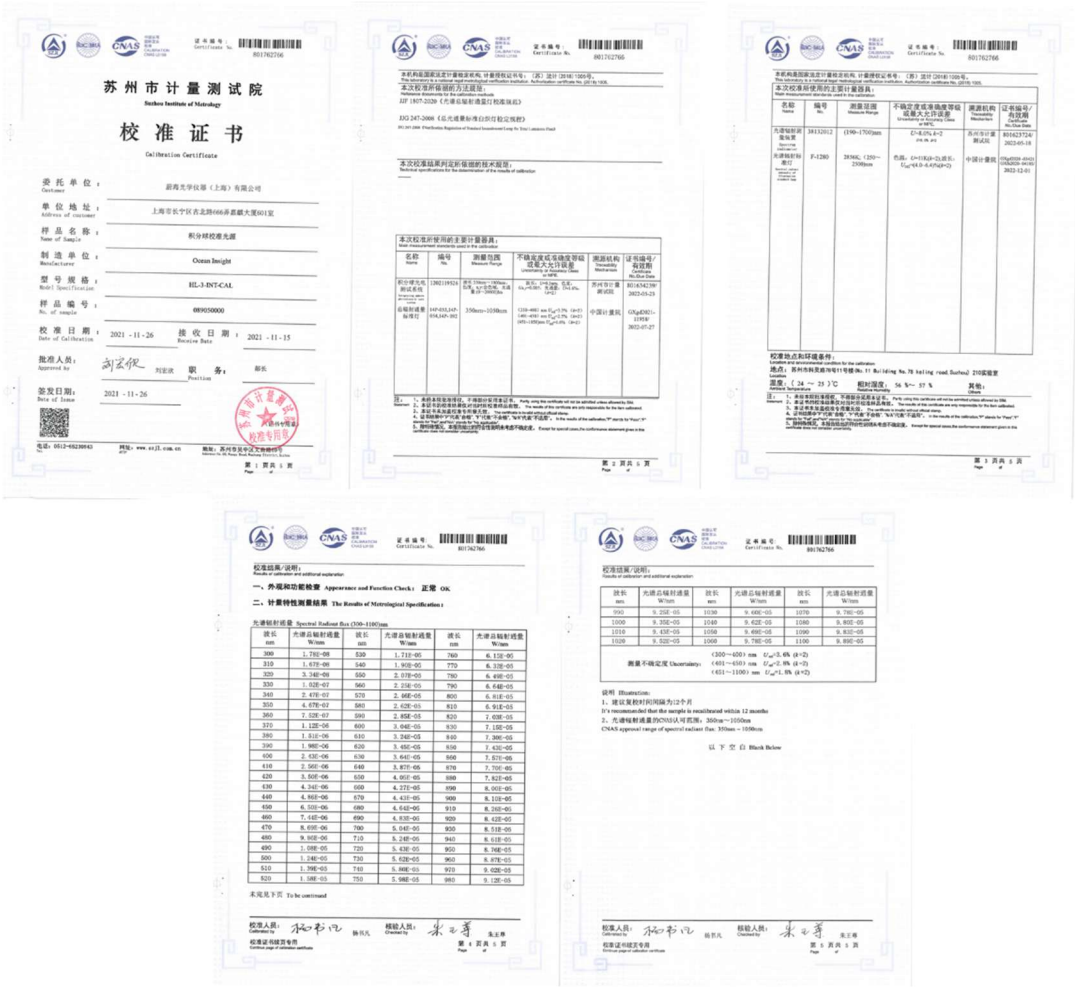

Fig. R48 The calibration certificate of PLQY light source by the Suzhou Research Institute.

The corresponding revisions for the revised manuscript and the revised Supplementary Information (marked red) are listed below:

Pages 8~9 in the revised Supplementary Information:

Photoluminescence Quantum Yield (PLQY) measurements. PLQY results were acquired using a SPECTRUMTEO-EOY-EL from Ocean Optics, inc. The excitation wavelength was set between 405 nm (the spectral integration was performed over the

wavelength range of 390-420 nm), and power density was 100 mW/cm^2. The calibration process is integrated into the instrument system. Spectral response calibration: A pre-calibrated standard calibration light source was measured within the integrating sphere system. The recorded detector signals were compared with the theoretical emission spectrum to determine the instrument response curve and calibration factor, which was subsequently applied to all sample measurements. The detailed procedure is described as follows: Integrating-sphere reflectance and geometric calibration: Corrections for excitation-light incidence angle, sample positioning, and port size are made based on measurements of a reference sample such as a Spectral on plate, which defines the integrating-sphere collection efficiency. Excitation-light intensity calibration: The excitation power is calibrated using a power meter or an energy meter to measure the absolute intensity of the incident light reaching the sphere. This ensures accurate determination of the number of absorbed photons when calculating excitation energies. Dark-noise and background calibration: The background signal of the empty sphere (without sample) is recorded to subtract the detector's dark current and stray-light contributions from subsequent measurements. PLQY measurement after calibration: After completing the calibration routines, PLQY measurements are performed by first recording the intensity of incident light inside the integrating sphere without a sample (excitation reference), and then measuring both the excitation and emission signals after the sample is introduced. The number of absorbed and emitted photons is calculated to determine the PLQY.

To address the concerns related to time-resolved photoluminescence (TRPL) results, we first provide the detailed experimental conditions of TRPL measurements here. The TRPL measurements were performed under identical conditions for all samples using a 454 nm pulsed excitation (fluence ≈ 2.25 mW cm^{-2}, repetition rate = 40 kHz). The emission was collected through the same optical path and detector settings, ensuring that the decay curves are directly comparable.

At last, we follow the suggestions that *"The decays should be measured under identical conditions for all samples. The TRPL of glass/perovskite sample should be provided. The reported SRH lifetimes should be extracted from a proper recombination model with a detailed discussion"*.

The TRPL decay curves of all perovskite film samples were fitted using a bi-exponential function:

$$I(t) = f_1 e^{-\frac{t}{\tau_1}} + f_2 e^{-\frac{t}{\tau_2}}$$

where f_1 and τ_1 represent the fast decay component, typically associated with surface-trap-assisted Shockley-Read-Hall (SRH) recombination, and f_2 and τ_2 correspond to the slow component, which originates from bulk radiative recombination or long-lifetime carrier diffusion. The 2PACz/perovskite sample exhibits the shortest average charge-carrier lifetime, indicating pronounced non-radiative recombination and a high density of interfacial defects at the buried interface, resulting in a fast recombination rate. The FTPA-CPA/perovskite sample shows a comparatively longer

carrier lifetime, suggesting significant improvement in interfacial passivation and a moderate enhancement of carrier lifetime. The FMTPA-CPA/perovskite sample possesses the longest average carrier lifetime, with the largest fraction of the slow component τ_2. This indicates that radiative recombination dominates the decay process and that buried-interfacial recombination has been effectively suppressed. As shown in **Fig. R49**, the Glass/perovskite sample exhibits $\tau_{avg} \approx 2.12$ μs, slightly shorter than FMTPA-CPA (≈ 4.1 μs), confirming its inert but less passivating interface.

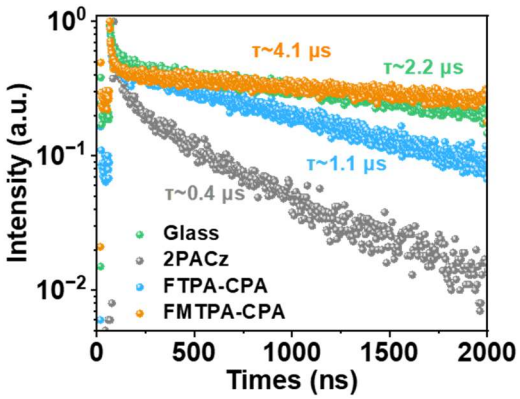

Fig. R49 Photoluminescence decays of perovskite films on 2PACz, FTPA-CPA and FMTPA-CPA SAMs using a 454 nm pulsed excitation at 2.25 mW cm^{-2} excitation fluence.

As shown in **Fig. 3d** (original **Fig. 3f**), the initially observed long-lived component for FMTPA-CPA mainly arises from the **relatively low excitation fluence** used in the measurement. At low excitation power, the photogenerated carrier concentration is relatively low, and the TRPL decay consists of two stages: an initial fast component dominated by surface recombination, followed by a much slower tail corresponding to bulk recombination. Upon increasing the excitation fluence (up to 14-350 mW cm^{-2}) consistent with recent observations reported in *Science* (*Science*, 2025, 389, 195)**,** both surface and bulk traps gradually become saturated, and the overall decay accelerates (**Fig. R50** (i.e., **Supplementary Fig. 43** in SI)), confirming the intensity-dependent transition from surface trap-limited recombination to bulk bimolecular recombination dynamics. Therefore, the apparent long tail for FMTPA-CPA reflects the combined effect of fast surface recombination at the beginning and slow bulk recombination at later times, amplified by the low-fluence regime.

In summary, all TRPL experiments were conducted under controlled and identical conditions, and the fluence-dependent measurements further confirm that the long tail observed for FMTPA-CPA is physically meaningful, originating from the combination effects of highly efficient buried-interface passivation and the lower carrier density under weak excitation. Therefore, the observed decay behavior is both reproducible and physically consistent across all experimental configurations. **To ensure accuracy, we have revised the TRPL decays under identical excitation intensity of 14.25 mW cm^{-2} in Fig. 3d** (original **Fig. 3f).**

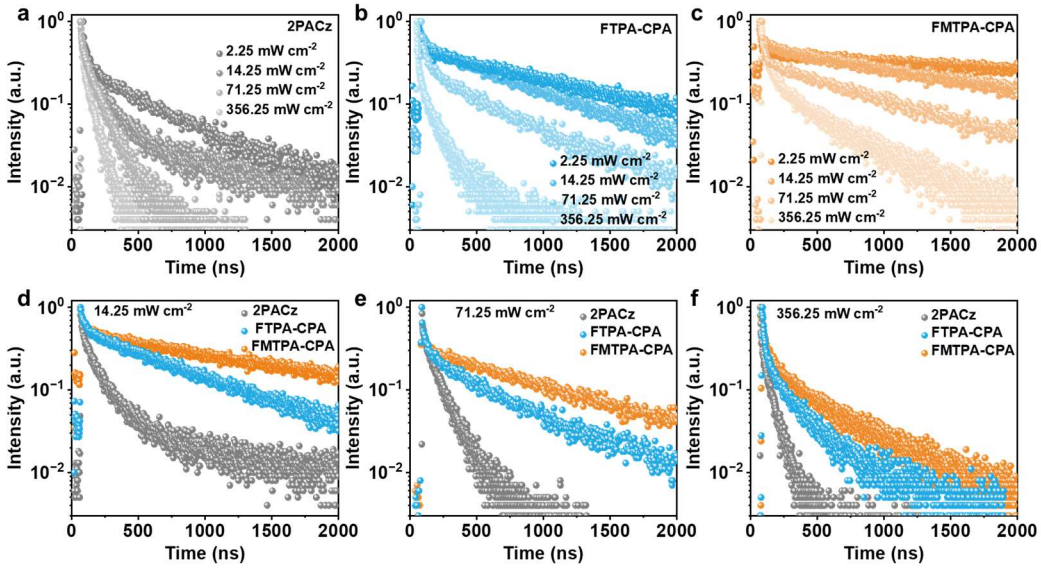

Fig. R50 (i.e., **Supplementary Fig. 43** in SI) Excitation intensity-dependent photoluminescence decays of perovskite films on (a) 2PACz, (b) FTPA-CPA and (c) FMTPA-CPA SAMs using a 454 nm pulsed excitation. Comparison of the decay curves under identical excitation intensities of (d) 14.25 mW cm^{-2}, (e) 71.25 mW cm^{-2}, (f) 356.25 mW cm^{-2}.

The corresponding revisions for the revised manuscript and the revised Supplementary Information (marked red) are listed below:

Pages 9~10 in the revised manuscript: In addition, the time-resolved photoluminescence (TRPL) results reveal that the Shockley-Read-Hall lifetime of perovskite film on FMMPA-CPA is around 1.2 μs, which is much longer than those on FTPA-CPA and 2PACz. This trend can be also observed under several different excitation intensities (**Fig. 3d** & **Supplementary Fig. 43** & **Supplementary Table 10**), implying interfacial nonradiative recombination has been effectively suppressed by developing super-amphiphilic, uniform and compact FMTPA-CPA.

Page 6 in the revised Supplementary Information:

TRPL measurements was tested by an FLS980 (Edinburgh Instrument, UK) and the excitation wavelength was set between 454 nm.

Table R15 (i.e., **Supplementary Table 10** in SI) TRPL decay fitting parameters of perovskite deposited on 2PACz, FTPA-CPA, FMTPA-CPA under excitation intensities of 14.25 mW cm^{-2}.

SAMs	τ_1 (ns)	f_1 (%)	τ_2 (ns)	f_2 (%)	τ_{avg} (ns)
2PACz	24.709	25.625	73.496	74.496	68.439
FTPA-CPA	31.139	4.001	688.884	95.999	687.647
FMTPA-CPA	33.375	2.204	1171.241	97.796	1170.575

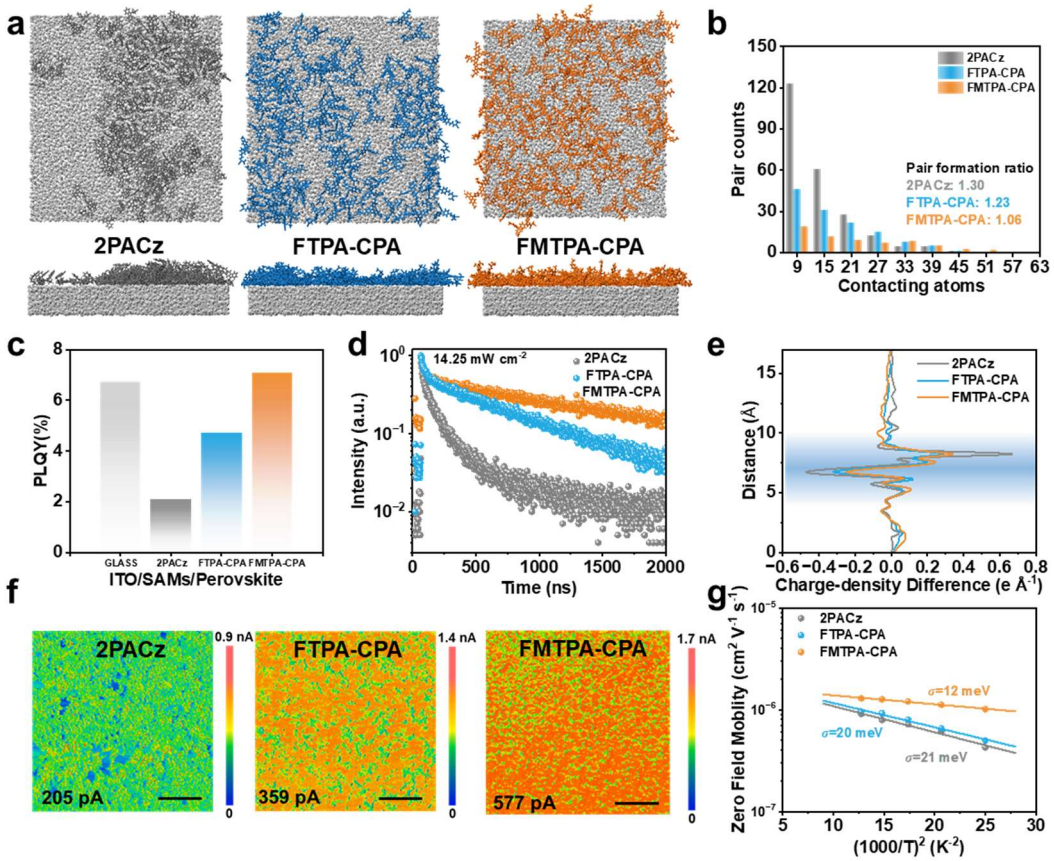

Fig. 3| Compact, homogeneous D-A-D resonant SAM and resulting high quality perovskite film. a, Top views and side views of equilibrated molecular representations of 2PACz, FTPA-CPA and FMTPA-CPA systems in MD simulations. **b,** MD simulated equilibrated snapshots and counts of dimer clusters for 2PACz, FTPA-CPA and FMTPA-CPA. **c,** PLQY of perovskite films on 2PACz, FTPA-CPA and FMTPA-CPA SAMs. **d,** Photoluminescence decays of perovskite films on 2PACz, FTPA-CPA and FMTPA-CPA SAMs. **e,** Calculated charge-density difference along the vertical direction to the ITO surface. **f,** C-AFM images of the 2PACz, FTPA-CPA and FMTPA-CPA (the scale bars represent 1 μm). **g,** Hole mobilities of the 2PACz, FTPA-CPA and FMTPA-CPA films as a function of $1/T^2$ were obtained using the equation for GDM.

12. The energy level diagram appears inconsistent with the UPS data (Fig. S35), please check again. In addition, UPS shows 2PACz has the largest work function, which should be more favorable for hole extraction in a p-i-n structure, contradicting the narrative that FMTPA-CPA is superior. The HOMO level of FMTPA-CPA does not appear deeper than FTPA-CPA of 2PACz from the UPS secondary electron cut-off and valence band region. The depicted energy level diagram (likely Fig. S35e) needs to be precisely derived from the UPS measurements (work function = 21.22 eV - Ecutoff; HOMO onset relative to Fermi level). A corrected, quantitatively accurate diagram is essential. The authors must reconcile these observations: if FMTPA-CPA has a less favorable work function, what other factor compensates to yield better device performance?

Response: Thanks for the reviewer's comments. **We draw the energy level diagram**

by aligning the Fermi level (E_F) instead of the Vacuum level of different layers. The UPS characterization was performed on the ITO/SAM heterostructures, rather than on the pure SAM molecules. Therefore, the measured energy levels can be attributed to the interfacial electric field effect that arises when the SAM is covalently anchored onto the ITO surface. Specifically, SAMs anchored onto the ITO substrate through covalent bonding leads to local variations in electrostatic potential. This potential difference manifests, at the band level, as shifts in the HOMO and work function (W_F) of the ITO/SAM. The resulting band bending and energy level alignment tend to drive the Fermi-levels of both components toward equilibrium, analogous to the built-in electric field within a conventional semiconductor p-n junction, which is also confirmed in some previously reported works (*Science*, 2023, 380, 404; *Science*, 2024, 383, 1236; *Nature*, 2024, 632, 301). As suggested, we revised the illustration figure to show this interfacial band alignment more clearly as shown in **Fig. R51** (i.e., **Supplementary Fig. 45** in SI, original **Supplementary Fig. 35**).

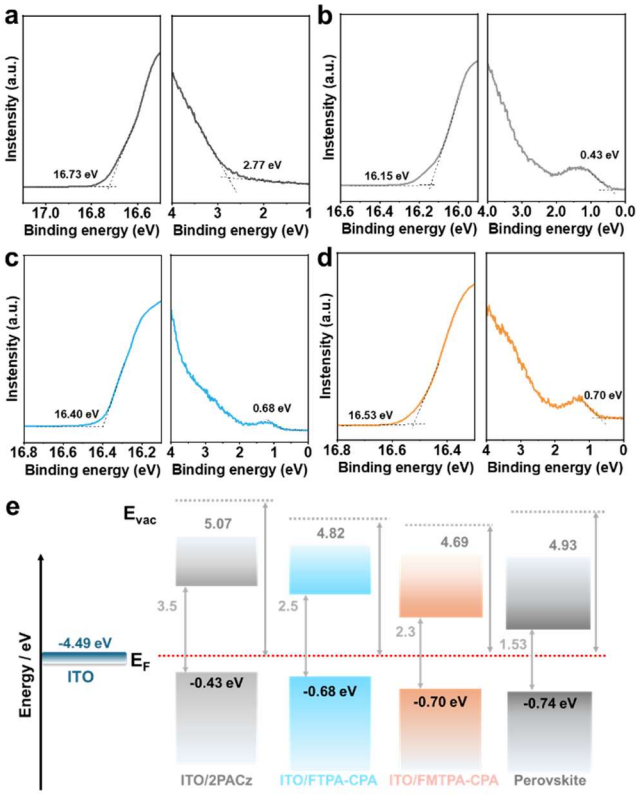

Fig. R51 (i.e., **Supplementary Fig. 45** in SI) UPS cut-off edge of (a) Glass/ITO, (b) ITO/2PACz, (c) ITO/FTPA-CPA and (d) ITO/FMTPA-CPA; (e) Schematic illustration of energy level diagram (aligned with the Fermi-level).

As shown in **Fig. R51** (i.e., **Supplementary Fig. 45** in SI), although the absolute work function of FMTPA-CPA is slightly lower than that of 2PACz/ITO, the HOMO of FMTPA-CPA aligns more favorably with the valence band maximum (VBM) of the perovskite layer after the Fermi-level alignment. This favorable energy level alignment minimizes interfacial energetic offsets and facilitates more efficient charge extraction and reduced interfacial recombination.

13. The origin of the different temperature dependencies of hole conductivity (Fig. 3g, S36) is not explained. Why does 2PACz show the strongest temperature dependence? Is it due to higher energetic disorder as mentioned? If so, how does the resonant structure of FMTPA-CPA reduce this disorder? The authors should discuss this in the context of molecular packing and electronic coupling. Furthermore, if FTPA-CPA and FMTPA-CPA possess radical character, their charge transport might involve hopping between localized states, which also has a temperature dependence. The authors should elaborate on the proposed transport mechanism in their systems.

Response: Thanks for the reviewer's professional comments. The strongest temperature dependence of 2PACz was attributed to high energetic disorder and inhomogeneous surface coverage. In contrast, FMTPA-CPA with uniform, ordered molecular arrangement as well as smallest reorganization energy has weaker temperature dependence of hole hopping. We reply to these comments point to point as below:

For the comment "*The authors should discuss this in the context of molecular packing and electronic coupling.*" For 2PACz, the strong π-π interactions between the carbazole cores lead to large binding energies in dimer formation and highly disordered aggregation. The calculated static energetic disorder is the highest among the studied molecules (0.297 eV, **Fig. R52** (i.e., **Supplementary Fig. 47** in SI)), and AFM-IR together with SECCM-TLCV results confirm its inhomogeneous surface coverage (**Supplementary Fig. 18 & Fig. 28**). In addition, MD-DFT simulations indicate locally strong intermolecular electronic coupling within aggregated dimers but negligible coupling in uncovered regions (**Fig. R53** (i.e., **Supplementary Fig. 48** in SI)). This spatially heterogeneous coupling interrupts charge-transport continuity; despite locally favorable interaction, the overall charge-transport connectivity remains limited. Consequently, 2PACz exhibits the strongest temperature dependence of hole conductivity due to its high energetic disorder.

In contrast, the D-A-D electronic resonance FMTPA-CPA enhances anchoring strength, indicating an extremely weak tendency to aggregate. The energetic disorder is the lowest (0.190 eV, **Fig. R52** (i.e., **Supplementary Fig. 47** in SI)), and AFM-IR and SECCM-TLCV confirm the compact and homogeneous coverage across the ITO substrate as shown in **Fig. 3c & Supplementary Fig. 18 & Fig. 28**. Consequently, the electronic resonance FMTPA-CPA shows uniform and ordered molecular arrangement, thus exhibiting the weakest temperature dependence of hole conductivity. MD-DFT results also reveal that although FMTPA-CPA possesses moderate intermolecular coupling in **Fig. R52** (i.e., **Supplementary Fig. 47** in SI), its uniform molecular arrangement enables well-connected transport pathways, minimizing trap formation and maintaining efficient hole conduction. This combination of homogeneous packing and sufficient coupling ensures efficient hole conductivity and weaker temperature dependence.

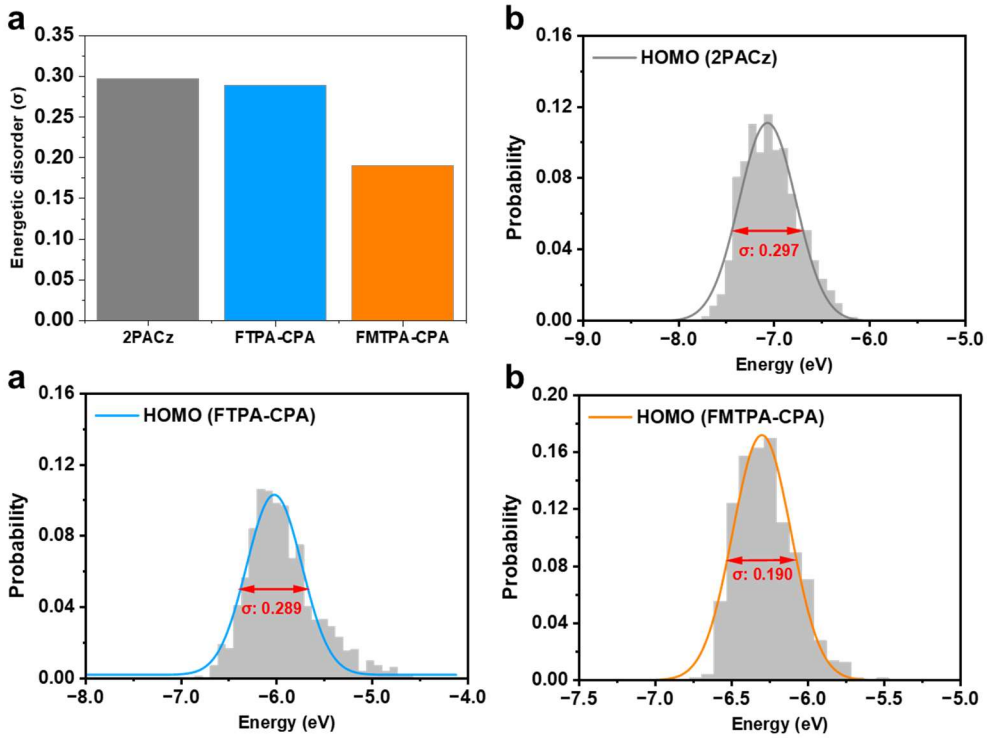

Fig. R52 (i.e., **Supplementary Fig. 47** in SI) (a) The fitted energetic disorder values for 2PACz, FTPA-CPA and FMTPA-CPA by MD-DFT simulation; (b) The probability distributions of HOMO energies, and the Gauss-fitted energetic disorder (σ) values for (b) 2PACz, (c) FTPA-CPA and (d) FMTPA-CPA by MD-DFT calculations.

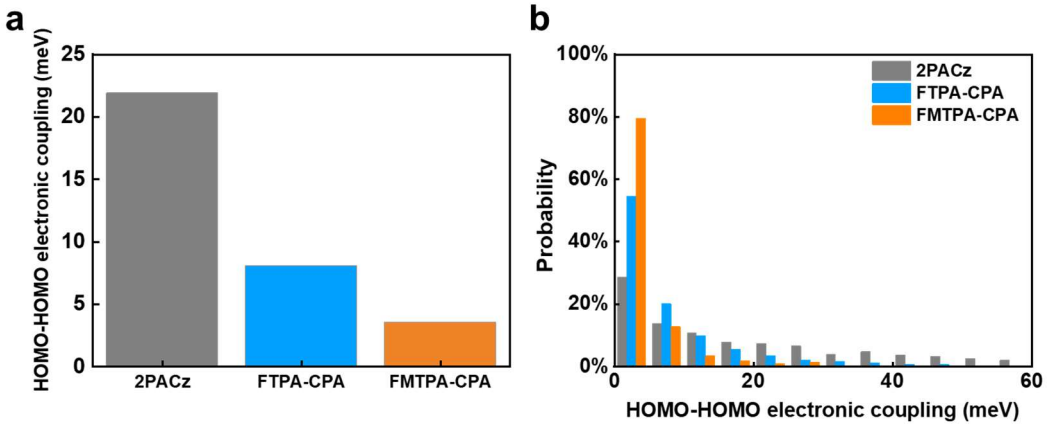

Fig. R53 (i.e., **Supplementary Fig. 48** in SI) (a) Statistically averaged HOMO-HOMO electronic coupling values for dimers extracted from MD simulations and (b) probability distribution of HOMO-HOMO electronic coupling estimated by MD-DFT calculations for 2PACz, FTPA-CPA and FMTPA-CPA.

For the comment "*The authors should elaborate on the proposed transport mechanism in their systems.*". In addition to static energetic disorder and intermolecular electronic coupling, temperature dependence of electronic conductivity also strongly depends on the extent of intramolecular dynamic energetic disorder quantified by intramolecular structural reorganization energy (see *Chem. Rev.*, 2007, 107, 4, 926). Here, we

calculated the intramolecular structural reorganization energies (λ) of FTPA-CPA and FMTPA-CPA for hole transport, 0.33 and 0.17 eV, respectively. Much larger λ values and static energetic disorder (σ) values than intermolecular electronic coupling values (see **Fig. R52** (i.e., **Supplementary Fig. 47** in SI)) lead to localized hole-transport states, which has been well known in charge-transport research filed (see *Chem. Rev.*, 2007, 107, 4, 926). In such cases, charge transport predominantly proceeds through thermally activated hopping between these localized states, which can usually be described in the framework of Marcus electron-transfer theory. At low temperatures, the hopping rate is suppressed because carriers lack sufficient energy to overcome the potential barriers between neighboring localized states, leading to reduced conductivity. As the temperature increases, thermal activation facilitates more frequent hops, resulting in enhanced hole conductivity (*Chem. Rev.*, 2007, 107, 4, 926). Therefore, the thermally activated temperature dependences observed for FTPA-CPA and FMTPA-CPA are consistent with a hopping-type transport mechanism associated with localized charge-transport states.

As shown by the results of our ESR measurements and DFT calculations, FTPA-CPA and FMTPA-CPA possess radical character to some extent. Importantly, the electronic resonance in FMTPA-CPA not only gives rise to a stronger radical character, but also leads to the HOMO delocalization on the two donor moieties. Therefore, the λ value of FMTPA-CPA is significantly reduced compared to that of FTPA-CPA. As shown in **Fig. R53** (i.e., **Supplementary Fig. 48** in SI), FTPA-CPA, exhibiting higher dynamic energetic disorder (due to a larger reorganization energy of 0.33 eV, **Fig. R54** (i.e., **Supplementary Fig. 49** in SI)), possesses more localized states and thus higher activation barriers for charge hopping. Consequently, the conduction in FTPA-CPA is more thermally activated, showing stronger temperature dependence. In contrast, FMTPA-CPA has a smaller reorganization energy (0.17 eV, **Fig. R54** (i.e., **Supplementary Fig. 49** in SI)) and a much narrower energetic distribution due to its homogeneous, stable molecular arrangement. Although its transport still follows a hopping mechanism, the uniform arrangement reduces trapping and energy barrier, enabling efficient hopping even at lower temperatures. As a result, FMTPA-CPA exhibits weaker temperature dependence of hole conductivity.

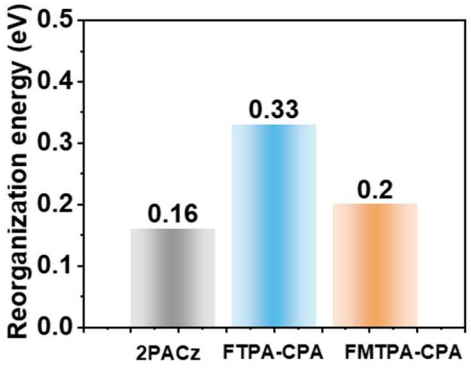

Fig. R54 (i.e., **Supplementary Fig. 49** in SI) The reorganization energies of 2PACz, FTPA-CPA and FMTPA-CPA.

We added the discussion of transport mechanism in the revised Supplementary Information (marked red) are listed below:

Pages 15~17 in the revised Supplementary Information:

Supplementary Note 8. The energetic disorders and analysis of dynamic energetic disorder

For 2PACz, the strong π-π interactions between the carbazole cores lead to large binding energies in dimer formation and highly disordered aggregation. The calculated static energetic disorder is the highest among the studied molecules (0.297 eV, **Supplementary Fig. 47**), and AFM-IR together with SECCM-TLCV results confirm its inhomogeneous surface coverage (**Supplementary Fig. 18 & 28**). In addition, MD-DFT simulations indicate locally strong intermolecular electronic coupling within aggregated dimers but negligible coupling in uncovered regions (**Supplementary Fig. 48**). This spatially heterogeneous coupling interrupts charge-transport continuity; despite locally favorable interaction, the overall charge-transport connectivity remains limited. Consequently, 2PACz exhibits the strongest temperature dependence of hole conductivity due to its high energetic disorder.

In contrast, the D-A-D electronic resonance FMTPA-CPA enhances anchoring strength, indicating an extremely weak tendency to aggregate. The energetic disorder is the lowest (0.190 eV, **Supplementary Fig. 47**), and AFM-IR and SECCM-TLCV confirm the compact and homogeneous coverage across the ITO substrate as shown in **Fig. 3c & Supplementary Fig. 18 & Fig. 28**. Consequently, the electronic resonance FMTPA-CPA shows uniform and ordered molecular arrangement, thus exhibiting the weakest temperature dependence of hole conductivity. MD-DFT results also reveal that although FMTPA-CPA possesses moderate intermolecular coupling in **Supplementary Fig. 47**, its uniform molecular arrangement enables well-connected transport pathways, minimizing trap formation and maintaining efficient hole conduction. This combination of homogeneous packing and sufficient coupling ensures efficient hole conductivity and weaker temperature dependence.

In addition to static energetic disorder and intermolecular electronic coupling, temperature dependence of electronic conductivity also strongly depends on the extent of intramolecular dynamic energetic disorder quantified by intramolecular structural reorganization energy.[25] Here, we calculated the intramolecular structural reorganization energies (λ) of FTPA-CPA and FMTPA-CPA for hole transport, 0.33 and 0.17 eV, respectively. Much larger λ values and static energetic disorder (σ) values than intermolecular electronic coupling values (see **Supplementary Fig. 47**) lead to localized hole-transport states, which has been well known in charge-transport research filed.[25] In such cases, charge transport predominantly proceeds through thermally activated hopping between these localized states, which can usually be described in the framework of Marcus electron-transfer theory. At low temperatures, the hopping rate is suppressed because carriers lack sufficient energy to overcome the potential barriers between neighboring localized states, leading to reduced conductivity. As the temperature increases, thermal activation facilitates more frequent hops, resulting in enhanced hole conductivity.[25] Therefore, the thermally activated temperature

dependences observed for FTPA-CPA and FMTPA-CPA are consistent with a hopping-type transport mechanism associated with localized charge-transport states.

As shown by the results of our ESR measurements and DFT calculations, FTPA-CPA and FMTPA-CPA possess radical character to some extent. Importantly, the electronic resonance in FMTPA-CPA not only gives rise to a stronger radical character, but also leads to the HOMO delocalization on the two donor moieties. Therefore, the λ value of FMTPA-CPA is significantly reduced compared to that of FTPA-CPA. As shown in **Supplementary Fig. 48**, FTPA-CPA, exhibiting higher dynamic energetic disorder (due to a larger reorganization energy of 0.33 eV, **Supplementary Fig. 49**), possesses more localized states and thus higher activation barriers for charge hopping. Consequently, the conduction in FTPA-CPA is more thermally activated, showing stronger temperature dependence. In contrast, FMTPA-CPA has a smaller reorganization energy (0.17 eV, **Supplementary Fig. 49**) and a much narrower energetic distribution due to its homogeneous, stable molecular arrangement. Although its transport still follows a hopping mechanism, the uniform arrangement reduces trapping and energy barrier, enabling efficient hopping even at lower temperatures. As a result, FMTPA-CPA exhibits weaker temperature dependence of hole conductivity.

14. UV light is known to degrade the interfaces. The UV illumination stability of devices, operational stability under a xenon lamp with UV region are necessary, which will provide critical information on photochemical stability. Additionally, the initial PCE values for all devices subjected to stability tests must be provided to allow readers to assess the starting point.

Response: Thanks for the reviewer's valuable comments. We totally agree with that "*UV light is the primary cause of degrade the interfaces*". To address this concern, we performed the stability measurements under UV light (365 nm, 56 mW cm^{-2}) illumination in a N_2 glovebox, and operational stability under a xenon lamp with UV region (metal halide (MH, 4.4% UV inside)).

As noted earlier (Response to Comment 1 of Reviewer#2) in **Fig. R10** (i.e., **Supplementary Fig. 58** in SI), the FMTPA-CPA-based device can maintain ~81% of their initial efficiency after 1,080 h under UV illumination (365 nm, 56 mW cm^{-2}), whereas only 62% and 43% of the initial efficiency is retained for FTPA-CPA and 2PACz-based devices after 700 h. These results clearly demonstrate that FMTPA-CPA forms a much more robust interfacial bond with ITO against UV-induced bond cleavage. Importantly, **Table R4** (i.e., **Supplementary Table 16** in SI) suggest that the UV stability of our devices maintain relatively improved UV stability compared with recently reported perovskite solar cells tested under similar UV stress conditions. This comparative analysis highlights the outstanding long-term UV tolerance achieved through the resonant FMTPA-CPA molecular design.

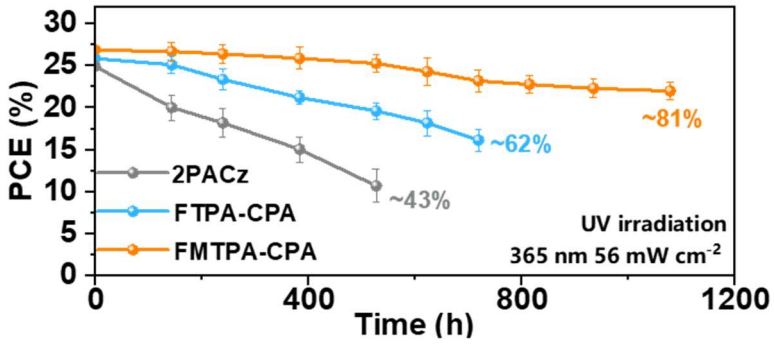

Fig. R10 (i.e., **Supplementary Fig. 58** in SI) The UV irradiation stability at 365 nm (56 mW cm^{-2}) of small-area devices based on 2PACz, FTPA-CPA and FMTPA-CPA.

Table R4 (i.e., **Supplementary Table 16** in SI) Statistical of the UV irradiation stability in references.

Ref.	Initial PCE	Power (mW cm^{-2})	Time (h)	PCE decay
This work	26.84%	56.0	1080	81%
Nature, 2023, 623, 313	25.5%	0.1	1100	95%
Sci. Adv., 2025, 11, eadu3493	26.0%	17.0	500	80%
Joule, 2024, 8, 11, 3142	26.32%	--	110	90%
Adv. Energy Mater., 2025, 15, 2501296	24.68%	50	130	80%
Adv. Funct. Mater., 2024, 34, 2400474	24.73%	50	380	90%
Chem. Eng. J., 2024, 497, 154552	22.46%	50	250	91%

In addition, as suggested by the reviewer, we evaluated device stability under a combined environment of UV-inclusive light as shown in **Fig. R55** (i.e., **Supplementary Fig. 60** in SI). The standard MPPT tests reveal that the FMTPA-CPA-based devices retains ~97% during continuous MPPT for 1,080 h under 100 mW cm^{-2} MH light (4.4% UV inside, the spectrum is shown in **Fig. R56** (i.e., **Supplementary Fig. 59b** in SI)) in N_2 atmosphere, whereas the 2PACz-based and FTPA-CPA-based devices fall to below 84% and 46% of their initial efficiency after 600 h. These comprehensive measurements present a key result demonstrating the exceptional long-term photothermal stability and practical durability of resonance molecular design strategy.

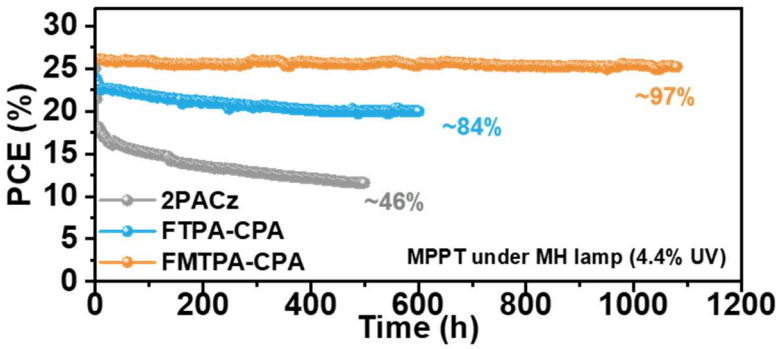

Fig. R55 (i.e., **Supplementary Fig. 60** in SI) Light-soaking stability of small-area devices (MPPT conditions) ased on 2PACz, FTPA-CPA and FMTPA-CPA under the illumination of MH lamp (100 mW cm^{-2}, 4.4% UV inside) in N_2 atmosphere.

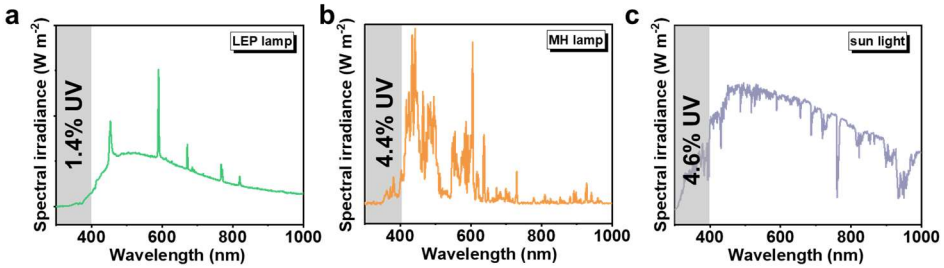

Fig. R56 (i.e., **Supplementary Fig. 59** in SI) Spectrum of the light source for light-soaking stability tests (a) LEP lamp; (b) MH lamp and (c) sunlight. The inset showed the UV ratio of the lamp in each spectrum.

The corresponding revisions for the Manuscript (marked red) are listed below:

Page 12 in the revised Manuscript: To evaluate the industrial potential of D-A-D FMTPA-CPA-based devices, we conduct more stability test according to protocols that mimic the real operation process. Considering UV light is the primary cause of bond dissociation between ITO and SAMs, we measure the UV illumination stability of devices under UV light (365 nm, 56 mW cm^{-2}) in a N_2 filled glovebox (**Supplementary Fig. 58 & Table 16**). The FMTPA-CPA-based device can maintain ~81% of their initial efficiency after 1,080 h while the FTPA-CPA and 2PACz-based devices retain only 62% and 43%, respectively, after 700 h. In addition, we evaluate device stability under a combined environment of UV-inclusive light (metal halide (MH) lamp, 100 mW cm^{-2}, 4.4% UV inside, the spectrum in **Supplementary Fig. 59**) and thermal stress (85±5ºC). The FMTPA-CPA-based device maintains 93% of its initial efficiency during continuous MPPT for 1,080 h, while the FTPA-CPA and 2PACz-based devices retain only 74% and 26% after 600 h (**Fig. 4f & Supplementary Fig. 60 & Fig. 61 &** more details of UV-inclusive stability can be found in **Supplementary Note 10**), demonstrating that the D-A-D resonance molecular design strategy substantially enhances practical photothermal stability under realistic UV-inclusive conditions.[17]

Page 18 in the revised Supplementary Information:

Supplementary Note 10 the stability of combined environment of light including UV and heat

We evaluated stability under UV-inclusive light (metal halide (MH), 100 mW cm^{-2}, 4.4% UV inside, the spectrum in **Supplementary Fig. 59**). The FMTPA-CPA-based device

maintains 97% of its initial efficiency after continuous MPPT for 1,080 h, while the FTPA-CPA and 2PACz-based devices retained only 84% and 46% after 600 h (**Supplementary Fig. 60**).

For the comment "*Additionally, the initial PCE values for all devices subjected to stability tests must be provided to allow readers to assess the starting point.*", we summarized the initial performance of all devices applied in the stability measurement in **Table R3** (i.e., **Supplementary Table 17** in SI).

Table R3 (i.e., **Supplementary Table 17** in SI) The initial photovoltaic parameters of pero-SCs under different stability protocols (under AM 1.5G illumination, the light emitting diode (LED), light emitting plasma (LEP), metal halide lamp (MH) solar simulator, 100 mW cm^{-2}).

protocols	SAMs	V_{oc} (V)	J_{sc} (mA/cm^2)	FF (%)	PCE (%)
ISOS-D-2	2PACz	1.16±0.01	26.45±0.08	80.4±0.7	24.66±0.25
	FTPA-CPA	1.18±0.01	26.57±0.13	82.1±0.3	25.70±0.18
	FMTPA-CPA	1.20±0.01	26.59±0.05	83.5±0.3	26.68±0.19
ISOS-T-3	2PACz	1.16±0.01	26.45±0.08	80.5±0.7	24.70±0.26
	FTPA-CPA	1.19±0.01	26.47±0.08	82.1±0.5	25.74±0.22
	FMTPA-CPA	1.20±0.01	26.59±0.07	83.4±0.3	26.69±0.20
ISOS-L-2	2PACz	1.16±0.01	25.81±0.12	80.8±0.5	24.19±0.28
	FTPA-CPA	1.19±0.01	25.89±0.07	82.8±0.4	25.44±0.17
	FMTPA-CPA	1.20±0.01	25.99±0.08	83.9±0.4	26.25±0.13
ISOS-LC-1	2PACz	1.16±0.01	25.69±0.10	80.6±0.5	24.11±0.25
	FTPA-CPA	1.19±0.01	25.78±0.08	82.3±0.5	25.17±0.15
	FMTPA-CPA	1.21±0.01	25.90±0.04	83.3±0.7	26.00±0.11
ISOS-D-3	2PACz	1.16±0.01	26.39±0.12	80.3±0.5	24.59±0.22
	FTPA-CPA	1.18±0.01	26.45±0.10	82.3±0.6	25.77±0.11
	FMTPA-CPA	1.20±0.01	26.56±0.06	83.8±0.8	26.74±0.15
UV irradiation	2PACz	1.17±0.01	26.46±0.09	80.5±0.4	24.89±0.25
	FTPA-CPA	1.19±0.01	26.51±0.08	81.8±0.6	25.82±0.08
	FMTPA-CPA	1.20±0.01	26.58±0.05	83.9±0.6	26.84±0.10
MPPT (MH lamp)	2PACz	1.17±0.01	25.55±0.09	80.2±0.7	23.91±0.29
	FTPA-CPA	1.19±0.01	25.58±0.07	82.1±0.7	25.01±0.17
	FMTPA-CPA	1.21±0.01	25.69±0.03	84.0±0.8	26.02±0.13
MPPT at 85±5°C (LEP lamp)	2PACz	1.17±0.01	25.90±0.14	80.8±0.7	24.46±0.31
	FTPA-CPA	1.19±0.01	26.01±0.07	81.5±0.9	25.25±0.20

	FMTPA-CPA	1.21±0.01	26.06±0.06	83.7±0.8	26.30±0.12
MPPT at 85±5℃ (MH lamp)	2PACz	1.17±0.01	25.69±0.07	80.9±0.9	24.26±0.28
	FTPA-CPA	1.19±0.01	25.73±0.06	81.9±0.6	25.04±0.16
	FMTPA-CPA	1.21±0.01	25.78±0.05	83.6±0.8	26.01±0.10

The average PCE, and standard deviations of 10 devices.

Response to Reviewers' Comments

We would like to thank all the reviewers for their positive evaluation of our response. For the remaining comments and insightful questions, we have now revised the manuscript and added experimental data to address the reviewers' concerns. The point-by-point response is attached in this document, which have helped us to significantly improve the manuscript. **These revisions have also been highlighted with red** in the main text and Supplementary Information. We hope that our revised version is now suitable for publication.

Response to Reviewer #1:

The authors have addressed most of my previous comments. However, I remain confused about the configuration analysis in this work. Specifically, two structurally similar molecules exhibit two different configurations: FTPA-CPA is assigned an E configuration, while FMTPA-CPA is assigned a Z configuration. I strongly recommend that the authors provide additional experimental evidence to support these DFT conclusions, such as single-crystal X-ray diffraction analysis or NMR measurements. Furthermore, the interconversion between E and Z configurations is generally challenging, as it requires a significant input of energy to overcome the π-bond barrier. The authors should consider these experimental approaches and the mechanism rather than relying solely on simulations based on the DFT results.

Response: Thanks for the reviewer's positive evaluation of our response. For the concern of the configuration analysis, we follow the reviewer's suggestion and added: (1) ^{1}H and ^{31}P nuclear magnetic resonance (NMR) measurements to determine the configuration distribution of the free molecules; and (2) Sum Frequency Generation (SFG) and X-ray Reflectivity (XRR) measurements to probe molecular configurations when anchoring on indium tin oxide (ITO) substrate. These experimental results are consistent with the conclusions predicted by Density functional theory (DFT) calculations.

For free molecules, we employed ^{1}H NMR and ^{31}P NMR spectroscopy to determine molecular configuration (*Chem. Rev.*, **2004**, 104, 1, 17-118). Before conducting NMR measurement, we first analyzed the chemical environment of E and Z configuration by electrostatic surface potential (ESP) calculations. As shown in **Fig. R1** (i.e., **Supplementary Fig. 15** in SI), the H and P atoms adjacent to the C=C double bond that are assigned to the E configuration all exhibit lower electrostatic potential (i.e., higher electron density) compared to Z configuration in both FTPA-CPA and FMTPA-CPA. Therefore, E configuration in FTPA-CPA and FMTPA-CPA appears at lower chemical shift (δ) relative to the Z configuration (James Keeler, Understanding NMR Spectroscopy (Section 3: Energy levels and NMR spectra); *J. Phys. Chem. A*, **2013**, 117, 497-503; *J. Org. Chem.*, **2012**, 77, 4, 1693-1700). In ^{1}H NMR measurement, FTPA-CPA powder with free molecule structure exhibits two distinct sets of signals in the vinylic proton (i position of FTPA-CPA in **Fig. R2a** (i.e., **Supplementary Fig. 1a** in SI)), at 7.57-7.64 ppm and 7.68-7.72 ppm, which were assigned to the E and Z

configurations, respectively (**Fig. R2b** (i.e., **Supplementary Fig. 1b** in SI)). The integration gave an E:Z ratio of 96:4. In comparison, the ^{31}P NMR spectrum displayed two signals at 5.51 and 5.58 ppm, with E:Z ratio of 95:5 (**Fig. R3** (i.e., **Supplementary Fig. 2** in SI)). The consistency in E:Z ratio with E as the dominant configuration confirms FTPA-CPA tends to exhibit E configuration. A similar analysis was also performed on FMTPA-CPA. In both the ^{1}H and ^{31}P NMR spectrum, the E:Z ratios are highly consistent, giving 8:92 and 9:91, respectively (**Fig. R4 & R5** (i.e., **Supplementary Fig. 5 & 6** in SI)). It confirms that free FMTPA-CPA predominantly adopts the Z configuration. These experimental results are consistent with the DFT calculation results. Taken together, although FTPA-CPA and FMTPA-CPA have a similar anchoring cyanovinyl phosphonic acid (CPA) group, the additional symmetric triphenylamine group in FMTPA-CPA changes the steric and electronic resonance around the C=C bond, which results in the difference of the stabilized molecular configuration (*Science*, **2023**, 380, 404; *ACS Energy Lett.*, **2021**, 6, 869).

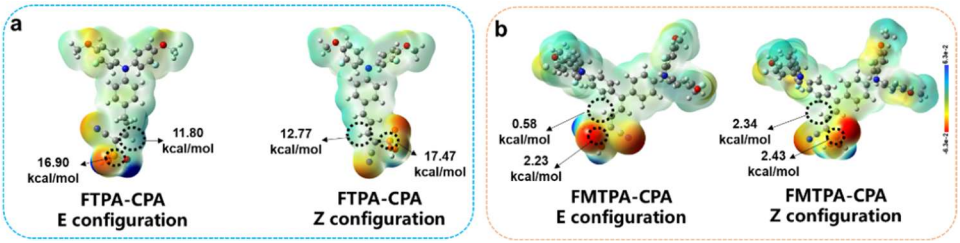

Fig. R1 (i.e., **Supplementary Fig. 15** in SI) (a) ESP distributions of E and Z configuration FTPA-CPA; (b) ESP distributions of E and Z configuration FMTPA-CPA.

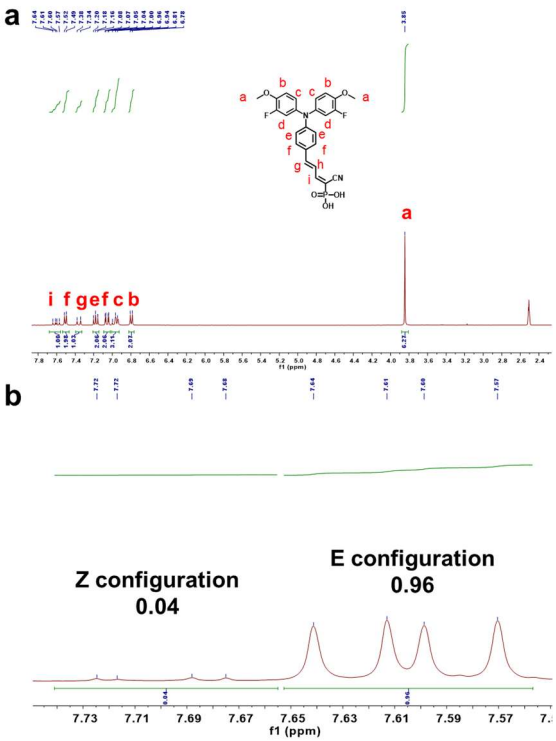

Fig. R2 (i.e., **Supplementary Fig. 1** in SI) (a) ^{1}H NMR spectrum of FTPA-CPA; (b) enlarged ^{1}H NMR spectrum in the range of 7.56-7.74 ppm.

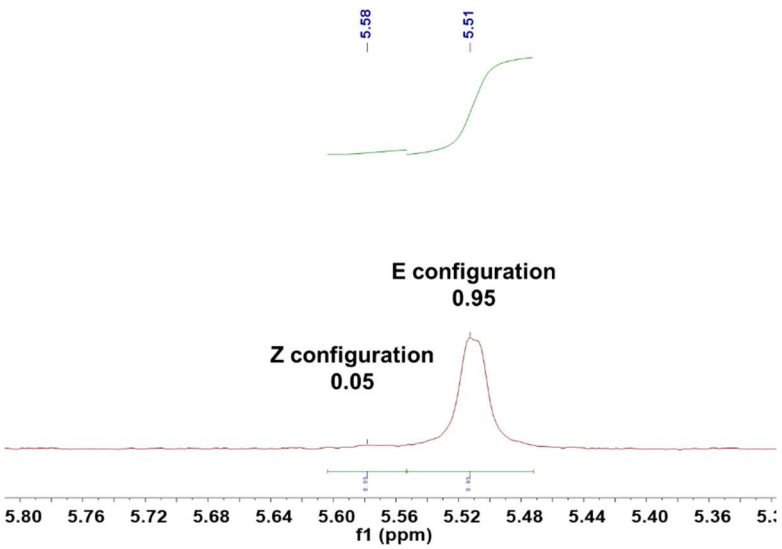

Fig. R3 (i.e., **Supplementary Fig. 2** in SI) ^{31}P NMR spectrum of FTPA-CPA.

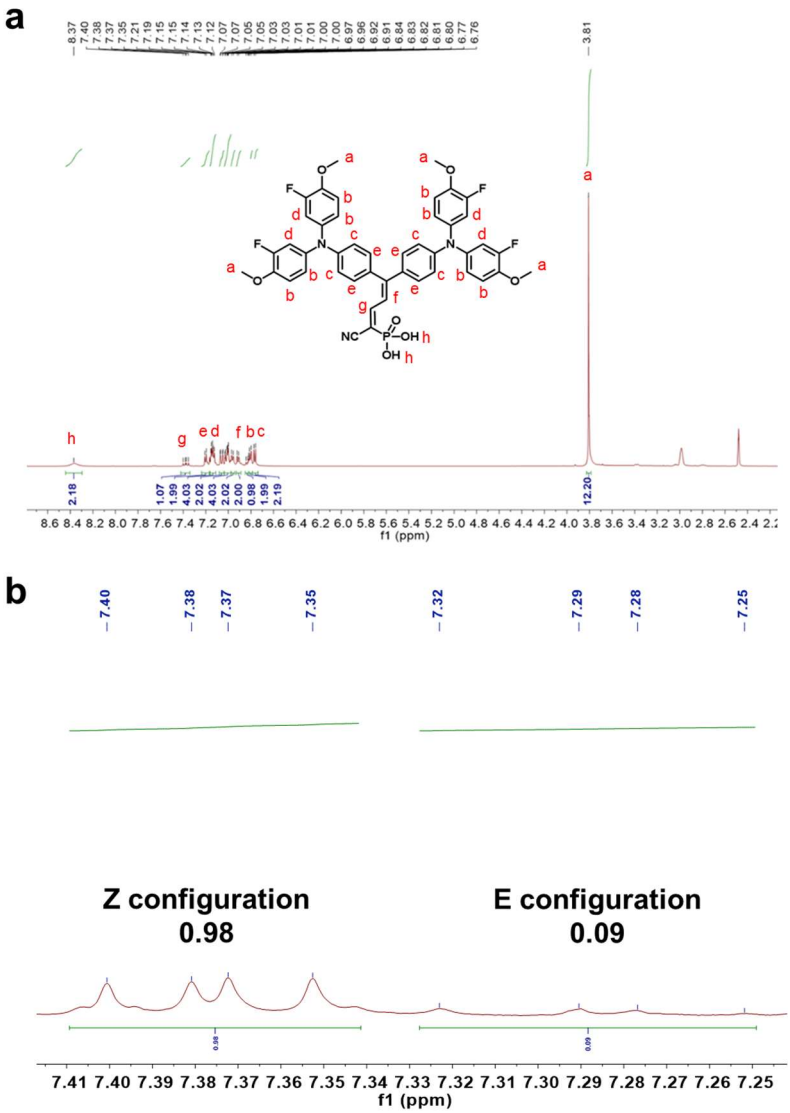

Fig. R4 (i.e., **Supplementary Fig. 5** in SI) (a) ^{1}H NMR spectrum of FMTPA-CPA; (b) enlarged ^{1}H NMR spectrum in the range of 7.25–7.41 ppm.

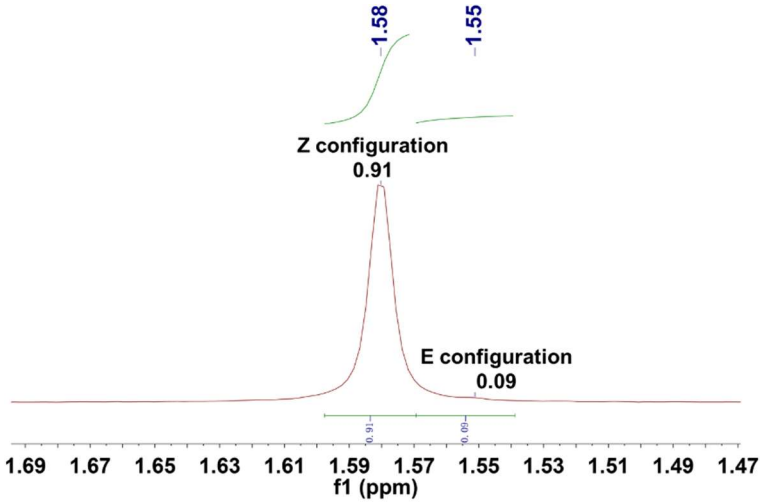

Fig. R5 (i.e., **Supplementary Fig. 6** in SI) ^{31}P NMR spectrum of FMTPA-CPA.

For molecules anchored on ITO, we quantified the height and orientation of FTPA-CPA and FMTPA-CPA SAM to define their anchoring configuration. As shown in **Fig. R6** (i.e., **Supplementary Fig. 11** in SI), XRR revealed molecular heights of 15.9 Å for FTPA-CPA and 16.9 Å for FMTPA-CPA, which are close to the previously calculated anchoring heights of the energetically favored Z configuration on ITO (15.5 Å for FTPA-CPA and 16.7 Å for FMTPA-CPA) (*Nat Commun.*, **2025**, 16, 86; *Adv. Mater.*, **2026**, 38, e21898). In addition, SFG spectroscopy was used to determine average tilt angle of FTPA-CPA on ITO (**Fig. R7** (i.e., **Supplementary Fig. 12** in SI)). The measured average tilt angle relative to the substrate normal is ~24°, which is much closer to the calculated value of Z configuration (38°) on ITO rather than E configuration (0°). This result implies the anchored FTPA-CPA is assigned mainly to the Z configuration (*Nat. Mater.*, **2026**, 10.1038/s41563-026-02546-1; *Adv. Mater.*, **2025**, 37, e02485; *Joule*, **2026**, 10.1016/j.joule.2026.102380).

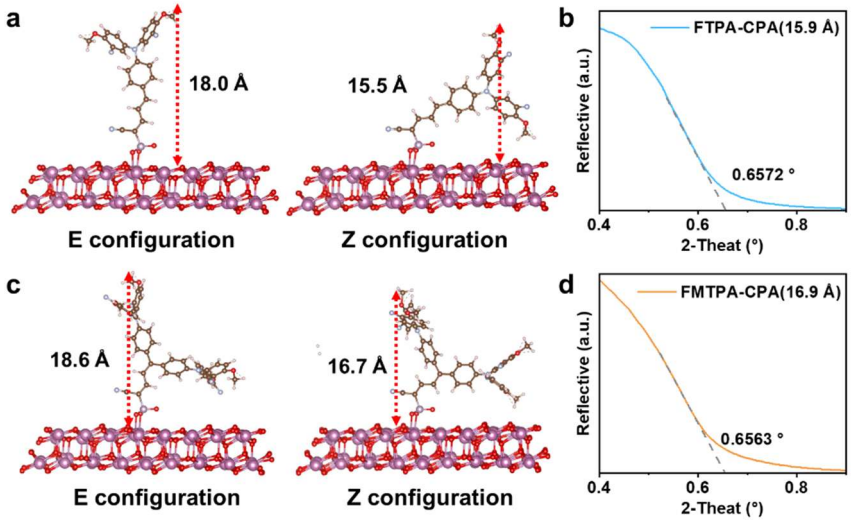

Fig. R6 (i.e., **Supplementary Fig. 11** in SI) (a) theoretical calculated heights for E- and Z- configurations FTPA-CPA anchored to ITO; (b) XRR measurements of FTPA-CPA SAM films after AcOH washing; (c) theoretical calculated heights for E- and Z-

configurations FMTPA-CPA anchored to ITO; (d) XRR measurements of FMTPA-CPA SAM films after AcOH washing.

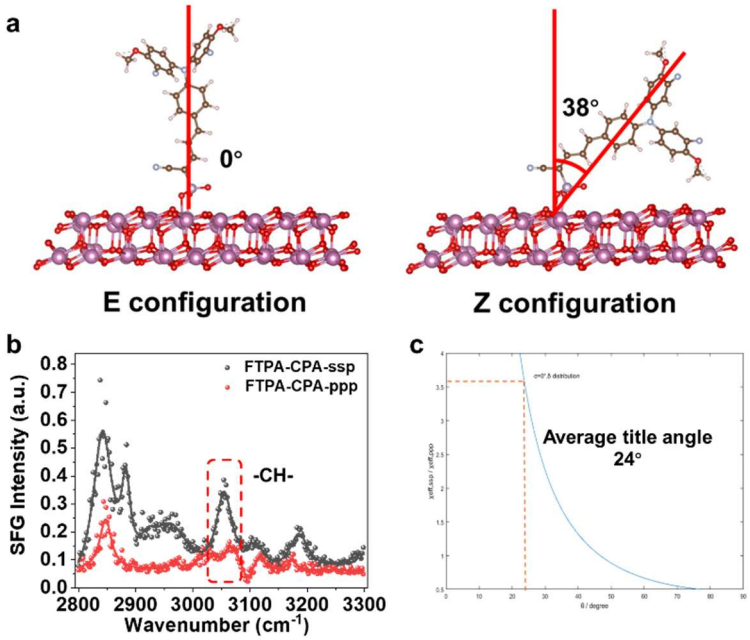

Fig. R7 (i.e., **Supplementary Fig. 12** in SI) (a) theoretically calculated tilt angle for E- and Z- configurations FTPA-CPA anchored to ITO; (b) the SFG spectra of the FTPA-CPA SAM films after AcOH washing; (c) the predicted average title angle of FTPA-CPA SAMs on ITO by SFG spectra.

We agree with the reviewer that "*interconversion between E and Z configurations is generally challenging*". In fact, the final SAM configuration on the ITO substrate is determined by selective anchoring rather than the interconversion between E and Z configuration (*Adv. Mater.*, **2023**, 35, 2304415; *Adv. Mater.*, **2024**, 36, 2311970). For the anchoring reaction of FTPA-CPA molecule onto ITO, the Z configuration is energetically more favored than E configuration (i.e., the activation energy difference of E and Z configuration ($\Delta E_{E\text{-}Z}$) = 0.66 eV as shown in **Supplementary Fig. 10**). Considering the Brønsted principle (Anslyn, E. V. et al., Modern Physical Organic Chemistry; *J. Phys. Org. Chem.*, **1990**, 3, 1-8), in acid-base reactions, a linear relationship exists between $\Delta E_{E\text{-}Z}$ and the standard Gibbs free energy difference of E and Z configuration ($\Delta G_{E\text{-}Z}$), where the parameter α is the Brønsted coefficient (0.5).

$$\Delta G_{E-Z} = \alpha \cdot \Delta E_{E-Z}$$

Therefore, the anchoring reaction rates of E and Z configuration molecules on ITO substrate can be calculated using the Arrhenius equation.

$$\frac{k_E}{k_Z} \propto \exp\left(-\frac{\Delta G_{E-Z}}{RT}\right)$$

Where k_E and k_Z are the anchoring reaction rate of E and Z configuration molecules on ITO, respectively; R denotes universal constant; T is the temperature. As a result, when we deposit FTPA-CPA solution with both configurations onto ITO substrate, the Z configuration FTPA-CPA molecules have a much faster anchoring reaction rate

compared to the E configuration molecules ($k_E/k_Z \approx 2.62*10^{-6}$). Then, the rapidly anchored Z configuration FTPA-CPA molecules prevent the E configuration molecules anchoring due to the steric hinderance, resulting in a SAM predominantly composed of the Z configuration anchored on the ITO substrate.

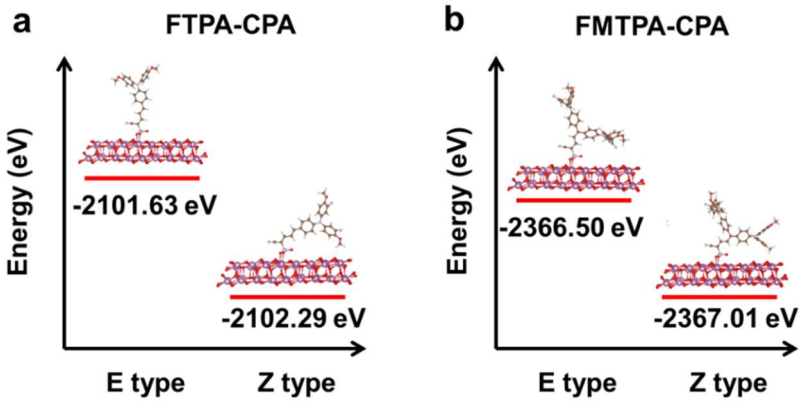

Supplementary Fig. 10 The total energies of the whole systems composed of (a) FTPA-CPA and (b) FMTPA-CPA with E (Z) configuration on the ITO substrate.

To further address the reviewer's concern regarding whether the quantity of Z configuration FTPA-CPA is enough for the full coverage of ITO substrate, we performed quantitative estimation based on the preparation conditions. The spin-coating solution concentration was 0.5 mg mL^{-1} for FTPA-CPA, and 30 μL of solution corresponding to 1.08×10^{16} molecules in total was deposited on a 1.5 cm × 1.5 cm ITO substrate. According to the ^{1}H and ^{31}P NMR results, the ratio of Z configuration free molecule is 4~5%, which corresponds to $4.31\sim5.39\times10^{14}$ molecules. For a 1.5 cm × 1.5 cm ITO substrate, the number of molecules required for a full compact monolayer, as estimated from the molecular footprint, is on the order of $2.25\sim4.50\times10^{14}$ molecules. Even for 100% surface coverage, the initially present Z configuration molecules are already sufficient in principle to populate nearly the entire substrate surface. Therefore, as for FTPA-CPA, the result is attributed to preferential adsorption of Z configuration molecules on the ITO substrate, while E configuration molecules are more readily removed during spin-coating and EtOH washing post-treatment.

We have added the discussion of the molecule configuration and measurements details in the revised Supporting Information.

Page 5 in the revised Supporting Information:

Supplementary Note 2. The discussion of molecular configuration

We employed ^{1}H NMR and ^{31}P NMR spectroscopy to determine molecular configuration.[6] Before conducting NMR measurement, we first analyzed the chemical environment of E and Z configuration by electrostatic surface potential (ESP) calculations. As shown in **Supplementary Fig. 15**, the H and P atoms adjacent to the C=C double bond that are assigned to the E configuration all exhibit lower electrostatic potential (i.e., higher electron density) compared to Z configuration in both FTPA-CPA

and FMTPA-CPA. Therefore, E configuration in FTPA-CPA and FMTPA-CPA appears at lower chemical shift (δ) relative to the Z configuration.[7,8] In ^{1}H NMR measurement, FTPA-CPA powder with free molecule structure exhibits two distinct sets of signals in the vinylic proton (i position of FTPA-CPA in **Supplementary Fig. 1a**), at 7.57-7.64 ppm and 7.68-7.72 ppm, which were assigned to the E and Z configurations, respectively (**Supplementary Fig. 1b**). The integration gave an E:Z ratio of 96:4. In comparison, the ^{31}P NMR spectrum displayed two signals at 5.51 and 5.58 ppm, with E:Z ratio of 95:5 (**Supplementary Fig. 2**). The consistency in E:Z ratio with E as the dominant configuration confirms FTPA-CPA tends to exhibit E configuration. A similar analysis was also performed on FMTPA-CPA. In both the ^{1}H and ^{31}P NMR spectrum, the E:Z ratios are highly consistent, giving 8:92 and 9:91, respectively (**Supplementary Fig. 5 & 6**). It confirms that free FMTPA-CPA predominantly adopts the Z configuration. These experimental results are consistent with the DFT calculation results. Taken together, although FTPA-CPA and FMTPA-CPA have a similar anchoring cyanovinyl phosphonic acid (CPA) group, the additional symmetric triphenylamine group in FMTPA-CPA changes the steric and electronic resonance around the C=C bond, which results in the difference of the stabilized molecular configuration.[9]

Page 6 in the revised Supporting Information:

We quantified the height and orientation of anchored FTPA-CPA and FMTPA-CPA to define the anchoring configuration. As shown in **Supplementary Fig. 11**, XRR revealed molecular heights of 15.9 Å for FTPA-CPA and 16.9 Å for FMTPA-CPA, which are close to the previously calculated anchoring heights of the energetically favored Z configuration on ITO (15.5 Å for FTPA-CPA and 16.7 Å for FMTPA-CPA).[10] In addition, SFG spectroscopy was used to determine average tilt angle of FTPA-CPA on ITO (**Supplementary Fig. 12**). The measured average tilt angle relative to the substrate normal is ~24°, which is much closer to the calculated value of Z configuration (38°) on ITO rather than E configuration (0°). This result implies the anchored FTPA-CPA is assigned mainly to the Z configuration.[11,12]

Page 6 in the revised Supporting Information:

Supplementary Note 3. The X-ray reflectivity (XRR) calculation details

XRR measurements were used to determine the thickness of anchored SAMs. In **Supplementary Fig. 11**, as the incident angle (2θ) increases, the attenuated reflectivity curve shows an inflection point. Upon magnification, at the inflection point, the thickness (d) of the SAM layer can be calculated using the formula:

$$\theta^2 - \alpha_c^2 = m^2 \frac{\lambda}{2d}^2$$

Where (0.325°) is the critical angle for total reflection at the ITO substrate interface, m is the order of diffraction fringes (m=1), and λ (0.15404 nm) is the X-ray wavelength (Cu Kα).

Page 7 in the revised Supporting Information:

Supplementary Note 4. The Sum Frequency Generation (SFG) calculation details

The visible and infrared beams were focused and superimposed on the quartz/SAM samples in order to generate the SFG signals. An optical parametric generation/amplification and difference frequency generation (OPG/OPA/DFG) system, based on LiB_3O_5 and $AgGaS_2$ crystals, was employed to generate an IR beam with a tunable wavenumber ranging from 1000 to 4300 cm^{-1}. The wavelength of the visible beam was fixed at 532 nm, derived from a Nd:YAG laser. The SFG spectra were collected with the *ssp* and *ppp* (with the letters from left to right representing the polarization of the output SFG field, the input visible and infrared field, respectively) polarization combinations, with a wavenumber step of 5 cm^{-1}. For this vibrational mode, the polarization-dependent effective susceptibilities can be related to the molecular tilt angle θ (between the vibrational axis and the surface normal) by

$$\frac{\chi_{eff,spp}}{\chi_{eff,ppp}} = \frac{0.29 < cos\theta > +0.08 < cos^3\theta >}{0.62 < cos\theta > -0.62 < cos^3\theta >}$$

Where $X_{eff,spp}$ and $X_{eff,ppp}$ are the effective macroscopic second-order susceptibility of spp and *ppp* polarization combinations, respectively; The orientational averages are defined as

$$< cos\theta >= \int_0^{\pi} cos\theta f(\theta)\, sin\theta d\theta$$

$$< cos^3\theta >= \int_0^{\pi} cos^3\theta f(\theta)\, sin\theta d\theta$$

Assuming a Gaussian orientational distribution:

$$f(\theta) = Cexp[-\frac{(\theta - \theta_0)^2}{2\sigma^2}]$$

where C is the normalization constant, θ_0 is the average tilt angle, and σ describes the orientational distribution width.

Response to Reviewer #2:

The authors have addressed most of my previous concerns satisfactorily. The revised manuscript represents a substantial improvement over the original submission. However, a few issues still remain that require further attention before I can recommend acceptance of this manuscript.

Response: Thanks for the reviewer's positive evaluation of our response. For the remaining issues, we have responded to the concerns point-to-point as follows.

1.The authors added UV stability data but did not provide a clear mechanistic discussion for why FMTPA-CPA resists UV-induced degradation. The Science paper by Fei et al. proposed that UV selectively cleaves weak hydrogen-bonded PA–TCO interactions through a photochemical pathway distinct from thermal hydrolysis. A more in-depth mechanistic discussion addressing this UV-specific degradation pathway would be needed to substantiate the claim of superior UV stability.

Response: Thanks for the reviewer's comments that help us to deepen the understanding on the mechanism of UV stability. With detailed investigations, we attribute the degradation under UV-inclusive light primarily to a photochemical pathway similar to the recently published *Science* paper by Fei et al. (*Science*, **2026**, 391, 6780), while stronger pure UV irradiation further promotes defects generation and phase segregation within the perovskite bulk (*Science*, **2024**, 384, 1126-1134).

To verify the UV degradation mechanism, we prepared ITO/SAM (with EtOH washing)/perovskite samples. In the previous response of Comment 1 from Reviewer 3, after EtOH washing, the initial coverage of 2PACz and FTPA-CPA may include a certain amount of weak hydrogen-bonded SAMs due to the severe molecular aggregation, and the D-A-D resonant FMTPA-CPA tends to form uniform and covalently anchored monolayer. Then, these samples were aged under metal halide (MH, 4.4% UV inside) lamp and pure UV (365 nm, 56 mW cm^{-2}) lamp, respectively. As for 2PACz and FTPA-CPA, the perovskite buried interfaces showed increased voids and decreased PL intensity after aged 200 h under MH lamp (**Fig. R8 & R9** (i.e., **Supplementary Fig. 74 & 75** in SI)). The significant change is ascribed to weak hydrogen-bonded SAM anchored on ITO, which is triggered by photochemical reaction involving the reaction between deprotonated hydrogen from CPA group with formamidinium cation (FA^+) or iodide (I^-), thereby promoting degradation of the buried perovskite interface (*Science*, **2026**, 391, 6780). In contrast, the perovskite buried interface based on FMTPA-CPA showed only minimal differences, indicating that the robust and stable covalent anchoring of D-A-D resonant FMTPA-CPA will not be influenced by UV photochemical degradation pathway.

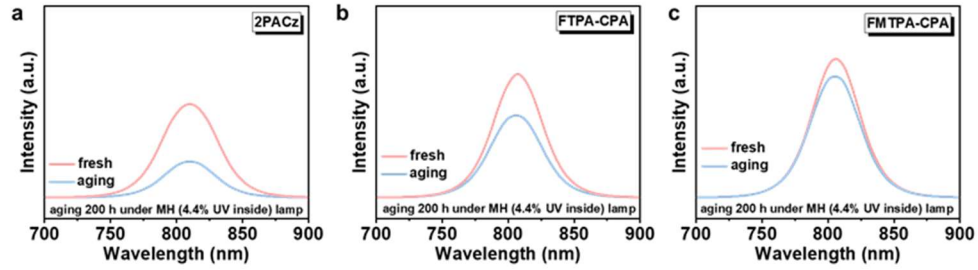

Fig. R8 (i.e., **Supplementary Fig. 74** in SI) PL peak of buried perovskite interface based (a) 2PACz, (b) FTPA-CPA and (c) FMTPA-CPA before and after aging under the MH lamp.

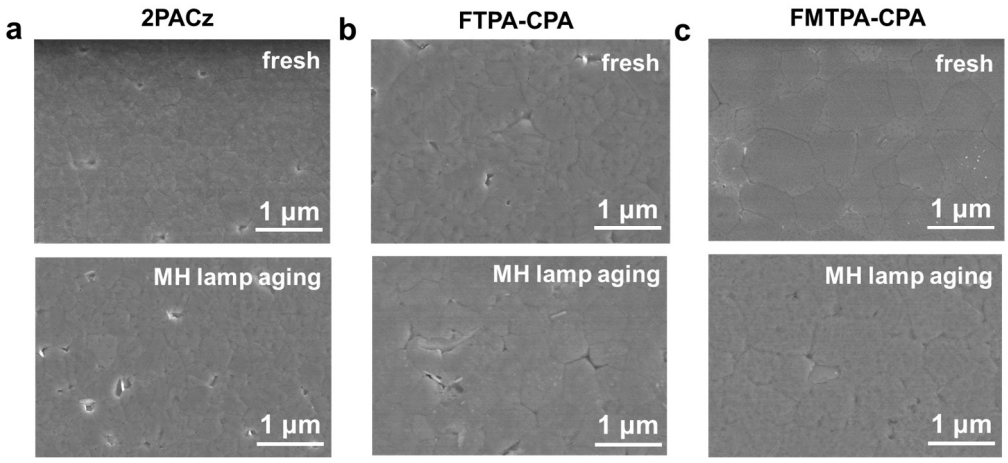

Fig. R9 (i.e., **Supplementary Fig. 75** in SI) SEM of buried perovskite interface based (a) 2PACz, (b) FTPA-CPA and (c) FMTPA-CPA before and after aging under the MH lamp.

Furthermore, we investigate the degradation mechanism after 200 h aging under pure UV (365 nm, 56 mW cm^{-2}) lamp. As for 2PACz and FTPA-CPA, the buried interface degradation became much more severe than that under MH lamp (**Fig. R10 & R11** (i.e., **Supplementary Fig. 76 & 77** in SI)), as evidenced by increased voids, the appearance of bright crystals (referring to PbI_2), and decreased PL intensity. In addition, the PL peaks exhibited a blue shift, which was ascribed to ion migration of A-site cations (e.g., Cs^+, FA^+) that induces weak phase segregation (*Science*, **2024**, 384, 1126-1134). These results indicate that under harsher pure UV irradiation, the degradation is not only limited to photochemical desorption of weakly hydrogen-bonded SAMs, but also involves UV-induced defects generation and ion migration within the perovskite bulk (*Science*, **2024**, 384, 1126-1134). Similarly, the FMTPA-CPA-based buried perovskite interfaces also exhibited bright crystals formation, accompanied by PL intensity decrease and peak blue shift. However, after pure UV lamp aging, the P/In ratio of FMTPA-CPA anchored on ITO showed no significant change from XPS characterization in **Fig. R12** (i.e., **Supplementary Fig. 78** in SI) and **Table R1** (i.e., **Supplementary Table 8** in SI). Therefore, we attribute the degradation mainly to UV-

induced defects generation and phase segregation in the perovskite bulk, rather than desorption of the FMTPA-CPA SAM itself.

Overall, the above results support that the degradation pathway under UV-inclusive light mainly originates from photochemical degradation of the weakly hydrogen-bonded SAMs, while stronger pure UV lamp further promotes defects generation and phase segregation within the perovskite bulk.

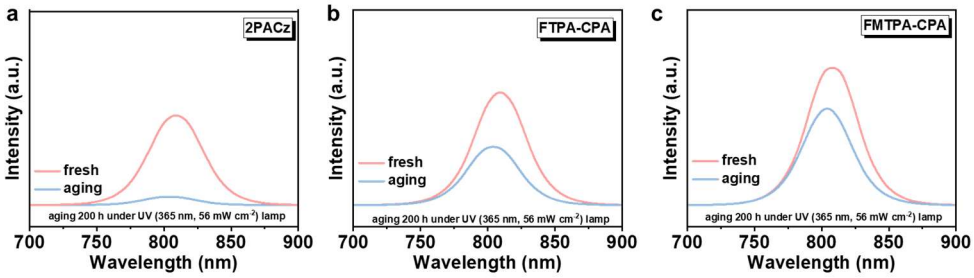

Fig. R10 (i.e., **Supplementary Fig. 76** in SI) PL peak of buried perovskite interface based (a) 2PACz, (b) FTPA-CPA and (c) FMTPA-CPA before and after aging under the pure UV lamp.

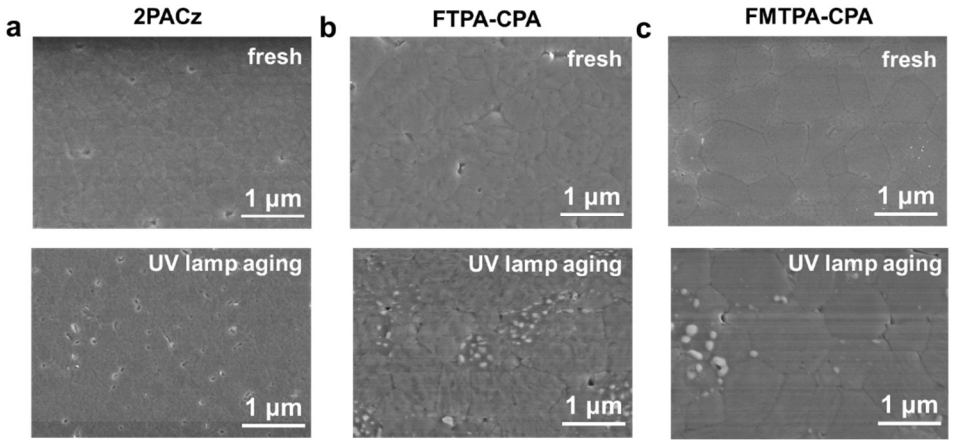

Fig. R11 (i.e., **Supplementary Fig. 77** in SI) SEM of buried perovskite interface based (a) 2PACz, (b) FTPA-CPA and (c) FMTPA-CPA before and after aging under the pure UV lamp.

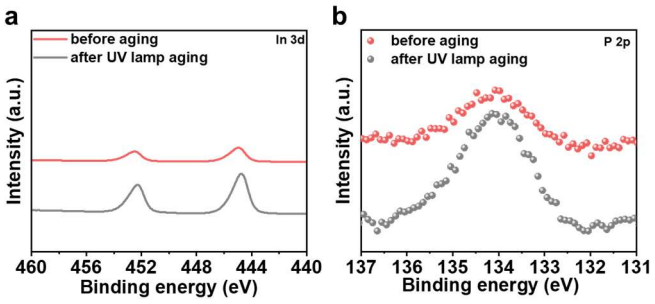

Fig. R12 (i.e., **Supplementary Fig. 78** in SI) XPS spectra of (a)In 3d and (b) P 2p obtained from the FMTPA-CPA films before and after UV irradiation.

Table R1 (i.e., **Supplementary Table 8** in SI**)** XPS spectra analysis obtained from the FMTPA-CPA films before and after aging under UV lamp.

SAM	condition	In area	P area	P/In
FMTPA-CPA	before aging (EtOH washing)	183058.1	4228.6	0.0231
	after UV lamp aging	536154.2	12281.1	0.0229

We have added the discussion of the UV degradation mechanism in the revised Supporting Information.

Pages 16~17 in the revised Supporting Information:

Supplementary Note 14. Stability Mechanism Analysis

To verify the UV degradation mechanism, we prepared ITO/SAM (with EtOH washing)/perovskite samples. As shown in **Supplementary Note 10**, after EtOH washing, the initial coverage of 2PACz and FTPA-CPA may include a certain amount of weak hydrogen-bonded SAMs due to the severe molecular aggregation, and the D-A-D resonant FMTPA-CPA tends to form uniform and covalently anchored monolayer. Then, these samples were aged under metal halide (MH, 4.4% UV inside) lamp and pure UV (365 nm, 56 mW cm^{-2}) lamp, respectively. As for 2PACz and FTPA-CPA, the perovskite buried interfaces showed increased voids and decreased PL intensity after aged 200 h under MH lamp (**Supplementary Fig. 74 & 75**). The significant change is ascribed to weak hydrogen-bonded SAM anchored on ITO, which is triggered by photochemical reaction involving the reaction between deprotonated hydrogen from CPA group with formamidinium cation (FA^+) or iodide (I^-), thereby promoting degradation of the buried perovskite interface.[33] In contrast, the perovskite buried interface based on FMTPA-CPA showed only minimal differences, indicating that the robust and stable covalent anchoring of D-A-D resonant FMTPA-CPA will not be influenced by UV photochemical degradation pathway.

Furthermore, we investigate the degradation mechanism after 200 h aging under pure UV (365 nm, 56 mW cm^{-2}) lamp. As for 2PACz and FTPA-CPA, the buried interface degradation became much more severe than that under MH lamp (**Supplementary Fig. 76 & 77**), as evidenced by increased voids, the appearance of bright crystals (referring to PbI_2), and decreased PL intensity. In addition, the PL peaks exhibited a blue shift, which was ascribed to ion migration of A-site cations (e.g., Cs^+, FA^+) that induces weak phase segregation.[39] These results indicate that under harsher pure UV irradiation, the degradation is not only limited to photochemical desorption of weakly hydrogen-bonded SAMs, but also involves UV-induced defects generation and ion migration within the perovskite bulk. Similarly, the FMTPA-CPA-based buried perovskite interfaces also exhibited bright crystals formation, accompanied by PL intensity decrease and peak blue shift. However, after pure UV lamp aging, the P/In ratio of FMTPA-CPA anchored on ITO showed no significant change from XPS characterization in **Supplementary Fig. 78** and **Supplementary Table 8**. Therefore, we attribute the degradation mainly to UV-induced defects generation and phase

segregation in the perovskite bulk, rather than desorption of the FMTPA-CPA SAM itself.

2.The promising small-cell results of FMTPA-CPA raise the question of whether the enhanced stability translates to large-area modules. Given that the Science paper by Fei et al. (10.1126/science.adz7969) has already demonstrated module-level operational stability under combined UV and thermal stress, providing equivalent module-scale data would further strengthen the impact of this work for Nature.

Response: Thanks for the reviewer's valuable comments. We also recognize that module-level operational stability under combined UV and thermal stress is important to the industrialization potential of our D-A-D resonant SAM. The UV (MH (4.4% UV inside)) and heat (85±5ºC) stability of modules had already been under parallel investigation since last round of review.

As shown in our pervious response in Comment 6 of reviewer #1 and Comment 14 of reviewer#3, we replaced bathocuproine (BCP) with atomic-layer-deposited SnO_2 to exclude possible side effects from other interlayers. This leads to slightly decrease in the efficiency of the small-area devices. Similarly, the initial PCE of FMTPA-CPA based module (aperture area of 15.64 cm^2) was 22.16%, which was slightly lower than the champion efficiency (23.6%). As shown in **Fig. R13** (i.e., **Supplementary Fig. 67** in SI), the FMTPA-CPA-based module maintains ~90% of its initial efficiency after continuous maximum-power-point tracking (MPPT) for 1,080 h, whereas the FTPA-CPA-based and 2PACz-based modules fall to below ~73% and ~28% of their initial efficiency after 900 h. These UV-inclusive light and heat stability results of modules are comparable with the recent *Science* paper (*Science*, **2026**, 391, 6780), demonstrating the practical durability of modules using the D-A-D resonant SAM.

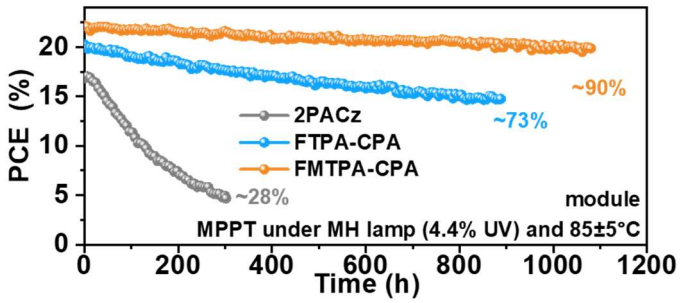

Fig. R13 (i.e., **Supplementary Fig. 67** in SI) MPPT stability of modules based on 2PACz, FTPA-CPA and FMTPA-CPA at 85±5°C under the illumination of MH lamp (100 mW cm^{-2}, 4.4% UV inside).

We have added stability of combined environment of light including UV and thermal stress in the revised Supplementary Information (marked red):

Page 15 in the revised Supplementary Information:

Supplementary Note 13 the stability of combined environment of light including UV and heat

Furthermore, to demonstrate the industrialization potential of our D-A-D resonant SAM, we evaluate the stability measurements on modules (aperture area of 15.64 cm^2) under combined environment of light including UV (MH (4.4% UV inside)) and heat (85±5ºC). The FMTPA-CPA-based module maintains ~90% of its initial efficiency after continuous maximum-power-point tracking (MPPT) for 1,080 h, whereas the FTPA-CPA-based and 2PACz-based modules fall to below ~73% and ~28% of their initial efficiency after 900 h (**Supplementary Fig. 67**).

Response to Reviewer #3:

The revised manuscript and the point-by-point response contain a significant amount of new experimental data, additional control experiments, and theoretical analyses. The addition of UV-stability tests under combined light/heat stress, the quantitative assembly density measurements, the FOD analysis for radical character, and the critical distinction between covalent and hydrogen bonding via acid washing are all commendable and have substantially improved the manuscript. The updated certified efficiency of 27.69% is also remarkable. The manuscript contains several points that need to be addressed before publishing on Nature.

Response: Thanks for the reviewer's positive evaluation of our work that "*all commendable and have substantially improved the manuscript. The updated certified efficiency of 27.69% is also remarkable.*". For the valuable suggestions, we have added more comprehensive measurements and discussions to further improve the quality of our work. The detailed responses are listed point-to-point as follows.

1. The new control molecule (FMTPA-DCPA) to show that removing the C=C bond and thus disrupting resonance reduces binding energy from -2.31 eV to -1.94 eV. This is a good control. But a quantitative comparison of the resulting anchoring stability under identical stress conditions is suggested to do for convincing new experimental data.

Response: Thanks for the reviewer's comments. We fully agree that a quantitative comparison of anchoring stability under identical stress conditions between FMTPA-CPA and FMTPA-DCPA would provide especially convincing experimental support for the role of the C=C bond.

In fact, following the reviewer's suggestion, we carefully considered and attempted to synthesize the molecule FMTPA-DCPA. The design was intended to isolate the role of the C=C linkage in the D-A-D electronic resonance in the previous response. However, during our synthetic exploration, we found that synthesizing a nonconjugated FMTPA-DCPA with the CPA anchoring group is intrinsically challenging. As shown in **Fig. R14a**, the CPA group is typically introduced through a Knoevenagel-type condensation, which inherently generates a conjugated olefinic linkage in the final product (*Beilstein J. Org. Chem.*, **2023**, 19, 1651; *RSC. Adv.*, **2022**, 12, 4346). As a result, an experimentally nonconjugated FMTPA-DCPA with CPA anchoring group by Knoevenagel-type condensation is not readily accessible. In addition, we considered direct post-synthetic reduction of the FMTPA-CPA and the corresponding aldehyde-containing intermediates using several reduction conditions (**Fig. R14b & c**), including mild $NaBH_4$, Hantzsch ester, and catalytic hydrogenation H_2/Pd/C strong reducing agent (*J. Org. Chem.*, **2021**, 86, 3, 2876-2894; *Angew. Chem. Int. Ed. Engl.*, **1989**, 28: 218-220; *J. Org. Chem.*, **1994**, 59, 3830-3837). However, selective reduction of only one C=C bond within the highly conjugated framework is difficult to control. The similar electronic environments of the olefinic sites make chemo-selective partial hydrogenation unlikely, which result in over-reduction and formation of complex product mixture, making product separation difficult. Despite numerous attempts, the

target product FMTPA-DCPA could not be obtained due to the limitations in current synthetic techniques.

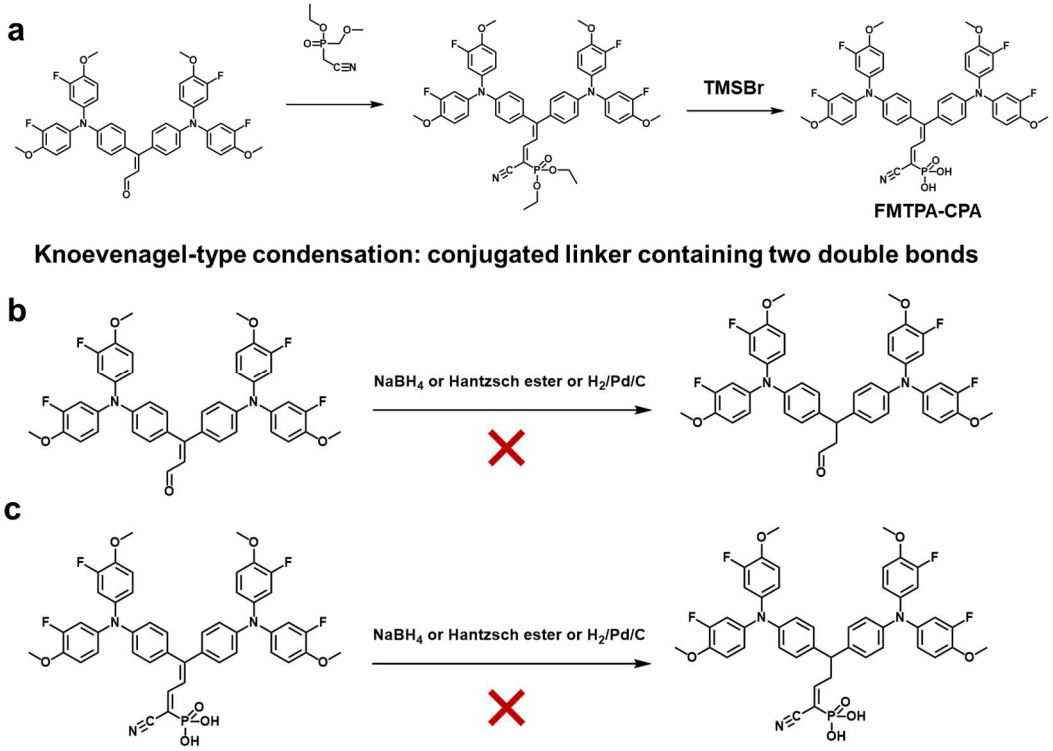

Fig. R14 (a) The synthesis route of FMTPA-CPA; (b) The post-synthetic reduction of the FMTPA-CPA; (c) The post-synthetic reduction of the corresponding aldehyde-containing intermediates.

Considering these synthetic limitations alternatively, we introduced theoretical calculations on FMTPA-DCPA as a control to isolate the electronic role of the C=C linker. The calculations show that removing the C=C bond disrupts the π-conjugation and reduces the binding energy from −2.31 eV to −1.94 eV, quantitatively supporting our interpretation that the conjugated bridge enhances covalent binding through resonance-assisted charge redistribution. In fact, as we employed the well-established and widely used theoretical calculation methods in this field, it is reasonable to believe that the calculated binding energy results in the last around response are quantitatively reliable.

We appreciate the reviewer's insightful suggestion and agree that an experimentally comparison of conjugated linker and nonconjugated linker on the resonance strength of D-A-D type SAMs is important. In the future, we would like to explore alternative synthetic routes in collaboration with an expert in synthetic organic methodology to design a series of D-A-D resonant SAMs and systematically compare the effects of molecular structure on their electronic structure characteristics and device stability.

2. The authors have replaced the HOMO-based diradical claim with a proper FOD analysis. The NFOD values (0.10 for 2PACz, 0.43 for FTPA-CPA, 0.66 for FMTPA-

CPA) are presented. What is the threshold for the claimed significant radical character? How do these values compare to known stable radicals or diradicals?

Response: Thanks for the reviewer's comments. We have provided a more careful discussion of the N_{FOD} value and compared our results with representative literatures to establish the relation between N_{FOD} value and radical character.

For the comment that "*What is the threshold for the claimed significant radical character?*", In general, N_{FOD} reflects the extent of radical character. The N_{FOD} value depends on the molecular structure, temperature and computational method (*Phys. Chem. Chem. Phys.*, **2025**, 27, 5973-5983), thus there is no universal threshold. Based on representative literature reports employing FOD analysis, N_{FOD} values close to 0 correspond to negligible radical character, value in the range of 0.1~0.3 indicate weak radical character, values in the range of 0.3~0.5 indicate moderate radical character, value above 0.5 are associated with pronounced radical character in conjugated organic molecules (*Phys. Chem. Chem. Phys.*, **2024**, 26, 25848; *Phys. Chem. Chem. Phys.*, **2024**, 26, 30018-30034; *J. Mater. Chem. C*, **2023**, 11, 16748).

For the comment that "*How do these values compare to known stable radicals or diradicals?*", the calculated N_{FOD} values of 0.10 (2PACz), 0.43 (FTPA-CPA), and 0.66 (FMTPA-CPA) indicate a clear progression from essentially negligible radical character to moderate radical character and then to pronounced radical character. In particular, the N_{FOD} value of 0.66 for FMTPA-CPA lies in the range commonly associated with significant stable radical character in conjugated organic systems. We have added representative literature comparisons in **Table R2**.

Table R2 Statistical of the N_{FOD} values in references.

Ref.	N_{FOD}	Presence of Radical Character
This work	0.66 (FMTPA-CPA)	Yes
Angew. Chem. Int. Ed., **2015**, 54, 12308-12313	0.43	Yes
Angew. Chem. Int. Ed., **2023**, 62, e202218156	0.63	Yes
Inorg. Chem., **2025**, 64, 13224-13233	0.64	Yes
Phys. Chem. Chem. Phys., **2024**, 26, 25848-25860	0.40~0.75	Yes

3. The UV stability test (Supplementary Fig. 58) indicates that FMTPA-CPA remains 81% after 1080 hours of irradiation. This is lower than the ~99% retention under LED light in the MPPT measurement. The authors should comment on whether this ~20% loss under UV is due to SAM degradation.

Response: Thanks for the reviewer's comments that help us to deepen the understanding on the mechanism of UV stability. With more optical properties and morphology characterizations on the degraded samples, we reveal the ~20% loss

between UV and LED light mainly originates from the severe defects generation and phase segregation within the perovskite bulk rather than SAM degradation, being consistent with the previous report (*Science*, **2024**, 384, 1126-1134).

To investigate the UV degradation mechanism, we prepared ITO/FMTPA-CPA (with EtOH washing)/perovskite samples, then aging 200 h under pure UV (365 nm, 56 mW cm^{-2}) lamp. In the previous response of Comment 1 from Reviewer 3, after EtOH washing, the D-A-D resonant FMTPA-CPA tends to form uniform and covalently anchored monolayer. After aging under UV lamp, the FMTPA-CPA-based buried perovskite interfaces exhibited bright crystals (referring to PbI_2) formation, accompanied by PL intensity decrease (**Fig. R15**). In addition, the PL peaks exhibited a blue shift, which was ascribed to ion migration of A-site cations (e.g., Cs^+, FA^+) that induces weak phase segregation (*Science*, **2024**, 384, 1126-1134). However, the P/In ratio of FMTPA-CPA anchored on ITO showed no significant change as observed from XPS characterization after pure UV lamp aging in **Fig. R12** (i.e., **Supplementary Fig. 78** in SI) and **Table R1** (i.e., **Supplementary Table 8** in SI). Therefore, we attribute the degradation mainly to UV-induced defects generation and phase segregation in the perovskite bulk, rather than desorption of the FMTPA-CPA SAM itself.

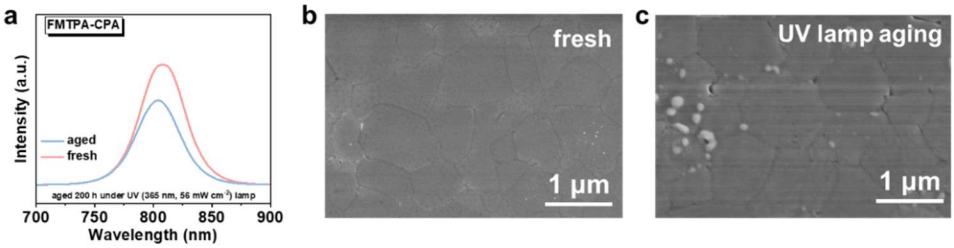

Fig. R15 (a) PL peak of buried perovskite interface based on FMTPA-CPA before and after aging under the pure UV lamp; SEM of buried perovskite interface based on FMTPA-CPA (b) before and (c) after aging under the pure UV lamp.

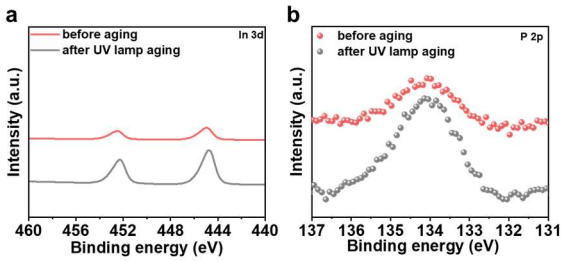

Fig. R12 (i.e., **Supplementary Fig. 78** in SI) XPS spectra of (a)In 3d and (b) P 2p obtained from the FMTPA-CPA films before and after UV irradiation.

Table R1 (i.e., **Supplementary Table 8** in SI) XPS spectra analysis obtained from the FMTPA-CPA films before and after UV lamp aging.

SAM	conditions	In area	P area	P/In
FMTPA-CPA	before aging (EtOH washing)	183058.1	4228.6	0.0231
	after UV lamp aging	536154.2	12281.1	0.0229

We have added the discussion of the UV degradation mechanism in the revised Supporting Information.

Page 17 in the revised Supporting Information:

Supplementary Note 14. Stability Mechanism Analysis

…Similarly, the FMTPA-CPA-based buried perovskite interfaces also exhibited bright crystals formation, accompanied by PL intensity decrease and peak blue shift. However, after pure UV lamp aging, the P/In ratio of FMTPA-CPA anchored on ITO showed no significant change from XPS characterization (**Supplementary Fig. 78** & **Supplementary Table 8**). Therefore, we attribute the degradation mainly to UV-induced defects generation and phase segregation in the perovskite bulk, rather than desorption of the FMTPA-CPA SAM itself.